

Distribution Agreement

In presenting this thesis or dissertation as a partial fulfillment of the requirements for an advanced degree from Emory University, I hereby grant to Emory University and its agents the non-exclusive license to archive, make accessible, and display my thesis or dissertation in whole or in part in all forms of media, now or hereafter known, including display on the world wide web. I understand that I may select some access restrictions as part of the online submission of this thesis or dissertation. I retain all ownership rights to the copyright of the thesis or dissertation. I also retain the right to use in future works (such as articles or books) all or part of this thesis or dissertation.

Signature:

Monica L. K. Sanchez

Date

Optimizing Photo-reduction Methods for the Light Induced Turnover of [FeFe] Hydrogenase

By

Monica L. K. Sanchez
Doctor of Philosophy

Chemistry

R. Brian Dyer, Ph.D.
Advisor

Craig Hill, Ph.D.
Committee Member

Tim Lian, Ph.D.
Committee Member

Accepted:

Lisa A. Tedesco, Ph.D.
Dean of the James T. Laney School of Graduate Studies

Date

Optimizing Photo-reduction Methods for the Light Induced Turnover of [FeFe] Hydrogenase

By

Monica L. K. Sanchez
B.S. and B.A., University of Texas-San Antonio, 2015

Advisor: R. Brian Dyer, Ph.D.

An abstract of
A dissertation submitted to the Faculty of the
James T. Laney School of Graduate Studies of Emory University
in partial fulfillment of the requirements for the degree of Doctor of Philosophy in
Chemistry
2020

Abstract

Optimizing Photo-reduction Methods for the Light Induced Turnover of [FeFe] Hydrogenase

By Monica L. K. Sanchez

Hydrogenases are a class of oxidoreductase enzyme which catalyze the reduction of protons to molecules of hydrogen, as well as the oxidation of hydrogen, at the fastest rates ever recorded. They do so with almost no over potential, while using earth abundant transition metals. To reproduce their unique strengths as catalysts, a detailed understanding of their chemical mechanism is required. However, it is precisely their own efficiency that presents barriers to study and replication. Due to their exceedingly rapid turnover rate, researchers have consistently struggled to map their mechanism in detail, and the research that has been produced has been characterized by conflicting data, and thus a lack of cohesive interpretation. In this thesis, a method for rapidly inducing turnover is explored, optimized and finally employed for studying two different [FeFe] hydrogenases, one from *Chlamydomonas reinhardtii* (*CrHydA1*) and the other from *Desulfovibrio desulfuricans* (*DdHydAB*).

Steady state and transient kinetic analysis of viologen based redox mediators was used to probe the ET mechanism between a nanocrystalline semiconductor and a NiFe hydrogenase. The results from this study revealed a complex interplay between the structure and the LUMO energy of the mediator, which could be tuned to optimize ET to hydrogenase. Despite significant advancement in the efficiency of the technique gained through this study, optimization for application to transient studies under varying experimental conditions remained to be explored. The results of this subsequent study led to the outlining of principles for achieving a specific solution potential based on the tuning of sample conditions.

Finally, once the details for this photo-initiation technique were outlined, the guidelines established by the previous studies were applied to the mechanistic study of two [FeFe] hydrogenases: *CrHydA1* and *DdHydAB*. Both enzymes were investigated through time-resolved spectroscopy, revealing rich intermediate dynamics on a previously unexplored timescale. The active site dynamics probed by time resolved infrared transient absorbance demonstrated the kinetic competency of several intermediate states previously proposed. Furthermore, preliminary results on the mechanism of the chemical reactions necessary for inter-conversion of the verified intermediates are reported, and suggest the likely pathways involved in enzymatic turnover.

Optimizing Photo-reduction Methods for the Light Induced Turnover of [FeFe] Hydrogenase

By

Monica L. K. Sanchez
B.S. and B.A., University of Texas-San Antonio, 2015

Advisor: R. Brian Dyer, Ph.D.

A dissertation submitted to the Faculty of the
James T. Laney School of Graduate Studies of Emory University
in partial fulfillment of the requirements for the degree of Doctor of Philosophy in
Chemistry
2020

Acknowledgements

To my committee, for challenging me (and passing me).

To my husband, for keeping me laughing.

To my lab mates, for laughing with me (and at me TBH).

To Brian Dyer, for pushing me (and letting me know when my data was garbage.)

Table of Contents

Chapter 1: Introduction

1.1 – The Global Energy Crisis and the Storage of Energy in Small Molecule Bonds	2
1.2 - Efficient Oxidoreductase Enzymes for Small Molecule Synthesis and Solar Fuels	6
1.3 – Hydrogenases: Structure, Efficiency and Challenges to Study	9
1.4 – Overview of [FeFe] Hydrogenases Catalytic Mechanism and Proposed Intermediates	11
1.5 – The “Potential Jump” Method for sub-Turnover Kinetics Analysis	14
1.6 – Hypothesis and Scope of Thesis	17
1.7 – References	20

Chapter 2: Materials and Methods

2.1 - Introduction	31
2.2 - Mediators Synthesis	32
2.2.1 - Preparation of 2-carbon Linker Mediators: DQ52 and DQ42	33
2.2.2 - Preparation of 3-carbon Linker Mediators: DQ03, DQ53 and DQ43	34
2.3 – Synthesis and Manipulation of Semi-Conducting Nanomaterials: CdSe QDs, CdSe/CdS Dot-in-rod and CdSe Nanorods	34
2.3.1 - Preparation of CdSe Quantum Dots	35
2.3.2 - Preparation of CdSe/CdS Dot-in-Rod (DIR) Nanorods	35
2.3.3 - Preparation of CdSe Nanorods	36
2.3.4 - Ligand Exchange of Nanoparticles for use in Aqueous Media	37
2.4.1 Buffers	37
2.5 - Analytical Methods	38
2.5.1 - UV/Vis Absorbance	38
2.5.2 – Photoluminescence Spectra	38
2.5.3 – Fourier Transform Infrared Spectroscopy (FTIR)	39
2.5.4 – Transmission Electron Microscopy (TEM)	40
2.5.5 – Time Correlated Single Photon Counting (TCSPC)	40
2.5.6 – In tandem Transient IR and Visible Absorbance	41

2.5.7 – Ultrafast Transient Visible Absorbance	42
2.5.8 – Nanosecond Transient Visible Absorbance Spectroscopy	43
2.5.9 – Electrochemistry: Cyclic Voltammetry	43
2.5.10 – Electrochemistry: Chronopotentiometry	44
2.5.11 – ¹ H NMR Spectroscopy	45
2.5.12 – X-ray Quality Crystal Growth Technique	45
2.6 – Light Driven Activity Assays and Quantum Yield Calculation	46
2.6.1 – Light-driven Mediator Reduction	46
2.6.2 – Light-driven H ₂ Production	47
2.6.3 – H ₂ Detection via a Pressure Sensor	48
2.7 – Data Analysis	49
2.7.1 – Fitting Infrared Transient Absorbance Data	49
2.7.2 – Fitting Visible Transient Absorbance Data	51
2.7.3 – Global Fitting FTIR and Absorbance Spectra	51
2.8 – References	52

Chapter 3 Optimizing Electron Transfer from CdSe QDs to Hydrogenase for Photocatalytic H₂ Production

3.1 – Abstract	55
3.2 – Introduction	56
3.3 – Results and Discussion	57
3.3.1 – Characterization and Analysis of Mediator Structural and Electronic Properties by UV-Vis, ¹ H NMR, X-ray Crystallography, and Cyclic Voltammetry	57
3.3.2 – Determining the Extinction Coefficient for each 1-electron Reduced Mediator via Chronopotentiometry	61
3.3.3 – Quantum Efficiency of Photo-driven Mediator Reduction	64
3.3.4 – Quantum Efficiency of Photo-driven Hydrogen Production	67
3.3.5 – Spectral Characteristics of Mediator Radical Decomposition Product	72
3.4 – Transient Studies of Electron Quenching by Mediator Population and Charge Recombination	75
3.4.1 – Excited State Electron Quenching by Mediator LUMO	75

3.4.2 – Mediator Radical Charge Recombination	77
3.5 - Conclusions	80
3.6 – Appendix with Supplementary Data	81
3.6.1 H NMR spectrum for each mediator	82-
	86
3.6.2 Cyclic Voltammograms for each mediator	87
3.6.3 Summary of X-ray Diffraction Data	89
3.7 - References	90
Chapter 4 “The Laser-Induced Potential Jump: a Method for Rapid Electron Injection into Oxidoreductase Enzymes”	
4.1 – Abstract	97
4.2 – Introduction	98
4.3 – Results and Discussion	101
4.3.1 – System Components: Photosensitizer, Mediators and Catalyst	101
4.3.2 – Steady-state Quantum Yield of Photo-driven Mediator Reduction and H ₂ Production	103
4.3.3 – Factors Affecting Potential Jump	109
4.3.4 – Kinetics of ET to <i>CrHydA1</i> Hydrogenase	115
4.4 – Utilization of CdSe NRs for 532 nm Excitation	119
4.4.1 – Steady State Photo-driven Mediator Reduction	121
4.4.2 – Transient Potential Pump-Power Dependence with CdSe NRs	123
4.5 – Conclusions	124
4.6 – References	128
Chapter 5 Mechanistic Studies of [FeFe] Hydrogenase: <i>CrHydA1</i> and <i>DdHydAB</i>	
5.1 – Abstract	137
5.2 – Introduction	138
5.3 – Investigating the Kinetic Competency of Proposed Intermediates	141
5.3.1 – Rapid Initiation of Hydrogenase Turnover using a Potential Jump	141
5.3.2 – Photoprotection of the Enzyme by Photosensitizer	144

5.3.3 – H-cluster Sub-turnover Kinetics at pH 8.4	146
5.3.4 – TRIR Spectra Reveal a New Intermediate State	152
5.3.5 – Conclusions on the Kinetic Competency of Proposed Intermediate States	154
5.4 – <i>CrHydA1</i> Mechanistic Studies with PDT mutant	157
5.4.1 – Light Titration Experiments with the PDT Mutant	159
5.4.2 – Kinetics Study of PDT Mutant under pHs Ranging from pH 6.5 to pH 10	162
5.5 – <i>DdHydAB</i> Mechanistic Studies	166
5.5.1 - pH Dependence of Intermediate State Transitions	167
5.2.2 – Redox Anti-cooperativity with PDT mutant	173
5.6 – Conclusions on [FeFe] Hydrogenase Mechanistic Studies	180
5.7 – References	181
Chapter 6: Conclusions and Future Directions	
6.1 – Conclusions from	189
4.2 – Introduction	190

List of Figures

Chapter 1 Introduction

Figure 1.1	Energy consumption by TWhrs per source and Energy Density comparison by kWhrs per gram	2
Figure 1.2	Common Oxidoreductase Enzymes with Solar Fuels Applications	6
Figure 1.3	Hydrogenase Active Sites	10
Figure 1.4	Summary of Intermediate States	12
Figure 1.5	Potential Jump Diagram	15

Chapter 2

Figure 2.1	Summary of Synthetic pathways for Mediators Synthesis	33
Figure 2.2	Chronopotentiometry Experiment Setup	44
Figure 2.3	Representative Quantum efficiency experimental data	47
Figure 2.4	Homebuilt Pressure Sensor components	48
Figure 2.5	Data Analysis procedure for TR IR data	50
Figure 2.6	Data Analysis Procedure for TR Vis data	51

Chapter 3

Figure 3.1	UV-Vis Molar Extinction Spectra of Oxidized Mediators	60
Figure 3.2	Summary of Chronopotentiometry Results	62
	a) Plot of Absorbance of mediator radical vs. time	
	b) Table Summarizing experimentally determined extinction coefficients for radical species	
Figure 3.3	Light-Driven Mediator Reduction Spectra	65
	a) UV-Vis molar extinction spectra of reduced mediators	
	b) Representative plots of radical concentration vs. Illumination Time for each mediator	
Figure 3.4	Steady-state Light-driven mediator reduction experiment results	66
	a) Plot of Concentration of radical generated vs. illumination time	
	b) Plot of QE_{rad} vs. Reduction potential of mediator	

	c) Relative Energy diagram of ET steps between CdSe QDs and mediators	
Figure 3.5	Results of Light-driven H ₂ Production	70
	a) H ₂ production as a function of illumination time	
	b) Plot of QE _{hyd} vs. reduction potential	
	c) Concentration of reduced mediator versus illumination time during H ₂ production measurements	
	d) Relative energy diagram of ET steps from QD to mediator to hydrogenase	
Figure 3.6	Spectral Properties of Mediator Radical Decomposition Product	72
	a) Difference Spectra for Mediators DQ03, DQ53 and DQ43	
	b) Concentration of Mediator Radical vs. Time	
	c) Bar Graph summarizing relative absorbances of radical to decomposition product over time	
Figure 3.7	Ultrafast transient absorbance kinetics	76
	a) Averaged absorbance spectra over 20 femtoseconds for CdSe QDs, DQ42 and DQ43	
	b) Normalized band edge bleach recovery kinetics	
Figure 3.8	Nanosecond transient absorbance kinetics	77
	a) Averaged Absorbance spectra over 10's of nanoseconds	
	b) Kinetics of Mediator radical decay	
	c) Relative energy diagram of mediator LUMOs and CdSe QD CB and VB	
	d) Marcus plot of change in energy vs. natural log of rate of charge separated state formation	
Figure 3.9	H NMR spectra of Mediator Salts	82-
		86
Figure 3.10	Cyclic Voltammograms for Mediator Salts	87
 Chapter 4		
Figure 4.1	Potential Jump System Components	102

	a) Schematic of Overall ET pathway	
	b) Relative Energy Level Diagram	
	c) Mediators and their Reduction Potentials Investigated	
	d) TEM images of CdSe/CdS NRs used	
	e) Absorbance and emission spectra of CdSe/CdS NRs used	
Figure 4.2	Steady-state Mediator Reduction and Hydrogen Production	104
	a) UV-Vis Extinction spectra for Reduced Mediators	
	b) Plot of QE_{rad} vs. Mediator Starting Concentration	
	c) Plot of QE_{rad} of mediator reduction vs pH	
	d) Plot of TCSPC results examining hole transfer efficiency	
	e) Schematic Depicting MPA Capping Ligand Protonation State	
Figure 4.3	Steady-state Hydrogen Production	108
	a) Plot of mols of H_2 vs. Illumination Time	
	b) Plot of Solution Potential (mV) vs. Illumination Time	
Figure 4.4	Transient absorbance experiment examining pump-power dependence of mediator reduction under several conditions	110
	a) Representative Pump Power Dependence Data	
	b) Summary of Pump Power dependence at different pHs for DQ03	
	c) Summary of Pump Power dependence at different pHs for DQ53	
	d) Summary of Pump Power dependence at different pHs for DQ43	
	e) Summary of Pump Power dependence for 2X DIR concentration	
Figure 4.5	Schematic of Pimer Formation and Disproportionation Mechanism	113
Figure 4.6	Time-resolved Visible and IR measurements with <i>CrHydA1</i>	117
	a) Diagram of <i>CrHydA1</i> H-cluster	
	b) FTIR of 1 mM and 4 mM samples	
	c) TR-Vis Traces for 1 mM and 4 mM samples	
	d) TRIR traces of H_{ox} and H_{red} Intermediates for Both Samples	
	e) TRIR traces of $H_{red}H^+$ for Both Samples	
	f) TRIR traces of $H_{sred}H^+$ for Both Samples	
Figure 4.7	UV-Vis absorbance spectra comparing band edge shift of CdSe NRs to Dot-in-Rod CdSe/CdS NRs	120

Figure 4.8	Steady-state photo-driven mediator reduction results	121
	a) UV-Vis spectra of initial samples for trials 1 and 2	
	b) Plot of Abs @ 510 nm for trials 1 and 2	
Figure 4.9	Pump Power dependence of Mediator reduction with CdSe NRs	123
Chapter 5 Mechanistic Studies of [FeFe] Hydrogenase		
Figure 5.1	Schematic relating Simplified versions of proposed catalytic cycles for <i>CrHydA1</i> [FeFe] Hydrogenase	140
Figure 5.2	Laser induced potential jump	143
	a) ET Pathway	
	b) Relative energy diagram	
	c) TR vis of radical population during potential jump	
	d) Representative FTIR spectrum of <i>CrHydA1</i> sample	
Figure 5.3	TRIR Kinetics of CO-Inhibited Intermediate populations	145
	a) TRIR traces of related CO-inhibited intermediates	
	b) Proposed reaction scheme for $H_{ox-CO} \rightarrow H_{oed-CO} \rightarrow H_{sred}H^+$	
Figure 5.4	H-cluster kinetics	148
Figure 5.5	Potential Jump TRIR Spectra	153
	a) Potential Jump IR transients at 1891, 1893 and 1895 cm^{-1}	
	b) TRIR spectra generated from individual IR transients at time delays	
	c) Steady-state difference FTIR spectrum	
Figure 5.6	<i>CrHydA1</i> Active site Structure and potential variations	150
	a) Crystal structure of active site from <i>Cpl</i>	
	b) Proposed alterations to H-cluster	
Figure 5.7	Comparison of PDT mutant to WT H-cluster	158
	a) Drawing of WT and PDT H-cluster	
	b) Observable intermediate transition with PDT mutant	
Figure 5.8	Phototitration experiments with <i>CrHydA1</i> : WT and PDT	161
	a) WT <i>CrHydA1</i> initial FTIR pre illumination spectrum	
	b) PDT <i>CrHydA1</i> initial FTIR pre illumination spectrum	

	c) WT <i>CrHydA1</i> photo illumination results by FTIR	
	d) PDT <i>CrHydA1</i> photo illumination results by FTIR	
Figure 5.9	Kinetics of PDT mutant monitoring H _{ox} and H _{red} intermediates	164
Figure 5.10	Comparison of structure between <i>CrHydA1</i> and <i>DdHydAB</i> hydrogenase	166
	a) Protein structure of <i>CrHydA1</i> and <i>DdHydAB</i> hydrogenase	
	b) Normalized TR Vis kinetics	
Figure 5.11	FTIR spectrum of <i>DdHydAB</i> [FeFe] Hydrogenase	167
Figure 5.12	pH dependence of formation and decay kinetics of intermediate states	169
	a) TRIR Kinetics of H _{red} monitoring at 1934 cm ⁻¹	
	b) TRIR Kinetics of H _{red} H ⁺ monitoring at 1916 cm ⁻¹	
	c) TRIR Kinetics of H _{sred} H ⁺ monitoring at 1911 cm ⁻¹	
	d) TRIR Kinetics of H _{hyd} monitoring at 1980 cm ⁻¹	
Figure 5.13	WT kinetics of F-cluster intermediates	174
	a) Schematic of auxiliary Fe ₄ S ₄ clusters and H-cluster	
	b) FTIR of WT sample showing F-cluster region	
	c) TRIR kinetics of H _{ox} F-cluster region	
Figure 5.14	PDT kinetics of F-cluster intermediates	176
	a) TRIR kinetics of H _{ox} F _{ox} region (1941 – 1945 cm ⁻¹)	
	b) TRIR kinetics of H _{red} F _{red} region (1934 – 1940 cm ⁻¹)	
Figure 5.15	Time-resolved FTIR of F-cluster region	178

List of Tables

Table 3.1	Summary of Structural Information (Including X-ray Structures) and Reduction Potentials for Mediator Salts	58
Table 3.2	Summary of Solution Potential data compared to photo-driven H ₂ production efficiency	71
Table 3.3	Summary of transient data comparing rates of radical formation and decay	77
Table 3.4	Summary of Cyclic Voltammetry data	88
Table 4.1	Summary of pump power and pH dependence results from TRVis experiments	111
Table 5.1	Summary of transient data comparing rates of intermediate states formation and decay for WT <i>DdHydAB</i>	171
Table 5.2	Summary of formation and decay constants for PDT kinetics data with <i>DdHydAB</i>	177

List of Equations

Equation 2.1	Equation for determining absorbance from FTIR spectra	39
Equation 2.2	Equation used for determining the amplitude weighted lifetime of fluorescence decay measurements	41
Equation 2.3	Equation used for determining the extinction coefficient from chronopotentiometry	45
Equation 2.4	Equation used to determine QE of mediator reduction (QE _{rad})	46
Equation 2.5	Sum of Exponentials fit function used to fit transient absorbance data	

List of Abbreviations

CB, conduction band

CR, charge recombination

CrHydA1, *Chlamydomonas reinhardtii* [FeFe] hydrogenase

DdHydAB, *Desulfovibrio desulfuricans* [FeFe] hydrogenase

DIR, dot-in-rod

ET, electron transfer

FTIR, fourier-transform infrared

H₂ase, hydrogenase

LUMO, lowest unoccupied molecular orbital

MPA, mercaptopropionic acid

MV, methyl viologen

NCS, nanocrystalline semiconductor

PCET, proton coupled electron transfer

PD, pimer disproportionation

PL, photoluminescence

PDQ, propylene bridged diquat

QCL, quantum cascade laser

QD, quantum dot

QE, quantum efficiency

TA, transient absorbance

TCSPC, time correlated single photon counting

TEM, transmission electron microscopy

TRIR, time-resolved infrared

TRVis, time-resolved visible

TOPO, trioctylphosphine oxide

VB, valence band

Chapter 1

Introduction

1.1 The Global Energy Crisis and the Storage of Energy in Small Molecule Bonds

It is estimated that by 2050, the total human population will have reached 9 billion persons, an increase of 2 billion within three decades.¹ Currently, the global population consumes more than 16 TWhrs of energy annually (Fig. 1.1).² Human energy consumption will continue to grow, not only in sheer quantity, but also in average usage per person. Global population growth must be evaluated in concert with the increasing rate at which underdeveloped countries are projected to continue to industrialize. In 2007, projections indicated that within 20 years, global energy consumption will increase by 60% over current recorded levels.¹ In sheer numbers, the current energy economy of the world is based almost exclusively on fossil fuels, a state of affairs that is defined equally by the ubiquity of their use and their finite, nonrenewable supply. Energy research has been increasingly focused on the exhaustive evaluation of renewable energy technologies, with the aim of finding those methods best suited to supplementing and eventually, independently providing for the world's energy needs. This goal requires considering not only the mechanisms of energy provision, but the ease with which such methods

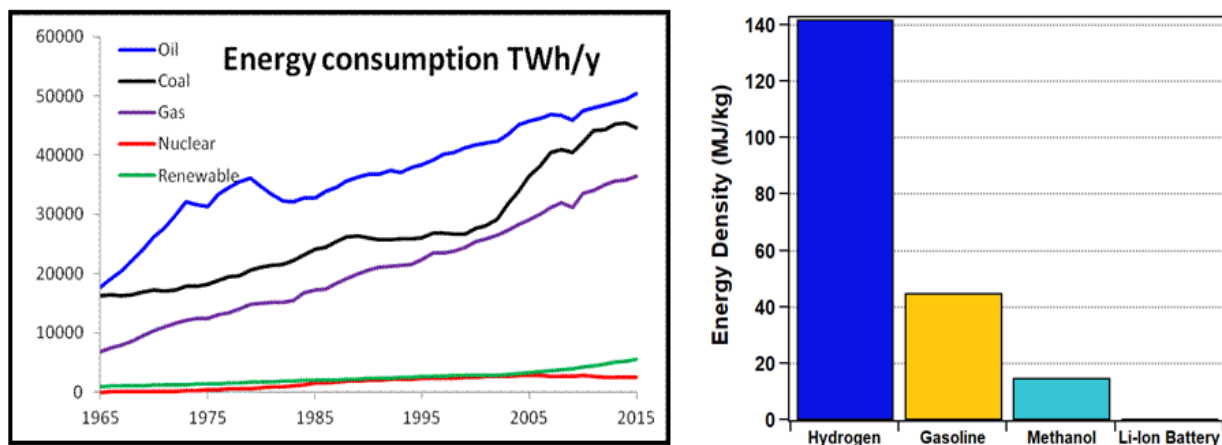


Figure 1.1 Comparison of common energy resources per year (left). Comparison of energy density of frequently considered energy resources: Hydrogen, gasoline, methanol and Li-ion battery. (right) Adapted from reference https://www.mpoweruk.com/energy_resources.html

can be scaled up, and necessary infrastructure built.²⁻³ Due to the fundamental role energy resources play in the function of all levels of economic activity, the degree to which such concerns are addressed may very well decide the state of the global economy in the current century.

Currently, several non-chemical strategies of harvesting energy from the environment have been developed and adopted on a relatively wide scale, such as wind-based turbines, solar energy panels, and hydroelectric dam facilities.¹ Each of these methods is based essentially on the conversion of kinetic, solar or thermal energy into electricity, which is then distributed through the preexisting power grid. They are also all essentially based on recurring, dynamic natural phenomena, whether wind patterns, sunlight, or movement in bodies of water. As such, they each face a similar set of inbuilt weaknesses, which currently limit their widespread applicability. Often, the drivers of these renewable sources do not provide the needed energy output, in many cases due to uncontrollable changes in weather patterns. The energy deficit thus created leaves communities without sufficient backup energy, requiring nonrenewable sources to make up the gap.

The converse problem also regularly arises, i.e. the overproduction of such electrical energy. In the state of California, the California Independent System Operator (ISO) has had to engage in the dumping of excess solar panel-generated electricity, by paying neighboring states to accept the extra power into their grids. During peak solar flux, the supply of solar power produced regularly exceeds demand, leading to the consistent need for dumping. These issues point to the difficulties inherent in current renewable energy sources. The energy they provide is not easily regulated for discretionary use, but instead energy grids must work around their dynamic patterns of supply.

In order to address the issue of electricity over-supply, Li-ion batteries have been adapted for use in conjunction with regional power grids, and are being used to store excess energy built up during peak renewable supply. The world's first large scale Li-ion battery electricity storage facility was built to supply energy to an entire region in southern Australia. While it has initially been found proficient at its aim of energy storing and distribution, the battery infrastructure that powers this behemoth endeavor has a lifespan of only 15 years, at maximum. This facility will have to be entirely rebuilt every decade and a half. Despite the massive strides that are actively being made in the optimization of Li-ion battery technology, there is currently no feasible path toward their wide scale use in the energy economy.

Due to the high cost of production, Li-ion batteries are at best suited for supplementation of energy storage, at least while other renewables work to develop scale. The high environmental costs of procuring the lithium needed for its use means that these batteries are less a renewable energy option than a recurrence of the environmental and supply issues we currently face with fossil fuels. Research has even indicated that due to the high environmental cost of the strip mining currently used to procure lithium, it is more environmentally sustainable to use vehicles running on fossil fuels to the maximum extent of their lifespan, rather than to upgrade to a Li-ion battery-powered vehicle. The many structural problems detailed here have led many to believe that any attempt to truly resolve our global energy problems must be based on an alternative energy storage method from those currently in use.²⁻³

The most efficient energy storage method currently known is that of the energy stored in small molecule chemical bonds (Fig. 1.1). For example, the energy density of H₂ is at least three orders of magnitude greater than state-of-the-art Li-ion batteries. Without an unforeseen revolution in battery technology, the use of chemical fuels, either in gaseous or liquid form, will

continue to be the most reasonable energy storage solution. This state of limitation is primarily due to the pivotal importance of energy density in fuel cost and application.⁴⁻⁸ Storage in H-H bonds, C-H bonds, -OH bonds, and CO bonds in the form of H₂, methane, CO₂ or even alcohols such as methanol or ethanol, are just a handful of the alternatives which are being viewed and evaluated as potentially viable replacements for fossil fuel sources precisely due to their high energy density.^{3-4, 9-11} But as with the renewable sources previously noted, an energy program based on the use of these chemical bonds is not without its own challenges to implementation.

A key barrier to making these potential fuel sources widely available is a way to efficiently form these bonds from abundant substrates (i.e. water, methane, CO₂ etc.) The energetic penalty for forming the bonds of these potential fuels is often quite high.^{9, 12} State of the art technology currently used for transforming these chemicals is at best modestly efficient and often completely unsustainable, as the energy costs for making many of these chemical feedstocks is quite high across the board.^{13-14 15} This is due to the kinetic and thermodynamic stability of the bonds present in the raw materials used as precursors to these fuels, such as C-H and O-H of methane and water, respectively requiring the use of a catalyst to overcome these barriers.

The chemical reactions required to efficiently activate these bonds are currently out of reach and occupy a focus of academic interest. Despite the fact that efficient manipulation of these chemical bonds is not yet possible, their use is nevertheless essential to resolving the issues with fossil fuel based energy (i.e. environmental cost and finite supply) that current renewables sources cannot resolve (in the form of electricity storage based on rare earth metals). The escalation of world energy consumption has forced the issue in its own way, underlining the

limitation of current methods to meet future demand. Innovative solutions to this longstanding energy barrier are desperately needed.

1.2 Efficient Oxidoreductase Enzymes for Small Molecule Synthesis and Solar Fuels

When it comes to producing catalysts which successfully overcome the energetic barriers associated with activating small molecules, Nature, in nearly all cases, remains the gold standard. The success of biocatalysts can be summarized by two key characteristics: 1) their high enzyme-substrate binding, 2) their high catalytic turnover rates relative to uncatalyzed reactions or manmade examples.¹⁵ But perhaps the most compelling testament to their dominance as catalysts is their ability to achieve these results with almost no overpotential, with earth-abundant transition metals, under relatively neutral conditions.¹⁶ This means that these chemical transformations occur at the thermodynamic limit for bond formation minimizing energy waste without requiring expensive metals or harsh conditions to make the chemistry favorable.

These enzymes, among them methane monooxygenases (MMOs)¹⁸, hydrogenases¹², nitrogenases^{17,19} and carbon monoxide dehydrogenase¹⁷, have been capable for many millions of years of generating and maintaining high energy feedstocks as energy currency. These biocatalysts accomplish such pivotal biological tasks through elegant, efficient mechanisms for converting photons and other energy resources, such as NAD(P)H, into the desired products, again doing so with little to no energy wasted at any step.^{17, 20} MMOs are able to selectively convert methane to methanol¹⁸, nitrogenases activate the N-N bond to form ammonia¹⁹, and hydrogenases are able to efficiently produce and oxidize molecules of H₂²¹.

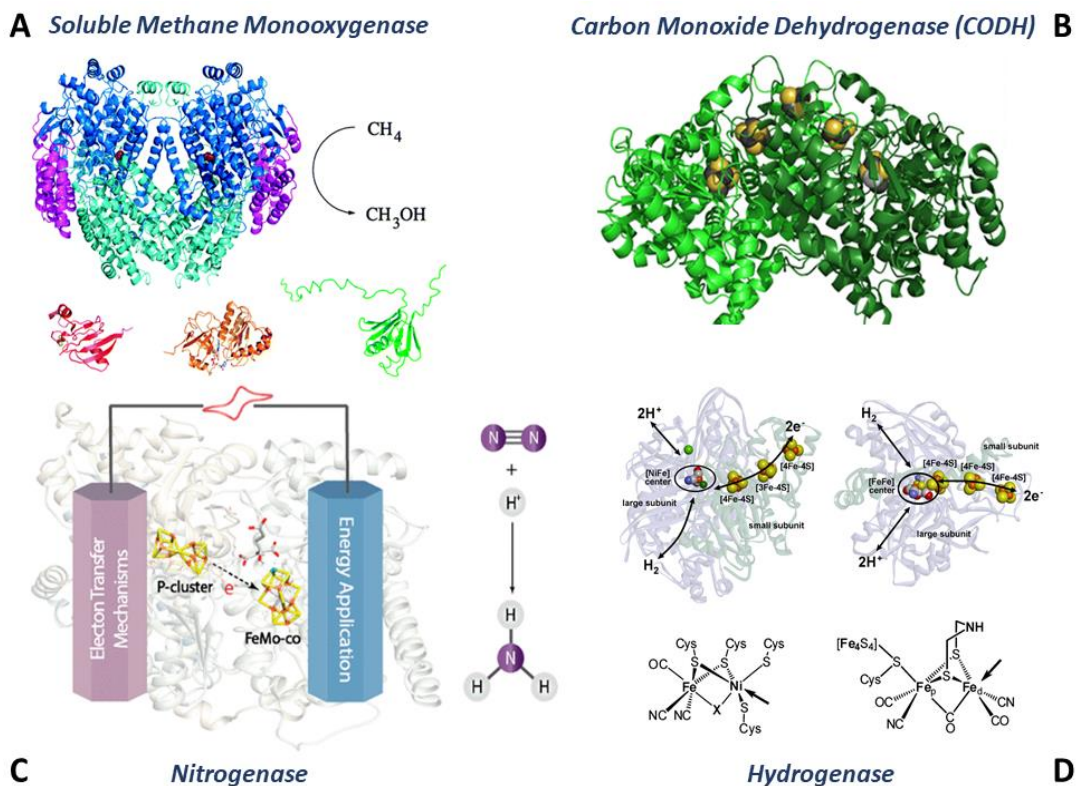


Figure 1.2 Examples of oxidoreductase enzymes frequently studied for solar fuels applications. A) soluble methane monooxygenase (sMMO, (PDB 1MTY). Reproduced from reference 13 with permission from Annual Review of Biochemistry. B) Carbon monoxide dehydrogenase -II (CODH-II, PDB 2YIV). Reproduced from Ref. 16 with permission from The Royal Society of Chemistry. C) Nitrogenase (N₂ase, PDB 4WZA). Adapted with permission from Cai, R.; Minter, S. D., Nitrogenase Bioelectrocatalysis: From Understanding Electron-Transfer Mechanisms to Energy Applications. *ACS Energy Letters* **2018**, 3 (11), 2736-2742. Copyright 2018 American Chemical Society. D) [FeFe] and [NiFe] Hydrogenases (H₂ase, PDB 1H2R). Adapted with permission from Lubitz, W.; Ogata, H.; Rüdiger, O.; Reijerse, E., Hydrogenases. *Chemical Reviews* **2014**, 114 (8), 4081–4148. Copyright 2014 American Chemical Society.

Due to their impressive longstanding track record, these biocatalysts are frequently looked to as inspiration for designing manmade catalysts capable of reproducing this chemistry, both for industrial chemical feedstocks, as well as possible means to store energy.¹⁸ Progress has been made towards unlocking the design principles of the catalytic cores responsible for the chemistry observed, resulting in significant advances in both our understanding of these catalysts and the reproduction of their chemistry by artificial means.¹⁹⁻²⁰

Some notable examples directly inspired by the inner-sphere ligand structure of [FeFe] hydrogenase have been published in recent years^{21,22}. Darensbourg et al. has been one of the pioneers of this field, and in 2018 published work describing an O₂ tolerant [FeFe] hydrogenase mimic which also efficiently generates H₂.²¹ This work is just one example of the way in which studying these naturally occurring enzymes, with the goal of emulating their structural motifs, has the potential to translate into adoptable strategies for improving the utility of these catalysts. By incorporating structural patterns directly observed in the catalytic core of [FeFe] hydrogenase, in this case pendant amines to act as proton shuttles to coordinate with the Fe atom, a giant step forward in the reproduction and control of hydrogen catalysis was achieved.

Despite these improvements, the field still faces a host of issues regarding how these remarkable systems can be most effectively studied.^{15, 23-24} Current approaches focus primarily on establishing a structure-function relationship between the active-site structural motifs and the chemistry that occurs. Experimental techniques range from traditional enzymological approaches, such as using protein crystallography, to flow techniques used to gain insight on the enzyme as it undergoes turnover.²⁵⁻²⁷ Other methods seek to modify the protein architecture itself, to try and identify which structural or chemical aspects are key to functionality.²⁸ One typical approach to accomplish this is done by mutating the active-site with the goal of trapping

different intermediate populations for characterization. Again, while much has been learned from these varied approaches, often what is missing are methods which can capture, in real time, the chemistry and structural transformations occurring in biocatalysts as they undergo catalysis with native protein architecture.

1.3 Hydrogenases: Structure, Efficiency and Challenges to Study

In addition to the focus they receive from those studying biomimetic catalysis, interest in the study of hydrogenases is widespread within the community of solar fuel researchers, as they form one of the most energy dense compounds known, hydrogen. Hydrogenases do this by efficiently moving protons and electrons, and stabilizing transition states, which act to lower barriers to bond formation.^{12, 29-30} Broadly speaking, through a network of redox active cofactors and protonatable amino acids, two equivalents of electrons and two equivalents of protons are shuttled to the active-site to form H₂ gas, with a speed and efficiency rivaled only by platinum. This entire process is accomplished with Ni and Fe atoms in the active site.^{12, 30} It is for these reasons that this class of enzyme remains the “gold standard” for hydrogen producing catalysts, and thus the reproduction of its chemistry is of considerable interest to researchers²⁹

Hydrogenase is also a model oxidoreductase catalyst by which methodologies for triggering and studying its catalytic mechanism can be developed and tested.

There are three primary classes of hydrogenase enzymes, assigned according to the composition of their active site (Fig. 1.3): [FeFe], [NiFe], and Fe-only.^{12, 30-31} As mentioned previously they can participate in both H₂ production and oxidation though some classes can be biased towards one process by varying conditions or active site amino acids. However, there are a few structural motifs consistent between all three hydrogenases despite having different

catalytic mechanisms and evolutionary origins²⁹. The first is an electron transport pathway composed of [Fe₄S₄] cluster(s) which provides a pathway for electrons to be delivered to the active site.³²⁻³⁴ The second is an amino acid chain which allows protons into the active site.^{25, 35} The last is a hydrophobic gas channel which allows the flow of H₂ or other small diatomic molecules into the active site.^{12, 25, 29, 31, 36} Of the three classes of hydrogenase, [FeFe] hydrogenase holds the record for the highest turnover frequency (ranging from 100 and 10000 s⁻¹)¹² of these enzymes, thus so much attention has been devoted to understanding its catalytic mechanism.

To date, several intermediate states of [FeFe] hydrogenase have been successfully identified using a wide array of spectroscopic techniques.^{25-26, 36-42} These states have been characterized by a variety of techniques, including but not limited to: protein crystallography,⁴³ low temperature Fourier transform infrared spectroscopy (FTIR), nuclear resonance vibrational scattering (NRVS),⁴² attenuated total reflectance FTIR (ATR-FTIR). Mutations of the active site, proton transport pathway, or inclusion of non-native metals and ligands in the active site or FeS cluster are also common techniques for isolating various intermediate states by trapping these intermediates.^{25, 44-46} These variations and manipulations of the enzyme have been quite successful in mapping the most critical components of enzyme catalysis, and a number of intermediates have been identified. However, despite the tremendous effort devoted to understanding this catalyst, there remains considerable disagreement as to the exact nature of the catalytic mechanism for [FeFe] hydrogenase. Particularly, disagreement surrounds which of these are intermediate states, which represent different active site arrangements as the enzyme undergoes turnover, and which are off pathway states. This lack of a consensus view has itself led to disagreement over which states are most critical to understanding the catalytic mechanism.

This challenging state of affairs is largely attributable to the very properties of hydrogenases which make them of such interest. The high turnover frequency of these catalysts results in short-lived, unstable intermediate transition states. With TOF's upwards of 1000 turnovers per second,^{16, 47} the lifetime of the intermediate states proposed to participate in the catalytic cycle are very short and so are nearly unobservable with traditional equilibrium techniques.

1.4 Overview of the [FeFe] H₂ases Catalytic Mechanism and Proposed Intermediates

The active site of [FeFe] hydrogenase, ubiquitous among all its variants, is composed of a bimetallic di-iron core, ligated by 3 CO ligands and 2 CN ligands. The 2 Fe atoms are coordinated by two thiolate bridges suspending a pendant amine group. Also coordinated to the active site is a Fe₄S₄ cluster through a thiolate bridge. The summary of these components is often referred to as the "H-cluster."^{36, 48-51}

As mentioned in the previous section, success has been achieved in identifying several intermediate states that the enzyme's active site is thought to pass through during catalysis.^{36, 50-53} These intermediates have been characterized primarily by equilibrium studies, taking advantage of natural resting states, manipulating sample conditions or mutating the active site, so that large populations of these intermediates might be generated and characterized spectroscopically. Some key intermediates are listed in Fig. 1.4. One technique that is frequently utilized in these studies is the use of infrared signatures to identify populations of different intermediate states. The CO and CN ligands coordinated to the Fe atoms of the active site are convenient spectroscopic handles for experimentally determining intermediate characteristics. These ligands are sensitive to perturbations of active site electron density and protonation state due to pi-

backbonding with the p orbitals of the Fe atoms in the active site. Changes in the protonation state of nearby cofactors or amino acids, or even in the oxidation state of the metal, cause shifts in the IR frequencies, yielding IR signatures which can be monitored and used to identify different intermediate populations as the enzyme turns over. This was the method used to identify the intermediates of Fig. 1.4.

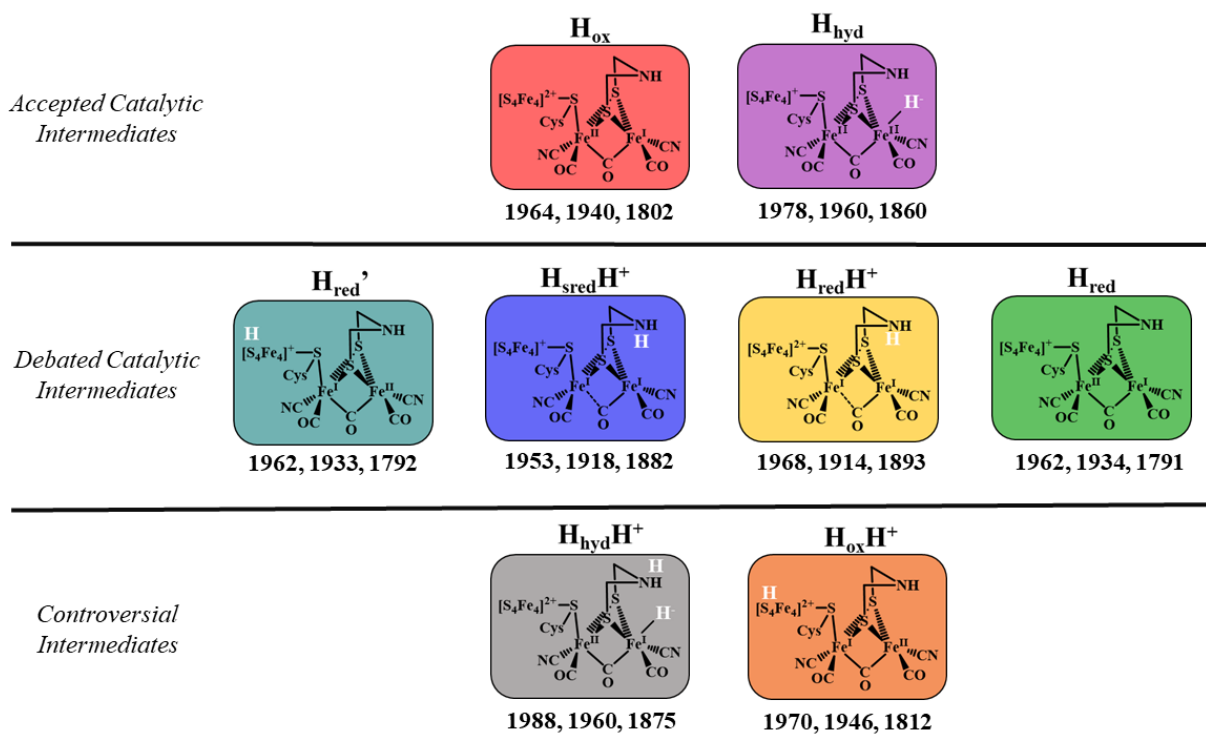


Figure 1.4 Summary of catalytic intermediates which have been identified and characterized categorized by whether they are “accepted”, “debated”, or simply controversial/have not been physically characterized but proposed anyways. Signature IR frequencies that have been used to identify and characterize these intermediates are listed beneath the depiction for each intermediate and are given in wavenumbers (cm^{-1}).

Determining which of these intermediate states the enzyme actually populates during turnover remains the subject of much controversy, though there are a few key points that have been agreed upon.^{49, 52} The active site of [FeFe] hydrogenase begins in a mixed valent state of $[\text{Fe}^{\text{II}}\text{Fe}^{\text{I}}]$, with an oxidized Fe_4S_4 cluster, named H_{ox} . Upon one-electron reduction of the Fe_4S_4 cluster coordinated to the di-Fe core, the H_{red} state forms. The location of this electron is still unclear, with some questioning whether the electron is indeed located on the Fe_4S_4 cluster, or if it is instead on the proximal Fe of the bimetallic center.³⁵ Some recent reports have also proposed that this initial ET step is actually proton coupled, and results in the reduction and concomitant protonation of the Fe_4S_4 cluster. The intermediate formed by this step is referred to as H_{red}' .^{39, 53}

After this initial reduction step, there are two other possible intermediate states the catalyst enters. One proposed intermediate is the $\text{H}_{\text{red}}\text{H}^+$ intermediate, formed by protonating the pendant amine and internal ET to the proximal Fe of the bimetallic center so that the diiron core is now in the $[\text{Fe}^{\text{I}}\text{Fe}^{\text{I}}]$ state.^{34, 54} From the $\text{H}_{\text{red}}\text{H}^+$ intermediate state, it has been demonstrated that the active site can undergo a second ET step form $\text{H}_{\text{sred}}\text{H}^+$ intermediate or a “super-reduced” state which is characterized as having a protonated pendant amine, a one-electron reduced Fe_4S_4 cluster and a $[\text{Fe}^{\text{I}}\text{Fe}^{\text{I}}]$ core.^{32, 55} It has been suggested that the $\text{H}_{\text{sred}}\text{H}^+$ intermediate can undergo tautomerization to form the H_{hyd} intermediate state⁵⁶, characterized by an oxidized H-cluster, with a hydride coordinated to the distal Fe of the diiron core.⁵⁷ The final intermediate state suggested in the [FeFe] hydrogenase catalytic cycle, is the $\text{H}_{\text{hyd}}\text{H}^+$ intermediate. $\text{H}_{\text{hyd}}\text{H}^+$ is described as having a protonated pendant amine in addition to the terminal hydride observed in the H_{hyd} state and is also proposed to be the final intermediate state the enzyme occupies prior to the formation of a molecule of H_2 .^{42, 52} At this step, it is generally accepted that the proton and hydride combine to form one hydrogen molecule which is released from the active site, to

regenerate the H_{ox} intermediate state. The descriptions of these intermediates is still the source of controversy despite the considerable experimental evidence available to identify and characterize these states.

1.5 The “Potential Jump” Method for sub-Turnover Kinetics Analysis

To study [FeFe] hydrogenase on a time scale relevant for monitoring intermediate populations (ms to μ s), the method of triggering catalysis must itself be on an equivalent time scale (sub μ s). To date, several approaches have been developed and employed for this purpose. For the study of hydrogenase enzymes, the substrates are protons and electrons and thus, by varying the pH of the sample at the time of sample prep, allowing the active site to become equilibrated with the concentration of protons in solution, the trigger can then become the release of electrons into solution. Previously, Brown et al. laid much of the groundwork for a technique which utilizes light as a means to initiate turnover via ET to hydrogenase, fast enough so that changes in intermediate populations could be observed.^{38, 58-65} Broadly speaking, this was accomplished by coupling a photosensitizing nanomaterial, CdTe quantum dots or CdS nanorods, to the enzyme.³³ Upon light exposure, the photosensitizer enters an excited state, from which an electron can be extracted, and is then delivered to the catalyst by direct electron injection, either by electronic tunneling or hopping from the donor to the acceptor.

There are two requirements critical to making this approach successful. The first is that the excited state of the photosensitizer must last long enough to allow the fast ET step to occur. The second is that there must be sufficient driving force for delivery of each electron, to ensure ET in the forward direction. This pathway is outlined in a generic schematic in Fig. 1.5 below.^{16, 64, 66} Greene’s work initially began by using CdTe quantum dots as the photosensitizer, and relied on the electrostatic interaction between hydrogenase and the negatively charged quantum dots to

facilitate the ET between the two components. With this approach, he was able to successfully demonstrate this light-driven method as effective in driving catalysis in hydrogenase, and thus reproduced similarly successful works by Brown et al.^{61, 64-65} However, the overall efficiency of this system was quite poor, only managing a quantum efficiency of less than 10%. Such a poor result is in line with methods which follow this direct electron injection approach. A far more efficient approach to this light triggering method is to include the use of a small molecule to act as an electron shuttle between the photosensitizer and hydrogenase enzyme.

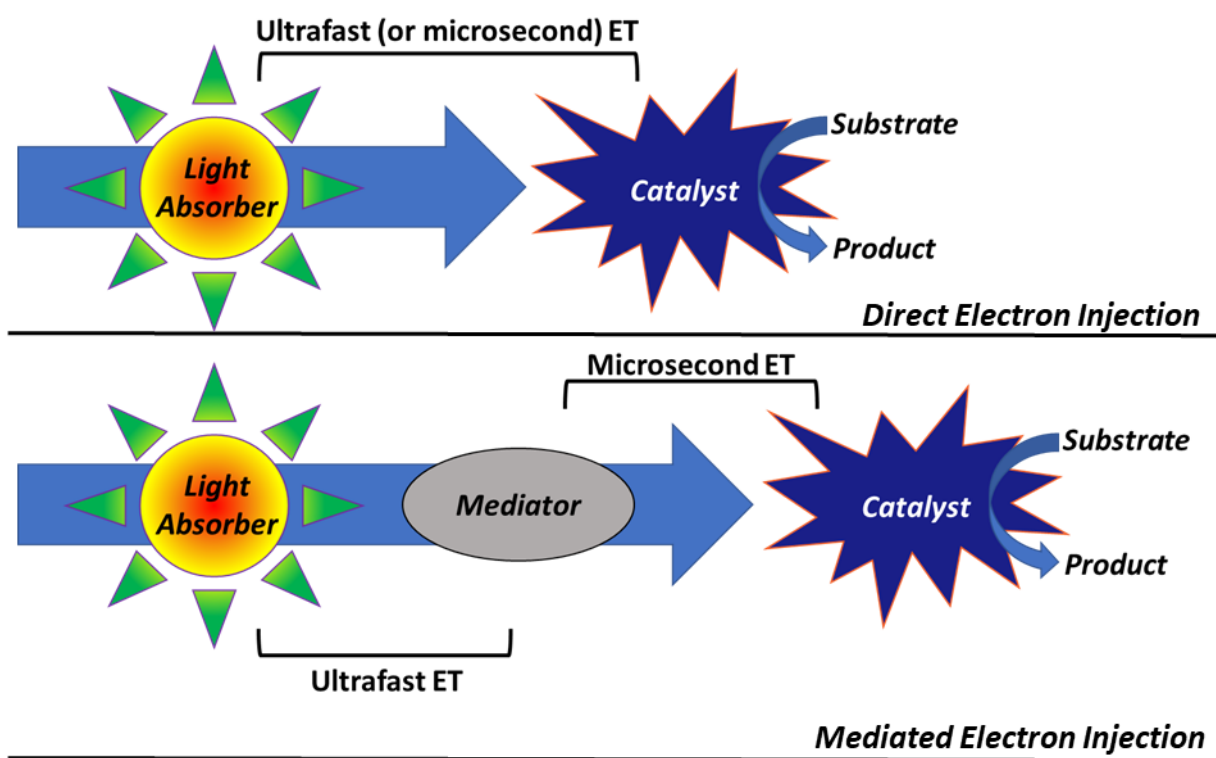


Figure 1.5 Generic Potential jump diagram comparing a direct electron injection method with a mediated electron injection method. A light absorber, in this case, a semiconductor nanocrystalline material absorbs strongly in the UV-to-Visible region forming an excited state. The excited-state electron is quenched by an electron shuttle or mediator. The mediator delivers the reducing equivalent to the catalyst inducing turnover. The rates are denoted with brackets. In the direct electron injection method, the mediator is not utilized.

Later, Greene's approach shifted to utilizing NADH and methyl viologen (MV) as the pair of choice to achieve the desired potential jump.⁵⁸⁻⁵⁹ With this adjustment he was able to resolve changes in intermediate populations and establish a unique mechanistic model based exclusively on these kinetics measurements.⁵⁹ Again, the photosensitizer (NADH in this example) absorbs a laser pulse and enters an excited state where electron transfer to the mediator (MV) can occur. This step happens in approximately less than 10 ns and in doing so, the solution potential drops and results in the establishing of a new equilibrium. This rapid change in solution potential or "*potential jump*" triggers turnover of the enzyme. As successful as the NADH/MV combination has been, it likewise contains an important draw back. Once photolyzed, the NADH in solution could not be reused, ultimately resulting in a sample which contained more byproducts than active participants in the photo-triggering pathway. MV also has a reduction potential (-440 mV) very close to the H₂ couple of hydrogenase. This ultimately results in a lack of driving force for forward ET from MV to hydrogenase, limiting the overall efficiency.

Along with NADH, a different class of photosensitizer and mediator has been used to drive catalysis and recently has been used to study hydrogenase.⁶⁷ The newly adopted photosensitizer is a CdSe based nanocrystalline semiconductor with a CdS shell in the form of a dot-in-rod nanostructure. These materials have the advantage of being very strong absorbers in the UV and visible (extinction coefficient > 100,000).⁶⁸

In 2017, Chica et al was able to demonstrate the advantage of incorporating these high absorbing photosensitizers and capturing their reducing power with a low potential viologen based mediator, PDQ or DQ03 as it will be referred to for the rest of the thesis. These materials have relatively long lived excited states allowing for facile ET to a small molecule quencher

facile which occurs with near unity quantum efficiency for those small molecules studied.^{67, 69-70}

In his work, he compared the efficiency of using MV to DQ03 for driving catalysis with SHI [NiFe] hydrogenase. The results plainly demonstrated that DQ03 behaved as a more efficient mediator for driving catalysis, due to the enhanced driving force the lower potential mediator provided. This resulted in a net increase in ET to the enzyme, whereas MV did not exhibit strong ET properties to hydrogenase because of the lack of driving force for ET to the enzyme.⁶⁷ For these reasons, Chica's work established new records for driving hydrogen production with an unprecedented quantum efficiency of 65%, at room temperature and close to neutral conditions.

1.6 Goals and Scope of Thesis

As described above, the combination of a strongly absorbing photosensitizer and mediator yielded a powerful approach, not only for driving catalysis, but also for detailed mechanistic studies. Several groups have demonstrated this and have had moderate success by incorporating these methods and employing them to study a wide variety of systems. There are nevertheless several remaining areas of confusion and ambiguity regarding the nature of the interaction between system components (mediator, photosensitizer, and catalyst). It remains to be seen how manipulating these components might improve or hinder ET. A few of the lingering questions can be described as follows: How do the structural and electronic properties of the mediator influence electron extraction from the photosensitizer and ET to the catalyst? What modifications to the photosensitizer can be made to expand the excitation sources available to us, and will it perform with the same efficiency? How do these manipulations effect the interpretation of mechanistic studies? The aim of this thesis is to begin answering these questions by characterizing the relevant component interactions utilizing an array of steady state and

transient spectroscopic techniques as well as to apply this knowledge for the study of hydrogenase enzymes.

In chapters 3 and 4, a series of studies designed to characterize several poorly understood mediators was undertaken. These involved incorporating the mediators of interest into a photocatalytic system which utilized nanocrystalline semiconductors as photosensitizers and three different hydrogenase enzymes as model catalysts. The molecules used as mediators were then characterized in detail via a series of analytical and spectroscopic techniques to establish their reactive nature. Their efficiency as electron carriers between photosensitizers and catalysts was also explored to establish their viability in such systems. The mediators studied are bipyridine based molecules with properties similar to MV, but which have the advantage of being easily tunable in structure and reduction potential. Depending on the driving force needed or other system requirements, a mediator can be selected to optimize these properties.

Expanding upon this approach, we incorporated these mediators into our potential jump system as a means of rapidly injecting electrons into a catalyst, to produce a solution potential jump initiating turnover via ET to the enzyme. To examine the influence of sample conditions on the solution potential jump, we subjected a model photocatalytic system to a variety of experimental conditions and measured the influence of these conditions as a function of reducing equivalents generated. For the model photocatalytic system, we selected three redox active molecules covering reduction potentials from -550 mV to -670 mV, CdSe/CdS core-shell nanorods, and an [FeFe] hydrogenase from *Chlamydomonas reinhardtii* (CrHydA1) as our model electron shuttles, photosensitizer and catalyst, respectively. We also utilized an excess concentration of a sacrificial electron donor (mercaptpropionic acid, MPA) as the terminal reductant for this system. With these components, we screened a variety of experimental

conditions such as pH, mediator concentration, protein concentration, photosensitizer concentration and photon flux. By manipulating these experimental conditions, we demonstrated the potential of simple modifications to improve tunability for application to the studying of sensitive systems.

In the final chapter, the principles established through these studies were employed to study the catalytic cycle of two different [FeFe] hydrogenases, the [FeFe] hydrogenase from *Desulfovibrio desulfuricans* (DdHydAB) and the [FeFe] hydrogenase from *Clamydomonas reinhardtii* (CrHydA1). Despite being quite similar in active site composition, these two catalysts, each from different organisms, feature unique properties. These properties indicate that different catalytic mechanisms are likely, as each is able to populate intermediate states with differing degrees of success.

1.7 References

1. Asif, M.; Muneer, T., Energy supply, its demand and security issues for developed and emerging economies. *Renewable and Sustainable Energy Reviews* **2007**, *11* (7), 1388-1413.
2. Cook, T. R.; Dogutan, D. K.; Reece, S. Y.; Surendranath, Y.; Teets, T. S.; Nocera, D. G., Solar Energy Supply and Storage for the Legacy and Nonlegacy Worlds. *Chemical Reviews* **2010**, *110* (11), 6474-6502.
3. Đokić, M.; Soo, H. S., Artificial photosynthesis by light absorption, charge separation, and multielectron catalysis. *Chemical Communications* **2018**, *54* (50), 6554-6572.
4. Hambourger, M.; Moore, G. F.; Kramer, D. M.; Gust, D.; Moore, A. L.; Moore, T. A., Biology and technology for photochemical fuel production. *Chemical Society Reviews* **2009**, *38* (1), 25-35.
5. Graetz, J., New approaches to hydrogen storage. *Chemical Society Reviews* **2009**, *38* (1), 73-82.
6. Nocera, D. G., Living healthy on a dying planet. *Chemical Society Reviews* **2009**, *38* (1), 13-15.
7. Pratt, C.; Tate, K., Mitigating Methane: Emerging Technologies To Combat Climate Change's Second Leading Contributor. *Environmental Science & Technology* **2018**, *52* (11), 6084-6097.
8. Shindell, D. T.; Faluvegi, G.; Koch, D. M.; Schmidt, G. A.; Unger, N.; Bauer, S. E., Improved Attribution of Climate Forcing to Emissions. **2009**, *326* (5953), 716-718.
9. Tang, P.; Zhu, Q.; Wu, Z.; Ma, D., Methane activation: the past and future. *Energy & Environmental Science* **2014**, *7* (8), 2580-2591.

10. Han, Z.; Eisenberg, R., Fuel from Water: The Photochemical Generation of Hydrogen from Water. *Accounts of Chemical Research* **2014**, *47* (8), 2537-2544.
11. Barber, J., Photosynthetic energy conversion: natural and artificial. *Chemical Society Reviews* **2009**, *38* (1), 185-196.
12. Lubitz, W.; Ogata, H.; Rüdiger, O.; Reijerse, E., Hydrogenases. *Chemical Reviews* **2014**, *114* (8), 4081–4148.
13. Banerjee, R.; Jones, J. C.; Lipscomb, J. D., Soluble Methane Monooxygenase. *Annual Review of Biochemistry* **2019**.
14. Wang, V. C. C.; Maji, S.; Chen, P. P. Y.; Lee, H. K.; Yu, S. S. F.; Chan, S. I., Alkane Oxidation: Methane Monooxygenases, Related Enzymes, and Their Biomimetics. *Chemical Reviews* **2017**, *117* (13), 8574-8621.
15. Marchetti, L.; Levine, M., Biomimetic Catalysis. *ACS Catalysis* **2011**, *1* (9), 1090-1118.
16. Evans, R. M.; Siritanaratkul, B.; Megarity, C. F.; Pandey, K.; Esterle, T. F.; Badiani, S.; Armstrong, F. A., The value of enzymes in solar fuels research – efficient electrocatalysts through evolution. *Chemical Society Reviews* **2019**, *48* (7), 2039-2052.
17. Cai, R.; Minteer, S. D., Nitrogenase Bioelectrocatalysis: From Understanding Electron-Transfer Mechanisms to Energy Applications. *ACS Energy Letters* **2018**, *3* (11), 2736-2742.
18. Kaeffer, N.; Chavarot-Kerlidou, M.; Artero, V., Hydrogen Evolution Catalyzed by Cobalt Diimine–Dioxime Complexes. *Accounts of Chemical Research* **2015**, *48* (5), 1286-1295.
19. Hammarström, L.; Wasielewski, M. R., Biomimetic approaches to artificial photosynthesis. *Energy & Environmental Science* **2011**, *4* (7), 2339-2339.

20. Woolerton, T. W.; Sheard, S.; Chaudhary, Y. S.; Armstrong, F. A., Enzymes and bio-inspired electrocatalysts in solar fuel devices. *Energy & Environmental Science* **2012**, *5* (6), 7470-7490.
21. Ahmed, M. E.; Dey, S.; Darensbourg, M. Y.; Dey, A., Oxygen-Tolerant H₂ Production by [FeFe]-H₂ase Active Site Mimics Aided by Second Sphere Proton Shuttle. *Journal of the American Chemical Society* **2018**, *140* (39), 12457-12468.
22. Le, J. M.; Bren, K. L., Engineered Enzymes and Bioinspired Catalysts for Energy Conversion. *ACS Energy Letters* **2019**, *4* (9), 2168-2180.
23. Davis, H. J.; Ward, T. R., Artificial Metalloenzymes: Challenges and Opportunities. *ACS Central Science* **2019**, *5* (7), 1120-1136.
24. Hammes-Schiffer, S., Proton-Coupled Electron Transfer: Moving Together and Charging Forward. *Journal of the American Chemical Society* **2015**.
25. Duan, J.; Senger, M.; Esselborn, J.; Engelbrecht, V.; Wittkamp, F.; Apfel, U.-P.; Hofmann, E.; Stripp, S. T.; Happe, T.; Winkler, M., Crystallographic and spectroscopic assignment of the proton transfer pathway in [FeFe]-hydrogenases. *Nature Communications* **2018**, *9* (1), 4726.
26. Mebs, S.; Duan, J.; Wittkamp, F.; Stripp, S. T.; Happe, T.; Apfel, U.-P.; Winkler, M.; Haumann, M., Differential Protonation at the Catalytic Six-Iron Cofactor of [FeFe]-Hydrogenases Revealed by ⁵⁷Fe Nuclear Resonance X-ray Scattering and Quantum Mechanics/Molecular Mechanics Analyses. *Inorganic Chemistry* **2019**, *58* (6), 4000-4013.
27. Senger, M.; Mebs, S.; Duan, J.; Wittkamp, F.; Apfel, U.-P.; Heberle, J.; Haumann, M.; Stripp, S. T., Stepwise isotope editing of [FeFe]-hydrogenases exposes cofactor dynamics. *Proceedings of the National Academy of Sciences* **2016**, *113* (30), 8454.

28. Siebel, J. F.; Adamska-Venkatesh, A.; Weber, K.; Rumpel, S.; Reijerse, E.; Lubitz, W., Hybrid [FeFe]-Hydrogenases with Modified Active Sites Show Remarkable Residual Enzymatic Activity. *Biochemistry* **2015**, *54* (7), 1474-1483.
29. Sickerman, N. S.; Hu, Y., Hydrogenases. *Methods Mol Biol* **2019**, *1876*, 65-88.
30. Haumann, M.; Stripp, S. T., The Molecular Proceedings of Biological Hydrogen Turnover. *Accounts of Chemical Research* **2018**.
31. Poudel, S.; Tokmina-Lukaszewska, M.; Colman, D. R.; Refai, M.; Schut, G. J.; King, P. W.; Maness, P.-C.; Adams, M. W. W.; Peters, J. W.; Bothner, B.; Boyd, E. S., Unification of [FeFe]-hydrogenases into three structural and functional groups. *Biochimica et Biophysica Acta (BBA) - General Subjects* **2016**, *1860* (9), 1910-1921.
32. Adamska, A.; Silakov, A.; Lambertz, C.; Rudiger, O.; Happe, T.; Reijerse, E.; Lubitz, W., Identification and characterization of the "super-reduced" state of the H-cluster in [FeFe] hydrogenase: a new building block for the catalytic cycle? *Angewandte Chemie International Edition* **2012**, *51* (46), 11458-62.
33. Berggren, G.; Adamska, A.; Lambertz, C.; Simmons, T. R.; Esselborn, J.; Atta, M.; Gambarelli, S.; Mouesca, J. M.; Reijerse, E.; Lubitz, W.; Happe, T.; Artero, V.; Fontecave, M., Biomimetic assembly and activation of [FeFe]-hydrogenases. *Nature* **2013**, *499*, 66.
34. Rodríguez-Maciá, P.; Pawlak, K.; Rüdiger, O.; Reijerse, E. J.; Lubitz, W.; Birrell, J. A., Intercluster Redox Coupling Influences Protonation at the H-cluster in [FeFe] Hydrogenases. *Journal of the American Chemical Society* **2017**, *139* (42), 15122-15134.
35. Senger, M.; Eichmann, V.; Laun, K.; Duan, J.; Wittkamp, F.; Knör, G.; Apfel, U.-P.; Happe, T.; Winkler, M.; Heberle, J.; Stripp, S. T., How [FeFe]-Hydrogenase Facilitates

Bidirectional Proton Transfer. *Journal of the American Chemical Society* **2019**, *141* (43), 17394-17403.

36. Wittkamp, F.; Senger, M.; Stripp, S. T.; Apfel, U. P., [FeFe]-Hydrogenases: recent developments and future perspectives. *Chemical Communications* **2018**, *54* (47), 5934-5942.

37. Sanchez, M. L. K.; Sommer, C.; Reijerse, E.; Birrell, J. A.; Lubitz, W.; Dyer, R. B., Investigating the Kinetic Competency of CrHydA1 [FeFe] Hydrogenase Intermediate States via Time-Resolved Infrared Spectroscopy. *Journal of the American Chemical Society* **2019**, *141* (40), 16064-16070.

38. Greene, B. L.; Vansuch, G. E.; Chica, B. C.; Adams, M. W. W.; Dyer, R. B., Applications of Photogating and Time Resolved Spectroscopy to Mechanistic Studies of Hydrogenases. *Accounts of Chemical Research* **2017**, *50* (11), 2718-2726.

39. Senger, M.; Mebs, S.; Duan, J.; Shulenina, O.; Laun, K.; Kertess, L.; Wittkamp, F.; Apfel, U.-P.; Happe, T.; Winkler, M.; Haumann, M.; Stripp, S. T., Protonation/reduction dynamics at the [4Fe-4S] cluster of the hydrogen-forming cofactor in [FeFe]-hydrogenases. *Physical Chemistry Chemical Physics* **2018**, *20* (5), 3128-3140.

40. Senger, M.; Mebs, S.; Duan, J.; Shulenina, O.; Laun, K.; Kertess, L.; Wittkamp, F.; Apfel, U.-P.; Happe, T.; Winkler, M.; Haumann, M.; Stripp, S. T., Protonation/reduction dynamics at the [4Fe-4S] cluster of the hydrogen-forming cofactor in [FeFe]-hydrogenases. *Physical Chemistry Chemical Physics* **2018**, *20* (5), 3128-3140.

41. Cramer Stephen, P.; Pham Cindy, C.; Mulder David, W.; Pelmeshnikov, V.; King Paul, W.; Ratzloff Michael, W.; Wang, H.; Mishra, N.; Alp, E.; Zhao, J.; Hu Michael, Y.; Tamasaku, K.; Yoda, Y., Terminal Hydride Species in [FeFe]-Hydrogenases are Vibrationally Coupled to the Active Site Environment. *Angewandte Chemie International Edition* **2018**, *0* (ja).

42. Birrell, J. A.; Pelmeshnikov, V.; Mishra, N.; Wang, H.; Yoda, Y.; Tamasaku, K.; Rauchfuss, T. B.; Cramer, S. P.; Lubitz, W.; DeBeer, S., Spectroscopic and Computational Evidence that [FeFe] Hydrogenases Operate Exclusively with CO-Bridged Intermediates. *Journal of the American Chemical Society* **2020**, *142* (1), 222-232.
43. Rodríguez-Maciá, P.; Reijerse, E. J.; van Gestel, M.; DeBeer, S.; Lubitz, W.; Rüdiger, O.; Birrell, J. A., Sulfide Protects [FeFe] Hydrogenases From O₂. *Journal of the American Chemical Society* **2018**, *140* (30), 9346-9350.
44. Caserta, G.; Papini, C.; Adamska-Venkatesh, A.; Pecqueur, L.; Sommer, C.; Reijerse, E.; Lubitz, W.; Gauquelin, C.; Meynial-Salles, I.; Pramanik, D.; Artero, V.; Atta, M.; del Barrio, M.; Faivre, B.; Fourmond, V.; Léger, C.; Fontecave, M., Engineering an [FeFe]-Hydrogenase: Do Accessory Clusters Influence O₂ Resistance and Catalytic Bias? *Journal of the American Chemical Society* **2018**, *140* (16), 5516-5526.
45. Sommer, C.; Richers, C. P.; Lubitz, W.; Rauchfuss, T. B.; Reijerse, E. J., A [RuRu] Analogue of an [FeFe]-Hydrogenase Traps the Key Hydride Intermediate of the Catalytic Cycle. *Angewandte Chemie* **2018**, *130* (19), 5527-5530.
46. Mulder, D. W.; Guo, Y. S.; Ratzloff, M. W.; King, P. W., Identification of a Catalytic Iron-Hydride at the H-Cluster of [FeFe]-Hydrogenase. *Journal of the American Chemical Society* **2017**, *139* (1), 83-86.
47. Ghirardi, M. L.; Dubini, A.; Yu, J.; Maness, P.-C., Photobiological hydrogen-producing systems. *Chemical Society Reviews* **2009**, *38* (1), 52-61.
48. Rodríguez-Maciá, P.; Kertess, L.; Burnik, J.; Birrell, J. A.; Hofmann, E.; Lubitz, W.; Happe, T.; Rüdiger, O., His-Ligation to the [4Fe-4S] Subcluster Tunes the Catalytic Bias of [FeFe] Hydrogenase. *Journal of the American Chemical Society* **2019**, *141* (1), 472-481.

49. Land, H.; Senger, M.; Berggren, G.; Stripp, S. T., Current State of [FeFe]-Hydrogenase Research: Biodiversity and Spectroscopic Investigations. *ACS Catalysis* **2020**, 7069-7086.
50. Yasui, S.; Itoh, K.; Ohno, A.; Tokitoh, N., Effect of structural change in viologen acceptors on the rate of single electron transfer from tributylphosphine. *Organic & Biomolecular Chemistry* **2006**, 4 (15), 2928-2931.
51. Artz, J. H.; Zadvornyy, O. A.; Mulder, D. W.; Keable, S. M.; Cohen, A. E.; Ratzloff, M. W.; Williams, S. G.; Ginovska, B.; Kumar, N.; Song, J.; McPhillips, S. E.; Davidson, C. M.; Lyubimov, A. Y.; Pence, N.; Schut, G. J.; Jones, A. K.; Soltis, S. M.; Adams, M. W. W.; Raugei, S.; King, P. W.; Peters, J. W., Tuning Catalytic Bias of Hydrogen Gas Producing Hydrogenases. *Journal of the American Chemical Society* **2019**.
52. Ratzloff, M. W.; Artz, J. H.; Mulder, D. W.; Collins, R. T.; Furtak, T. E.; King, P. W., CO-Bridged H-Cluster Intermediates in the Catalytic Mechanism of [FeFe]-Hydrogenase CaI. *Journal of the American Chemical Society* **2018**, 140 (24), 7623-7628.
53. Senger, M.; Laun, K.; Wittkamp, F.; Duan, J.; Haumann, M.; Happe, T.; Winkler, M.; Apfel, U.-P.; Stripp, S. T., Proton-Coupled Reduction of the Catalytic [4Fe-4S] Cluster in [FeFe]-Hydrogenases. *Angewandte Chemie International Edition* **2017**, 56 (52), 16503-16506.
54. Adamska-Venkatesh, A.; Krawietz, D.; Siebel, J.; Weber, K.; Happe, T.; Reijerse, E.; Lubitz, W., New Redox States Observed in [FeFe] Hydrogenases Reveal Redox Coupling Within the H-Cluster. *Journal of the American Chemical Society* **2014**, 136 (32), 11339-11346.
55. Sommer, C.; Adamska-Venkatesh, A.; Pawlak, K.; Birrell, J. A.; Rudiger, O.; Reijerse, E. J.; Lubitz, W., Proton Coupled Electronic Rearrangement within the H-Cluster as an Essential Step in the Catalytic Cycle of [FeFe] Hydrogenases. *J. Am. Chem. Soc.* **2017**, 139 (4), 1440-1443.

56. Wiedner, E. S., Thermodynamic Hydricity of [FeFe]-Hydrogenases. *Journal of the American Chemical Society* **2019**, *141* (18), 7212-7222.
57. Rumpel, S.; Sommer, C.; Reijerse, E.; Farès, C.; Lubitz, W., Direct Detection of the Terminal Hydride Intermediate in [FeFe] Hydrogenase by NMR Spectroscopy. *Journal of the American Chemical Society* **2018**, *140* (11), 3863-3866.
58. Greene, B. L.; Schut, G. J.; Adams, M. W. W.; Dyer, R. B., Pre-Steady-State Kinetics of Catalytic Intermediates of an [FeFe]-Hydrogenase. *ACS Catalysis* **2017**, *7* (3), 2145-2150.
59. Greene, B. L.; Wu, C.-H.; McTernan, P. M.; Adams, M. W. W.; Dyer, R. B., Proton-Coupled Electron Transfer Dynamics in the Catalytic Mechanism of a [NiFe]-Hydrogenase. *Journal of the American Chemical Society* **2015**, *137* (13), 4558-4566.
60. Greene, B. L.; Joseph, C. A.; Maroney, M. J.; Dyer, R. B., Direct Evidence of Active-Site Reduction and Photodriven Catalysis in Sensitized Hydrogenase Assemblies. *Journal of the American Chemical Society* **2012**, *134* (27), 11108-11111.
61. Brown, K. A.; Harris, D. F.; Wilker, M. B.; Rasmussen, A.; Khadka, N.; Hamby, H.; Keable, S.; Dukovic, G.; Peters, J. W.; Seefeldt, L. C.; King, P. W., Light-driven dinitrogen reduction catalyzed by a CdS:nitrogenase MoFe protein biohybrid. *Science* **2016**, *352* (6284), 448.
62. Brown, K. A.; Wilker, M. B.; Boehm, M.; Hamby, H.; Dukovic, G.; King, P. W., Photocatalytic Regeneration of Nicotinamide Cofactors by Quantum Dot–Enzyme Biohybrid Complexes. *ACS Catalysis* **2016**, *6* (4), 2201-2204.
63. Wilker, M. B.; Shinopoulos, K. E.; Brown, K. A.; Mulder, D. W.; King, P. W.; Dukovic, G., Electron Transfer Kinetics in CdS Nanorod–[FeFe]-Hydrogenase Complexes and

Implications for Photochemical H₂ Generation. *Journal of the American Chemical Society* **2014**, *136* (11), 4316-4324.

64. Brown, K. A.; Wilker, M. B.; Boehm, M.; Dukovic, G.; King, P. W., Characterization of Photochemical Processes for H₂ Production by CdS Nanorod–[FeFe] Hydrogenase Complexes. *Journal of the American Chemical Society* **2012**, *134* (12), 5627-5636.

65. Brown, K. A.; Dayal, S.; Ai, X.; Rumbles, G.; King, P. W., Controlled Assembly of Hydrogenase-CdTe Nanocrystal Hybrids for Solar Hydrogen Production. *Journal of the American Chemical Society* **2010**, *132* (28), 9672-9680.

66. Reisner, E.; Powell, D. J.; Cavazza, C.; Fontecilla-Camps, J. C.; Armstrong, F. A., Visible Light-Driven H₂ Production by Hydrogenases Attached to Dye-Sensitized TiO₂ Nanoparticles. *Journal of the American Chemical Society* **2009**, *131* (51), 18457-18466.

67. Chica, B.; Wu, C.-H.; Liu, Y.; Adams, M. W. W.; Lian, T.; Dyer, R. B., Balancing electron transfer rate and driving force for efficient photocatalytic hydrogen production in CdSe/CdS nanorod–[NiFe] hydrogenase assemblies. *Energy & Environmental Science* **2017**, *10* (10), 2245-2255.

68. Talapin, D. V.; Koeppel, R.; Götzinger, S.; Kornowski, A.; Lupton, J. M.; Rogach, A. L.; Benson, O.; Feldmann, J.; Weller, H., Highly Emissive Colloidal CdSe/CdS Heterostructures of Mixed Dimensionality. *Nano Letters* **2003**, *3* (12), 1677-1681.

69. Zhao, F.; Li, Q.; Han, K.; Lian, T., Mechanism of Efficient Viologen Radical Generation by Ultrafast Electron Transfer from CdS Quantum Dots. *The Journal of Physical Chemistry C* **2018**, *122* (30), 17136-17142.

70. Zhu, H.; Song, N.; Lv, H.; Hill, C. L.; Lian, T., Near Unity Quantum Yield of Light-Driven Redox Mediator Reduction and Efficient H₂ Generation Using Colloidal Nanorod Heterostructures. *Journal of the American Chemical Society* **2012**, *134* (28), 11701-11708.

Chapter 2

Materials and Methods

Aspects have been reproduced from Ref. 8 with permission from the Royal Society of Chemistry

Also

Reproduced in part with permission from

Monica L. K. Sanchez,[†] Constanze Sommer,[‡] Edward Reijerse,[‡] James A. Birrell,^{‡*} Wolfgang

Lubitz,^{‡*} R. Brian Dyer^{†*} Investigating the Kinetic Competency of CrHydA1 [FeFe]

Hydrogenase Intermediate States via Time-resolved Infrared Spectroscopy. *Journal of the*

American Chemical Society **2019**, 141 (40), 16064-16070

copyright 2019 American Chemical Society

2.1 Introduction

This chapter describes several experimental methods used for examining steady state and pre-steady state kinetics of several different electron transfer processes. It also describes the techniques used to measure spectroscopic and physical features of hydrogenases, redox mediators, photosensitizer materials and other chemical tools used for photo-initiation experiments described in the following chapters. A wide variety of analytical techniques were required to develop and apply this methodology due to the challenging nature of the specific kinetic processes measured. This chapter is divided into 7 sections concerning the synthesis of photosensitizer and mediator materials used, analytical methods, assays and procedures for data analysis and processing.

[FeFe] hydrogenase enzyme expression and purification from the organisms *Chlamydomonas reinhardtii* (CrHydA1) and *Desulfovibrio desulfuricans* (DdHydAB) was performed by Dr. James Birrell, Dr. Constanze Sommer, and Nina Breuer working in Prof. Wolfgang Lubitz's lab at the Max Plank Institute for Chemical Energy Conversion. *Pyrococcus furiosus* SHI [NiFe] Hydrogenase enzyme was performed by Dr. Chang-Hao "Perry" Wu working in Prof. Michael W. W. Adams lab at the University of Georgia. These enzymes were used throughout this thesis.

Additional chemicals were used as received from standard commercial sources. Nanomaterials utilized throughout this thesis were synthesized according to procedures inspired from previous publications¹⁻⁵. The spectroscopic techniques used to physically characterize materials included: UV-Vis absorbance, Fourier-Transformed Infrared (FTIR) spectroscopy, emission spectra, NMR, electrochemical techniques (such as cyclic voltammetry and chronopotentiometry), and transmission electron microscopy (TEM). Time resolved applications

of visible, infrared and fluorescence spectroscopy were used extensively throughout this thesis as well. Finally, methods for experimentally determining enzyme rate constants and kinetic parameters, which are used in chapters 3-5, are more thoroughly detailed in those chapters.

2.2 Mediator Synthesis

The mediators used in the chapters of this thesis were chosen for their unique combination of structural and electronic characteristics and are summarized in Figure 2.1. Every mediator presented was synthesized and characterized using chemicals purchased from Sigma Aldrich and characterized using core facilities in the Emory chemistry department including NMR and X-ray crystallography. While the methodology and experimental details of these techniques are presented in this chapter, analysis and conclusions of this characterization are covered in chapter 3 of this thesis.

The nomenclature that is used throughout this thesis (including in Figure 2.1) to describe the redox mediators, refers to the physical features of each molecule. The “DQ-” prefix refers to “diquat” as a description of the bipyridine core.⁶ The two numbers following “DQ” denote the combination of substituents that differentiate these molecules structurally and electronically. The first number refers to the position of the methyl groups, i.e. “5” refers to methyl groups being in the 5 position and “4” refers to methyl groups in the 4-position. A “0” denotes that there are no additional methyl groups in the core. The second number refers to the length of the carbon chain connecting the nitrogens of the bipyridine, e.g. a “2” corresponds to 2-carbon atom length chain and a “3” corresponds to a 3-carbon length chain. So, for example, DQ52 describes a

bipyridine molecule with methyl groups in the 5-position on the bipyridine core and 2-carbon linker chain between the two nitrogens of the pyridine ring.

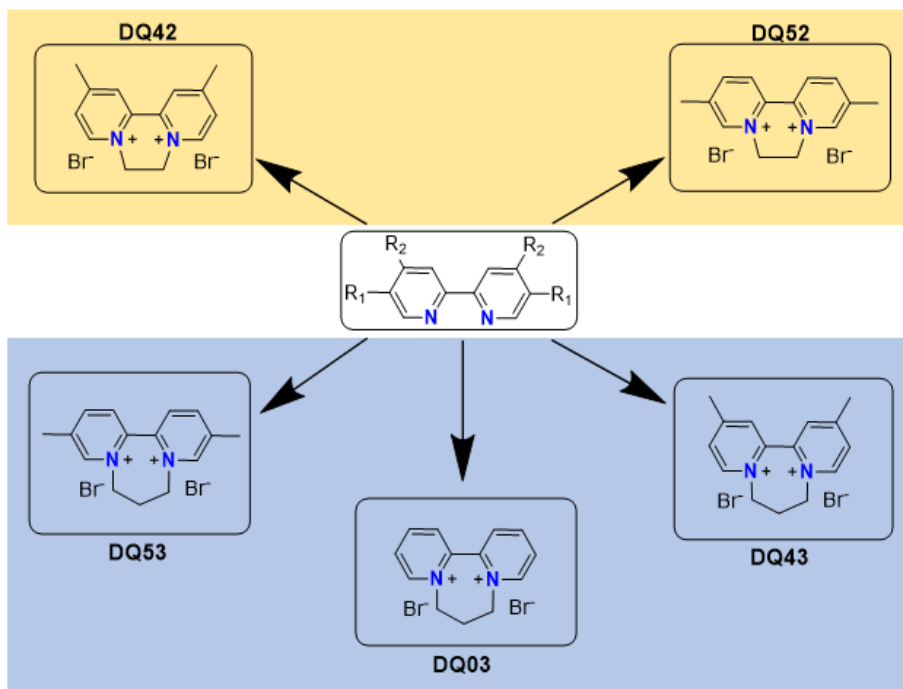


Figure 2.1 Summary of Synthetic Pathways for Mediators Synthesis. Summary of synthetic pathways to synthesize the small molecule redox mediators discussed throughout this thesis. The colored blocks denote the different cyclizing solvents (dibromoethane vs. dibromopropane) used to synthesize the corresponding mediator. Light yellow = dibromoethane, light blue = dibromopropane. The R_x designation refers to methyl group placement.

2.2.1 Preparation of 2-Carbon Linker Mediators: DQ52 and DQ42

Procedure used for synthesis of the two carbon linker molecules was inspired by literature procedure and subsequently modified.⁷ To an air free 3-neck round bottom flask, 5 mL of 1,2-dibromoethane and 0.25g of 4,4'-dimethyl-2,2'-bipyridine (for DQ42, or 5,5'-dimethyl-2,2'-bipyridine for DQ52). The reaction mixture was refluxed at 125 °C and allowed to react for

12-18 hrs at which point a large amount of pale-yellow precipitate had formed within the flask. After reaction ran to completion, the vessel was cooled with an ice bath and the solid collected on a frit. Excess reagents were washed from the product with cold acetone and hexane. The final product was crystallized from methanol and characterized. The crystals collected were off white. Yield: 62% NMR spectra of the resulting compounds were obtained and are included in Chapter 3.

2.2.2 Preparation of 3-Carbon Linker Mediators: DQ03, DQ43, and DQ53

Procedure used for synthesis of the three-carbon linker molecules was inspired by literature procedure and subsequently modified.⁷ To an air free 3-neck round bottom flask, 5 mL of 1,3-dibromopropane and 0.25g of 4,4'-dimethyl-2,2'-bipyridine (or 5,5'-dimethyl-2,2'-bipyridine for DQ53 or 2,2'-bipyridine for DQ03). The reaction mixture was refluxed at 100-110 °C and allowed to react for 3-5 hrs at which point a large amount of pale-yellow precipitate had formed within the flask. After reaction ran to completion, the vessel was cooled with an ice bath and the solid collected on a frit. Excess reagents were washed from the product with cold acetone and hexane. The final product was crystallized from methanol/ethanol and characterized. The crystals collected were off white or yellow. Yield: 73% NMR spectra of the resulting compounds were obtained and are included at the end of Chapter 3, pages 81-85.

2.3 Synthesis of Nanomaterials: CdSe QDs, CdSe/CdS Dot-in-Rod and CdSe nanorods

Several kinds of photosensitizing nanomaterials were used throughout this thesis and were characterized using UV-vis absorbance spectroscopy, fluorescence emission, and TEM imaging to verify the size, morphology, and electronic characteristics of the particles. While the technical details are described in this chapter, results and analysis of these data are presented in the corresponding chapters.

2.3.1 Preparation of CdSe Quantum Dots

The procedure used for the synthesis of CdSe QDs is similar to the previously reported one.^{1, 8} Briefly, Cadmium Oxide (CdO) (0.06 g), Trioctylphosphine oxide (TOPO) (3 g), and Octadecylphosphonic acid (ODPA, purchased from Alfa Aesar) (0.28 g) were combined in a 3-neck flask and put under vacuum while heating to 150 °C for 1.5 hrs. After this initial reaction period, the reaction vessel was put under a N₂ atmosphere. Once under N₂, the flask was heated to 350 °C until the reaction mixture became clear, indicating that the Cd had fully dissolved in the solvent. Once the reaction mixture was clear, 1.5 mL of trioctylphosphine (TOP) was injected. After the reaction temperature was heated to ~340 °C the Se precursor solution was injected. The Se precursor solution was prepared by dissolving 0.058 g of Se into 0.45 mL of trioctylphosphine (TOP). The reaction was run for 5 min, after which the vessel was removed from heat and cooled to room temperature. The particles were suspended in hexane and stored in the dark until needed.

2.3.2 Preparation of CdSe/CdS Dot-in-rod (DIR) Nanorods

CdSe/CdS DIR nanostructures were synthesized by first synthesizing CdSe cores and growing a CdS shell over the cores. This was accomplished according to a modified literature procedure.¹ Briefly CdO (0.06 g), TOPO (3 g), hexylphosphonic acid (HPA) (0.08 g) and ODPA (0.28 g) were combined in a 3-neck flask and put under vacuum while heating to 150 °C for 2 hrs. After this initial reaction time, the reaction vessel was placed under a N₂ atmosphere. Once under N₂, the flask was heated to 350 °C until the reaction mixture became clear, indicating that the Cd had fully dissolved in the solvent, at which point 1.5 mL of trioctylphosphine (TOP) was injected. Once the reaction temperature recovered (to ~340 °C) the sulfur precursor solution containing the CdSe seeds was injected. The sulfur precursor solution was prepared by dissolving sulfur (0.12 g) into TOP (1.5 mL) along with 2-3 mg of precipitated CdSe seeds. The reaction was run for 5 min. For

slightly larger or smaller particles, the reaction time and temperature were adjusted accordingly. Once the reaction was completed, the vessel was removed from heat and cooled to room temperature. A small volume of hexane or toluene was added to keep the reaction mixture in the solution phase.

The particles were purified by precipitation via centrifugation with methanol and resuspended in chloroform. This procedure was repeated three times to remove excess ligand and unreacted cadmium before proceeding to the ligand exchange reaction.

2.3.3 Preparation of CdSe Nanorods

Procedure was modified from a literature procedure.^{5, 9} Briefly CdO (0.08 g), trioctylphosphine oxide (TOPO) (4.8 g), and hexylphosphonic acid (HPA) (0.7 g) were combined in a three neck flask and put under vacuum while heating to 150 °C and stirring for 2 hrs. After which the reaction vessel was put under N₂ atmosphere. Once under N₂, the flask was heated to 350 °C or until the reaction mixture goes clear indicating that the Cd has fully dissolved in the solvent. Once the reaction mixture is clear the Se precursor solution was injected. The Se precursor solution was prepared by dissolving 0.2 g of Se into 3.6 mL of TOP. Once there was an indication of color change, the vessel was removed from heat and cooled to room temperature (usually 2-3 min). A small addition of hexane will keep the reaction mixture in solution phase.

2.3.4 Ligand Exchange of Nanoparticles for use in Aqueous Media

The nonpolar ligand (TOPO) was exchanged with mercaptopropionic acid (MPA, Sigma Aldrich) via a ligand exchange procedure.^{2, 8} Briefly, 5 mg of purified nanoparticles were refluxed for 2 hrs under N₂ in the dark in 15 mL of methanol with 10 mM MPA. The pH of this reaction mixture had been adjusted to 10 using tetramethyl ammonium hydroxide (TMAOH, Sigma Aldrich) prior to refluxing. After reaction has gone to completion, the exchanged nanorods were then isolated by centrifugation and resuspended in 10 mM MPA, 10 mM tris carboxy ethyl phosphide (TCEP, Sigma Aldrich), 50 mM Borate buffer at pH 8 and stored in an air free environment, in the dark for future use.

2.4.1 Buffers - All buffers used here were prepared using monobasic and dibasic potassium phosphate of analytical grade (J. T. Baker) and pH adjusted using conc NaOH and 10 M HCl and a calibrated pH meter (Mettler Toledo). Salt additions were determined to be less than 10 % of the buffer concentration based on initial pH.

2.5 Analytical Methods

Equipment used for most analytical measurements can be found in the laboratory of R. Brian Dyer. However, TEM images, Proton NMR spectra, and X-ray structures were collected using core facilities in Atwood Chemistry Building or Emerson Hall. Ultrafast and nanosecond TA measurements described in sections 2.5.7 and 2.5.8 were performed using laser systems in the laboratory of Dr. Tianquan “Tim” Lian.

2.5.1 UV/Vis Absorbance

UV-Visible spectra were typically collected on a Lambda 35 UV-Vis spectrophotometer (Perkin Elmer) with a 1 nm slit width and scan speed of 496 nm/min.

UV/vis absorbance spectra of samples were also collected using a modular, home-built fiber coupled spectrometer. Light from a 100 W Xenon lamp was coupled into a solarization resistant optical fiber (Ocean Optics inc.) and directed into a collimating optic typically mounted in a cuvette holder containing the sample. Probe beam levels were selected to maximize sensitivity while avoiding the possibility of probe beam driven photochemistry. The collimated beam passes through the sample and into another fiber coupled collimated optic. This fiber is attached to a spectrometer (QE-6500 Ocean Optics). Absorbance measurements were performed in single beam mode and the reference was a solvent blank or empty air as appropriate.

2.5.2 Photoluminescence Spectra

Fluorescence spectra of luminescent samples were obtained using a Horiba Scientific Dual-FI fluorometer and contained in a quartz fluorescence cuvette purchased from Firefly Sci Cuvette shop. Integration time was typically from 0.1 to 1 s as needed. Excitation wavelength was either 405 nm or 532 nm depending on sample needs.

2.5.3 Fourier Transform Infrared (FTIR) Spectroscopy

FTIR spectra were recorded on a Varian 660 spectrometer using a Mercury Cadmium Telluride (MCT) liquid nitrogen cooled detector external to the sample compartment. The beam is focused on the sample with a gold parabolic mirror, recollimated and then focused onto a liquid nitrogen cooled MCT detector by two more parabolic gold mirrors. Measurements were typically performed with 2 cm^{-1} resolution, were Fourier transformed and ratioed against an appropriate reference in the same sample cell to obtain the absorbance signal. (see equation 2.1) The data were then baseline corrected with a multipoint spline function. The sample was housed in a home-built copper cell with CaF_2 windows with a Teflon spacer of either $50\text{ }\mu\text{m}$ or $75\text{ }\mu\text{m}$ thickness.

$$\Delta A (bs) = -\log\left(\frac{I_{light}}{I_{dark}}\right)$$

Equation 2.1 Equation for determining absorbance from infrared spectra that have been Fourier transformed.

Light titration experiments were performed using the same FTIR spectrometer. Multiple excitation sources were used depending upon experimental needs and photosensitizer used. Excitation sources used included: a diode pumped Q-switched yttrium lithium fluoride (YLF) laser (355nm, CrystaLaser), a diode laser (405 nm, Thor Labs) or a CrystaLaser diode pumped Q-switched 527 nm laser with 20 ns pulses. The laser was located inside the box and aligned with the IR probe beam using a $200\text{ }\mu\text{m}$ pinhole to illuminate the probe volume uniformly. Light exposure was gated by a manually controlled shutter for the desired illumination times. A difference FTIR spectrum was computed from the single beam spectra obtained in the dark (I_{dark}) and after laser illumination (I_{light}) to determine the degree of photoreduction of the hydrogenase.

The “dark” spectrum was obtained for a sample containing protein, nanorods, and mediator that was kept in the dark, whereas the “light” spectrum was obtained by illuminating the same sample for 10s and then collecting the single beam spectrum. Optical spectra could also be collected during light titrations by aligning the collimated visible beam from an optical fiber (ocean optics) with the probe beam and light excitation source.

2.5.4 Transmission Electron Microscopy

Images of nanoparticle samples were collected using core facilities in the Robert P. Akarian Microscopy center. Samples for TEM were prepared by evaporation of purified and concentrated samples of hexane solvated nanorods onto Cu-hole carbon mesh grid films purchased from Electron Microscopy Sciences. The images were collected on a Hitachi 700 microscope with an acceleration voltage of 80 kV. While the methodology is included in this chapter, images of nanorods used in subsequent chapters are included in the relevant chapters.

2.5.5 Time Correlated Single Photon Counting (TCSPC)

Fluorescence decay lifetimes were collected on a Nikon confocal scanning laser microscope interfaced with Picoquant TCSPC electronics. Samples were prepared in an anaerobic chamber on a micro-well plate and sealed with plate sealing film (VWR). Samples in the plate were imaged via the confocal microscope and excited with 405 nm at 1 MHz repetition rate. The emission was passed through a 520 nm long pass filter (Semrock, Razoredge) to remove scattered excitation light. Data were collected until 10,000 counts was reached at the beginning of the decay trace to ensure good signal-to-noise ratio.

$$\tau_{AWL} = \frac{\sum_{k=0}^{n-1} A[k] * \tau[k]}{A_{sum}}$$

Equation 2.2 Equation used to determine the amplitude weighted lifetime (τ_{AWL}) of fluorescence decay measurements. Where, $A[k]$ coefficient describes the amplitude for the $\tau[k]$ derived from the multi-exponential fit and A_{sum} is the sum of amplitudes. Each value is derived from the multi-exponential function used to fit the experimental data.

2.5.6 In tandem Transient IR and Visible Absorbance

The instrument used to collect the nanosecond infrared and visible transient absorbance (TA) data simultaneously has been described previously.¹⁰ Briefly, the pump-probe experiment employs the third harmonic of a Q-switched Nd:YAG laser (10 ns pulse at 355 nm) as the pump pulse and two continuous wave probe lasers, a Quantum Cascade Laser (QCL, Daylight Solutions) operating in the mid-IR (1805-2010 cm^{-1}) and a 785 nm diode laser (ultra-compact diode laser, Toptica Photonics). Scattered light from the excitation source is used to trigger data collection. The time-resolved absorbance of the two probe beams is detected using a fast MCT detector and an avalanche photodiode, respectively. Single shot transients were collected at room temperature using 100 μJ of 355 (or 532) nm light focused to an ≈ 500 μm diameter spot (50 mJ/cm^2). The sample position was shifted to ensure a new sample volume was probed with each laser shot. Typically, an average of 20-25 shots was obtained for every probe wavelength.

Typical samples prepared for potential jump experiments were composed of 50 potassium phosphate buffer, ~ 2 mM enzyme, 50 mM redox mediator, 50 mM mercaptopropionic acid (MPA) sacrificial electron donor and CdSe/CdS nanorods with O.D. ~ 0.3 at 355 nm or 532

nm. The reference sample was prepared identically except with deoxymyoglobin (deoxyMb) instead of [FeFe] hydrogenase. The pump pulse slightly heats the water (1-2 °C temperature jump due to nonradiative relaxation of excess pump energy), producing a transient IR background signal (due to the temperature dependence of the mid-IR water absorbance) that rises within 10 ns and decays on the 1 ms timescale. The pump pulse slightly heats the water (1-2 °C temperature jump due to nonradiative relaxation of excess pump energy), producing a transient IR background signal (due to the temperature dependence of the mid-IR water absorbance) that rises within 10 ns and decays on the 1 ms timescale. To account for this, deoxyMb was used in these experiments as a protein-based UV absorber that has minimal interaction with the mediator to match the optical density at the pump wavelength relative to the hydrogenase samples. The reference absorbs the pump beam identically to the sample (protein plus photosensitizer absorbance) and thus matches the inner filter effect of the protein in the transient absorbance measurements and the solvent heating effect in the TRIR measurements.¹¹

2.5.7 Ultrafast Transient Visible Absorbance

Ultrafast transient absorbance measurements were made at room temperature using a Helios Spectrometer with pump and probe beams derived from an amplified Ti:Sapphire laser system (Coherent Legend, 800 nm, 150 fs, 2.4 mJ/pulse, and 1 kHz repetition rate). The 800 nm output pulse was frequency-doubled to produce the 400 nm pump beam. Neutral density filters were used to adjust pump beam power. The pump beam was focused on the sample to a diameter of 300 μm . A white light continuum (WLC) from 380 to 850 nm was generated by attenuating and focusing the 800 nm pulse into a CaF₂ window and split into probe and reference beams. The probe beam was focused with a parabolic reflector onto the sample. The reference and probe beams were focused into a fiber-coupled multichannel spectrometer with complementary

metal-oxide-semiconductor (CMOS) sensor and detected at a frequency of 1 kHz. The delay between the pump and probe pulses was controlled by a motorized delay stage. 1 mm cuvettes were used for all solution sample TA spectroscopy measurements.¹²

2.5.8 Nanosecond Transient Visible Absorbance

Nanosecond TA was performed with the EOS spectrometer (Ultrafast Systems LLC). The pump beam at 400 nm was generated in the same way as femtosecond TA experiments. The WLC used was generated by focusing an Nd:YAG laser into a photonic crystal fiber. The delay time between the pump and probe beam was controlled by a digital delay generator (CNT-90, Pendulum Instruments). The probe and reference beams were detected with the same multichannel spectrometers used in femtosecond TA experiments. Solution phase samples were also contained in 1 mm cuvettes and data was collected under constant stirring to ensure the sample was not damaged. Full details of both the systems used for the nanosecond and ultrafast measurements have been published elsewhere.¹²

2.5.9 Electrochemistry: Cyclic Voltammetry

All electrochemical techniques were performed on a Gamry Instruments Potentiostat, Reference 600. The scan rates are indicated in each voltammogram. Solutions for cyclic voltammetry each contained 10 mM analyte, 10 mM borate buffer and 100 mM KCl salt. The solution was purged under N₂ for 10 min prior to data collection. Cyclic voltammograms of mediators were collected using a glassy carbon working electrode, Ag/AgCl (0.1M) (vs. NHE 0.2881 V)¹³ as reference and Pt wire as counter electrode. Final data and analysis are listed in the appropriate chapters.

2.5.10 Electrochemistry: Chronopotentiometry

For the determination of the extinction coefficients of the radical form of the mediators, an electrochemical technique called chronopotentiometry was adapted from a literature described procedure.¹⁴ This experiment was performed using a Gamry Instruments Potentiostat Reference 600 while monitoring the absorbance spectrum via a fiber optically coupled spectrometer from Ocean Optics by the submersion of a dip probe (Ocean Optics).

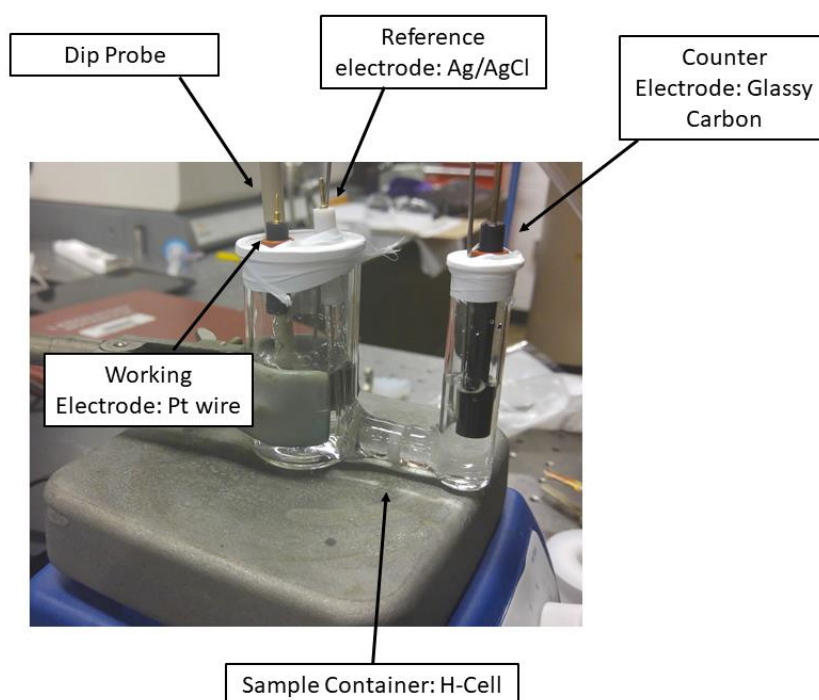


Figure 2.2 Chronopotentiometry setup with experimental components indicated with arrows. The H-cell with electrodes are positioned on a stir plate with **N₂ gas lines** inserted to maintain inert atmosphere.

Briefly, the experiment consisted of generating a 4 mM solution of the mediator, in 50 mM borate buffer, pH 12 and housed in an H-cell (borrowed from the laboratory of Dr. Craig Hill). Into the cathodic compartment were the dip probe and working and reference electrodes.

In the anodic compartment, the carbon counter electrode was located. The solution was stirred constantly and kept inert with a gas line inserted into the headspace of the cell. The equation listed below was used to determine the extinction coefficient of the radical from the slope of the line from data generated. A more detailed discussion of experimental parameters, setup and results are included in chapter 3 of this thesis.

$$\alpha = \frac{(\varepsilon)(I)(l)}{(F)(v)}$$

Equation 2.3 Equation used to determine the extinction coefficient of reduced species generated during the chronopotentiometry experiment. Where, α = slope from plot of absorbance vs. time; ε = extinction coefficient; I = current (A); l = pathlength; F = Faraday's constant; v = volume of solution.

2.5.11 Proton NMR

Samples prepared for proton nuclear magnetic resonance (H NMR) spectroscopy were prepared as 1 mM solutions of analyte in D₂O. NMR spectra were recorded using either a 400 or 500 MHz Bruker spectrometer in the Emory Chemistry Core facilities. NMR spectra of mediators presented in this thesis are included in Chapter 3 of this thesis.

2.5.12 X-ray Quality Crystal Growing Procedure

X-ray quality crystals were grown by vapor diffusion of chloroform into concentrated mediator solutions of water. Diffraction data were collected and analyzed by John Bacsá and Tom Pickel. A table containing representative X-ray data are presented in table 1 in Chapter 3 of this thesis.

2.6 Light Driven Activity Assays and Quantum Yield Calculations

2.6.1 Light-driven Mediator Reduction

Typical mediator reduction experimental conditions are listed here and are similar to those used by others.^{1-2, 8} A typical sample contained CdSe/CdS dot-in-rod (DIR) nanoparticles (0.1-0.2 O.D @ 405 nm), 1-30 mM mediator and 50 or 100 mM MPA the typical sacrificial electron donor (SED) used for these measurements. The total volume for each sample was 1.4 mL in 50mM phosphate and buffered to the appropriate pH (between 6.5 and 10.5) The sample was prepared inside of a glovebox under a 95% N₂ and 5% H₂ atmosphere. Sample components were buffer exchanged or dissolved directly into the buffer to maintain consistent conditions. While still inside of the glovebox, the cuvette was sealed with a rubber septum and Teflon tape. N₂ flow was introduced 10 min prior to the start of the experiment and continuously run in the headspace of the cuvette to maintain an inert atmosphere.

The sample was illuminated with a 405 nm diode purchased from Thor labs and the absorbance monitored with a fiber optically couple ocean optics uv-vis spectrometer. The sample was illuminated in 10 second intervals and allowed to equilibrate with the laser off for 10 sec intervals while stirring continuously, producing the steps observed in Figure 2.3 below. QE is calculated by dividing moles of radical generated by moles of photons absorbed by the sample (see equation 2.4).

$$QE_{rad} = \frac{n_{med}}{\phi_q(1 - 10^{A_{405}})t}$$

Equation 2.4 Equation used to calculate the quantum efficiency of mediator reduction (QE_{rad}).

Where, n_{med} is the number of mediators reduced, ϕ_q is the photon flux of the excitation source

and t is time at which this calculation is being done. $(1 - 10^{A_{405}})$ represents the concentration of the nanomaterial in solution.

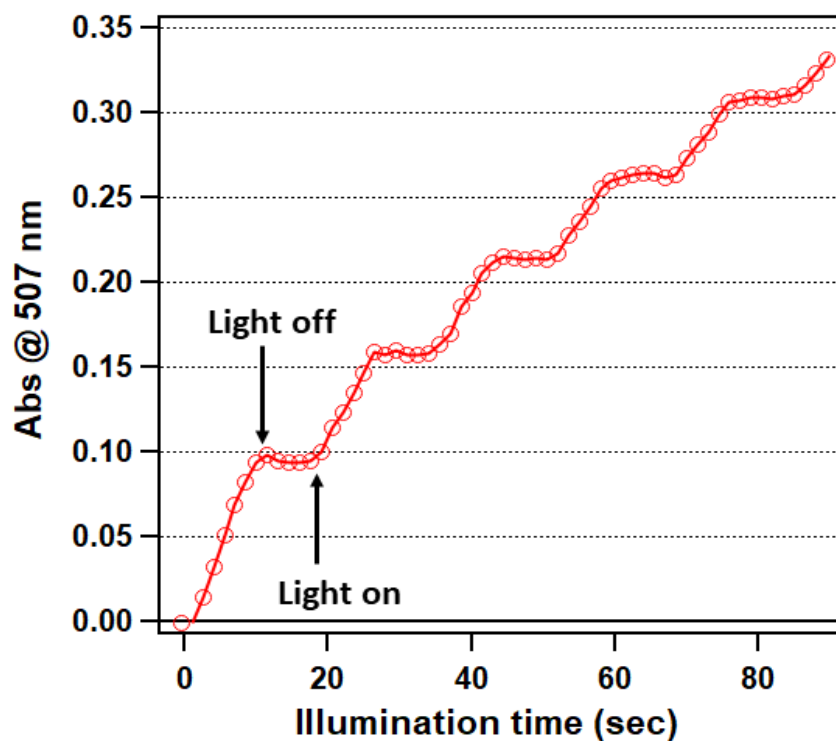


Figure 2.3 Representative QE data for Mediator reduction. Depicted is an example of the kind of data that is collected in a photo-driven mediator reduction experiment

We accounted for the index of refraction by multiplying by 9.15 based on previously reported measurements. For H_2 production assays mediator radical is replaced with 2*moles H_2 produced.

2.6.2 Light-driven H_2 Production

The samples used for light driven hydrogen production are analogous to those used in light-driven mediator reduction. The main exception is the inclusion of the hydrogen producing enzyme, [FeFe] hydrogenase or [NiFe] hydrogenase. The protein was buffer exchanged into the appropriate buffer prior to inclusion in the sample containing rods and mediator. Also, instead of

septa and Teflon tape to seal the cuvette, a homebuilt pressure sensor was incorporated into the cuvette cap for monitoring the generation of H₂ as a change in pressure. Mols of H₂ were calculated using a previously reported equation.¹⁵

2.6.3 H₂ Detection via a Pressure Sensor

Hydrogen production was measured as a change in pressure using a home-built system with sensor components purchased from Phidgets. The change in pressure was measured by with a pressure sensor inserted directly into the cuvette cap and cemented with epoxy (Fig. 2.3). The pressure data was recorded with a LabVIEW program every 1000 ms or 10000 ms according to experimental set up and the change in pressure is converted to moles of H₂ with the ideal gas law.

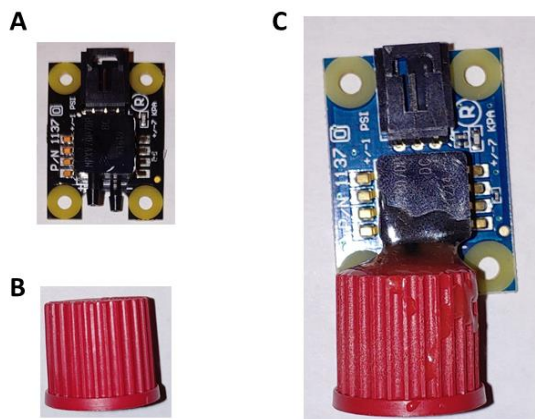


Figure 2.4 Homebuilt pressure sensor components. A) Phidgets pressure transducer, maximum pressure 7 kpa \pm 1 kpa. B) Typical red cuvette cap used to hold pressure sensor. C) Final pressure sensor cap with pressure transducer cemented to the cap with epoxy.

2.7 Data Analysis

For transient measurements such as TRIR and TRVis data collected, typically several individual “transients” or shots were collected then averaged. This final average either needed to be further treated or could be fitted with a sum of exponential function (equation 3 below).

Although the fitting procedure, details and examples are listed in this chapter all analysis and final fit coefficients achieved from this process are discussed in the relevant chapters.

$$f(x) = y_0 + \sum_{k=0}^{n-1} (A[k] * e^{(-1/\tau * x[k])})$$

Equation 2.5 Sum of exponential fit function used to fit transient data. Where $A[k]$ = amplitude and τ = rate.

2.7.1 Fitting Infrared Transient Absorbance Data

Data were imported into Igor via a home-written loader program. After averaging, discarding noisy data and subtracting the heating signal in the IR, the transients were fit to a multi-exponential function. In some cases, the time constants derived were then used to calculate an amplitude weighted lifetime (AWL). The data averaging and subtracting procedure is depicted in Figure 2.5. The number of components varied depending on the measurement. The optimum number of exponentials was determined by minimizing the χ^2 value and comparison of residuals.

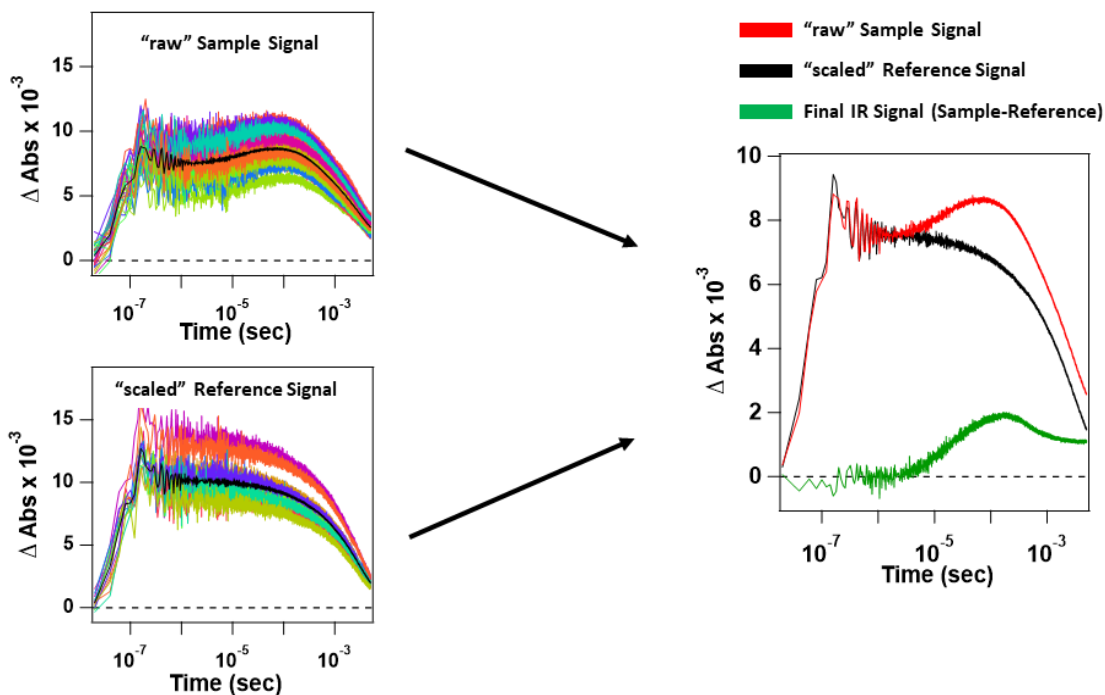


Figure 2.5 Data analysis procedure for IR data. Top left panel shows representative raw reference signals that are averaged to yield the black trace, ($S_{\text{am,avg}}$). Below, in the bottom left panel, representative raw sample signals probing at 1934 cm^{-1} are shown as multi-color traces. These have been averaged to yield the black trace similar to the reference traces ($S_{\text{am,avg}}$). The final panel to the right depicts the subtraction process between the sample and reference averages to yield the “final IR signal” that is used for kinetics analysis.

2.7.2 Fitting Transient Absorbance Visible Data

Data were imported into Igor via a home written loader program. After averaging individual transient traces and discarding noisy data, the transient absorbance (TA) data were fit

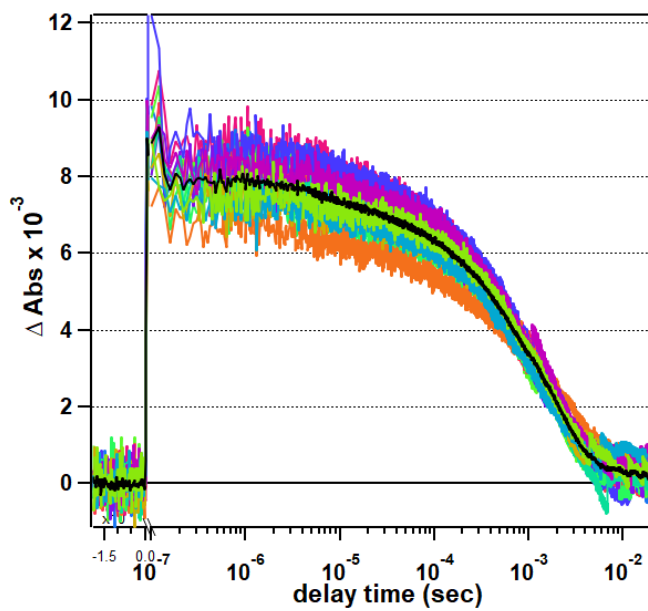


Figure 2.6 Data analysis procedure for TRVis data. The multicolored traces represent individual “shots” collected and the black trace is the average of these shots that is used for analysis.

to a sum of exponential functions. The number of components varied depending on the measurement. The optimum number of exponentials was determined by minimizing the χ^2 value and comparison of residuals. The data averaging and subtracting procedure is depicted in Figure 2.8.

2.7.3 Global Fitting FTIR and Absorbance Spectra

FTIR and UV-Vis absorbance data were fit using a global fitting procedure package in IGOR with a gaussian function to determine peak locations and deconvolve overlapping populations.

2.8 References

1. Chica, B.; Wu, C.-H.; Liu, Y.; Adams, M. W. W.; Lian, T.; Dyer, R. B., Balancing electron transfer rate and driving force for efficient photocatalytic hydrogen production in CdSe/CdS nanorod–[NiFe] hydrogenase assemblies. *Energy & Environmental Science* **2017**, *10* (10), 2245-2255.
2. Zhu, H.; Song, N.; Lv, H.; Hill, C. L.; Lian, T., Near Unity Quantum Yield of Light-Driven Redox Mediator Reduction and Efficient H₂ Generation Using Colloidal Nanorod Heterostructures. *Journal of the American Chemical Society* **2012**, *134* (28), 11701-11708.
3. Talapin, D. V.; Koeppel, R.; Götzinger, S.; Kornowski, A.; Lupton, J. M.; Rogach, A. L.; Benson, O.; Feldmann, J.; Weller, H., Highly Emissive Colloidal CdSe/CdS Heterostructures of Mixed Dimensionality. *Nano Letters* **2003**, *3* (12), 1677-1681.
4. Kunneman, L. T.; Zanella, M.; Manna, L.; Siebbeles, L. D. A.; Schins, J. M., Mobility and Spatial Distribution of Photoexcited Electrons in CdSe/CdS Nanorods. *The Journal of Physical Chemistry C* **2013**, *117* (6), 3146-3151.
5. Manna, L.; Scher, E. C.; Alivisatos, A. P., Synthesis of Soluble and Processable Rod-, Arrow-, Teardrop-, and Tetrapod-Shaped CdSe Nanocrystals. *Journal of the American Chemical Society* **2000**, *122* (51), 12700-12706.
6. Homer, R. F.; Tomlinson, T. E., 504. The stereochemistry of the bridged quaternary salts of 2,2'-bipyridyl. *Journal of the Chemical Society (Resumed)* **1960**, (0), 2498-2503.
7. Brienne, S. H. R.; Boyd, P. D. W.; Schwerdtfeger, P.; Bowmaker, G. A.; Cooney, R. P., Infrared spectra and theoretical studies of bridged diquaternary 2,2'-dipyridinium compounds. *Journal of Molecular Structure* **1995**, *356* (2), 81-94.

8. Sanchez, M. L. K.; Wu, C.-H.; Adams, M. W. W.; Dyer, R. B., Optimizing electron transfer from CdSe QDs to hydrogenase for photocatalytic H₂ production. *Chemical Communications* **2019**.
9. Jiang, Z.-J.; Kelley, D. F., Hot and Relaxed Electron Transfer from the CdSe Core and Core/Shell Nanorods. *The Journal of Physical Chemistry C* **2011**, *115* (11), 4594-4602.
10. Greene, B. L.; Vansuch, G. E.; Chica, B. C.; Adams, M. W. W.; Dyer, R. B., Applications of Photogating and Time Resolved Spectroscopy to Mechanistic Studies of Hydrogenases. *Accounts of Chemical Research* **2017**, *50* (11), 2718-2726.
11. Greene, B. L.; Wu, C.-H.; McTernan, P. M.; Adams, M. W. W.; Dyer, R. B., Proton-Coupled Electron Transfer Dynamics in the Catalytic Mechanism of a [NiFe]-Hydrogenase. *Journal of the American Chemical Society* **2015**, *137* (13), 4558-4566.
12. Li, Q.; Lian, T., Ultrafast Charge Separation in Two-Dimensional CsPbBr₃ Perovskite Nanoplatelets. *The Journal of Physical Chemistry Letters* **2019**, *10* (3), 566-573.
13. Meites, L., *Handbook of Analytical Chemistry*. McGraw-Hill: New York, 1963; p 1788.
14. Pedersen, S. U.; Bo Christensen, T.; Thomasen, T.; Daasbjerg, K., New methods for the accurate determination of extinction and diffusion coefficients of aromatic and heteroaromatic radical anions in N,N-dimethylformamide. *J. Electroanal. Chem.* **1998**, *454* (1), 123-143.
15. Greene, B. L.; Joseph, C. A.; Maroney, M. J.; Dyer, R. B., Direct Evidence of Active-Site Reduction and Photodriven Catalysis in Sensitized Hydrogenase Assemblies. *Journal of the American Chemical Society* **2012**, *134* (27), 11108-11111.

Chapter 3

Optimizing Electron Transfer from CdSe QDs to Hydrogenase for Photocatalytic H₂ Production

Aspects have been reproduced from Ref. 8 with permission from the Royal Society of Chemistry

3.1 Abstract: With the ability to convert solar energy into a storable fuel source, systems composed of a photosensitizing nanomaterial, redox mediator, and catalyst have the potential to provide a new source of clean energy. The inclusion of a redox mediator to act as electron shuttle between photosensitizing material and catalyst is not novel, but this approach has been under-utilized due to a lack of characterization of potential small molecules as electron shuttles. We addressed this gap in knowledge by employing a class of molecules with unique structural modifications on the classic mediator, methyl viologen. This series of viologen related molecules, also of varying reduction potential (-450 mV to -670 mV vs. SHE), has been characterized and their utility as electron shuttles between CdSe quantum dots and H₂ase enzyme demonstrated. These molecules have a bipyridine core but feature methyl group substituents and a carbon chain of varying length linking the nitrogens of the molecule. The chain induces a twist in the ring system, while the methyl groups increase the electronic bulk of the aromatic system to varying degrees depending on the position they occupy. Cumulatively, these changes lead to interesting structural and electronic properties in these mediators. We found that tuning the mediator LUMO energy optimizes the performance of this hybrid photocatalytic system by balancing electron transfer rates of the shuttle in steady-state hydrogen production measurements. This sensitivity to mediator LUMO energy was also observed in ultrafast transient absorbance measurements but could not be explained exclusively by this. By manipulating the redox mediator to bias electron transfer to the catalyst through convenient surface interactions with the nanomaterial and a lowered redox potential, we have shown the potential of this simple modification to vastly improve the efficiency of this system. Thus, from both steady-state and transient measurements, a dependence on mediator structural and electronic features has been demonstrated.

3.2 Introduction

Artificial photosynthetic systems usually employ separate modules to accomplish the essential functions of efficient light harvesting, charge separation and catalytic proton coupled electron transfer (PCET) reactions to generate high energy chemical bonds.¹⁻³ This approach mimics the natural photosynthetic systems and allows independent optimization of each module for its specific task. Hybrid nanomaterial/enzyme photocatalysts are promising examples of this modular approach.³⁻⁵ The nano-crystalline semiconductor (NCS) material acts as both the light harvesting and charge separation module. It can be designed to generate long-lived reductive or oxidative equivalents with high quantum efficiency and regenerated by the addition of a sacrificial electron donor to act as the terminal hole acceptor. Enzymes that catalyze PCET reactions operate with little overpotential at rates that match or exceed the rate of generation of redox equivalents by the solar flux.⁶ Thermophilic enzymes have high stability and durability, yielding high turnover numbers (TONs).⁷ These modules have been highly optimized; however, the difficult challenge that remains is how to transfer reactive electrons between the modules. Both natural and artificial systems have employed redox mediators, small molecule electron carriers capable of moving between modules and efficient redox cycling. The challenges with this approach include generating a sufficient driving force for multiple electron transfer (ET) steps and efficient interfacial ET while avoiding back ET.⁸ Methyl viologen (MV) and closely related molecules have been widely employed as electron relays largely because of their stable, long-lived radicals, commercial availability and solubility in water.⁹⁻¹² Most studies aimed at optimizing ET to and from a mediator have focused on manipulating the light harvesting/charge separation material.⁹⁻¹⁰ Not much attention has been paid to tuning the mediator structure and redox potential for improving ET efficiency.^{8, 13-14} Here, we have investigated the effects of a

mediator structure and reduction potential on the overall efficiency of a hybrid CdSe quantum-dot/mediator/[NiFe]-hydrogenase photocatalytic system. We varied the structure of viologen-like mediators by introducing the methyl group substituents and a carbon chain linking the two pyridyl nitrogens, as shown in Fig. 1. These modifications expand the range of reduction potentials of the mediators. We characterized this series of mediators structurally, spectroscopically and electrochemically and determined the effects of these mediator properties on the photocatalytic production of hydrogen in the hybrid QD/hydrogenase system.

3.3 Results and Discussion

3.3.1 Characterization of Mediator Structure and Electronic Properties by UV-Vis, H NMR, X-ray Crystallography, and Cyclic Voltammetry

While several studies on the effect of the electronic properties of the redox mediator as electron shuttle have been published, few studies have been focused on the structural aspect of the mediator. Two key studies inspiring this work were published by Weiss et al. in which it was determined that the primary mechanism by which the redox mediator accepted an excited state electron from the photosensitizer was via tunneling directly between donor and acceptor orbitals. This mechanism was determined to be facilitated by the positioning of the mediator on the surface of the material. If there was not sufficient overlap between the orbitals of the mediator and the material, ET was less likely to occur. Thus, the efficiency of ET had the potential to be influenced by the structural characteristics of the mediator as well as the electronic properties and so ET could be enhanced or inhibited depending on the degree of these changes.^{10-11, 13}

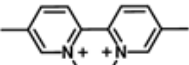
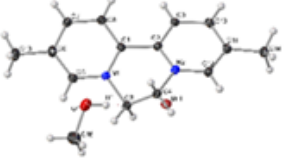
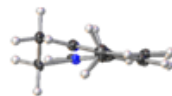
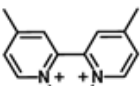
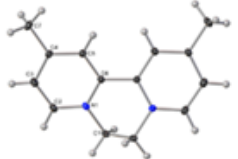

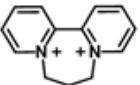
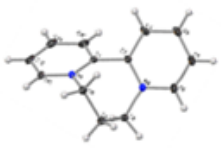
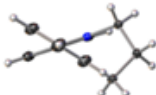
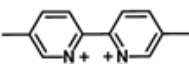
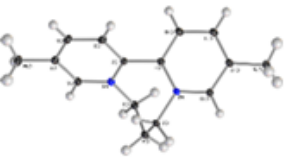
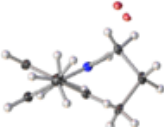
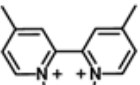
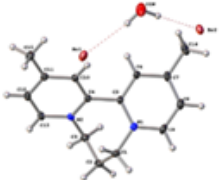
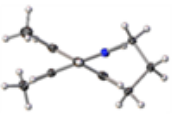
	Front View	Side view	Torsional Twist
 DQ52 -470 mV			18°
 DQ42 -490 mV			20.8°
 DQ3 -550 mV			52.5°
 DQ53 -635 mV			55.5°
 DQ43 -670 mV			52.3°

Table 3.1 Table summarizing structural information and reduction potentials (vs. NHE) for the mediators used in this study obtained by X-ray crystallography and cyclic voltammetry. The numbering scheme refers to the position of the methyl substituents (4 or 5) and the length of the carbon chain (2 or 3). Column 1 lists the reduction potential as well as identifies the mediator in the row. Columns 2 and 3 shows the X-ray structures for each mediator in a “front view” and as a “side-on” the mediator. Column 4 lists the torsional twist for each mediator. All experimental procedures can be found in the Analytical chapter of this thesis.

We know the position of the bipyridyl methyl substituent has the potential to affect the electronic structure of the mediator while minimally affecting the sterics of its interaction with a nanocrystalline semiconductor surface. So, we began this study by detailing the specific structural characteristics of these mediators both in the solid and liquid state. As had been demonstrated previously,¹⁵⁻¹⁷ the carbon chain linking the two pyridyl nitrogens introduces a twist in the torsion angle of the two rings that depends on the chain length. Evidence of the twist along the bipyridine core is clear from the X-ray structures (Table 3.1). The NMR spectra of the mediators also support the presence of this twist in the core due to the coupling of the shifted peaks that is observed. A planar structure would not exhibit such coupling between protons which should be experiencing identical environments. These data together are consistent with previous reports based on similar techniques.¹⁶ Representative X-ray structures of the mediators are presented in Table. 3.1. The average torsional twist between the pyridyl ring was ~19 degrees for those mediators with a two-carbon chain linker and ~53 degrees for those with a three-carbon chain linker. The torsional twist also causes important changes in the electronics structure of the mediators. These changes are reflected in the reduction potential, which becomes more negative as the torsional twist increases. Previous molecular orbital (MO) calculations for mediators with 2C and 3C linkers showed that increasing the torsional twist disrupts the conjugated system and shifts the LUMO to a higher energy.¹⁶ The position of the methyl groups also play a role in the change in reduction potential observed. When in the gamma position (as is the case for DQ42 and DQ43) the electron density donation of the methyl groups is felt more strongly as opposed to the beta position (DQ52 and DQ53) leading to slightly more negative reduction potentials as observed by cyclic voltammetry.

The effect on the mediator electronic structure is also reflected in the UV-vis absorbance spectra of the di-cation forms (Fig. 3.1). The $\pi \rightarrow \pi^*$ transition of the di-cation is observed to shift to higher energy with an increasing torsional twist.¹⁸ The blue shift is related to the change in ΔE between the HOMO and LUMO with the twist angle. The MO calculations indicate that the ΔE increases due to the increase in the LUMO energy, consistent with our observation of more negative reduction potentials in the cyclic voltammetry data (Fig. 3.5.2 of the appendix).¹⁶ In contrast, the $\pi \rightarrow \pi^*$ transition of the reduced mediators is observed to shift to lower energy with an increasing linker length (Fig. 3.2). This red-shift has been attributed to previously to a more planar structure for the radical species.^{16, 18} The decrease in the torsional twist associated with the radical cation formation allows a greater degree of orbital overlap between the bipyridinium rings, leading to the lower energy transition. Slower ET rates are observed as the twist angle is increased, due to an increase in the reorganization energy required to reach the

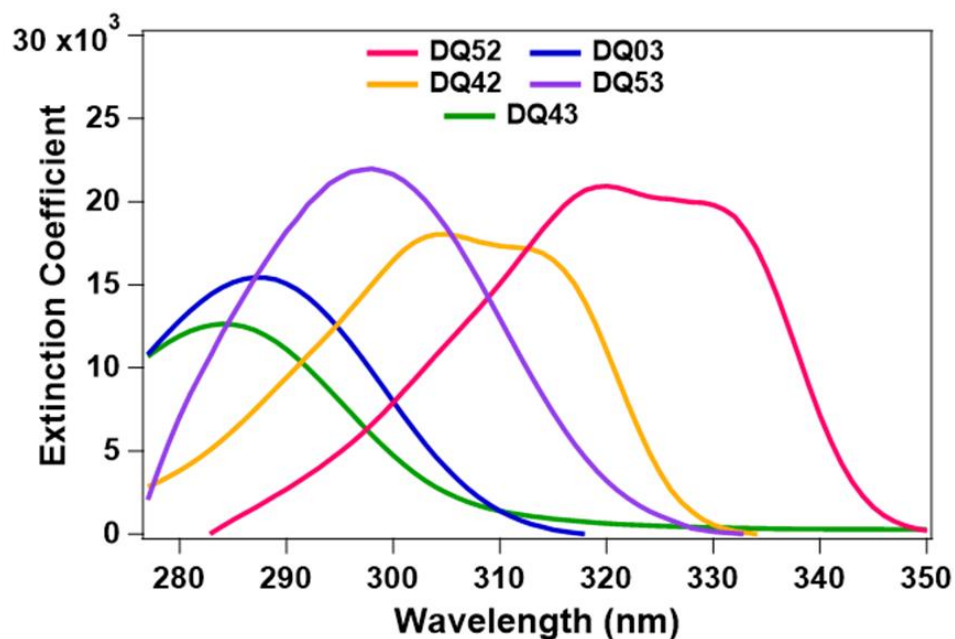


Figure 3.1 UV-Vis molar extinction spectra of oxidized mediators. Color scheme is as follows: pink = DQ52; yellow = DQ42; blue = DQ03²⁺; purple = DQ53²⁺; green = DQ43²⁺

planar structure of the reduced state.¹⁸ Electronic structure calculations of DQ03 also support a change in the geometry of the mediator from the twisted form to a more planar configuration upon reduction.¹⁶

3.3.2 Determining the Extinction Coefficient for One-electron Reduced Mediators via Chronopotentiometry

Before the efficiency of these mediators to act as electron acceptors and carriers for the photosensitizer system could be assessed, a method to quantify the concentration of reduced mediator was needed. Typically, the absorbance spectrum can be used for this purpose by solving for the concentration using Beer's Law ($A = \epsilon * c * l$). To do this though, the extinction coefficient of the analyte must be known. For this reason, at the outset of this study, we found it necessary to experimentally determine the extinction coefficient of the one-electron-reduced mediator ourselves because reliable data of the molar absorptivity of the mediators was not available. To determine the extinction coefficients needed, we employed a method that had been used previously to find the molar absorptivity for one electron reduced molecules¹⁹. This approach involves electrochemically reducing the mediators while simultaneously monitoring the absorbance spectrum. From which, absorbance at a specified wavelength vs. time can be plotted and used to solve for the extinction coefficient. An example of this is pictured in Figure 3.2A, with the DQ03 mediator. The slope for each period of reduction (or increased absorbance) could then be used to calculate the extinction coefficient using the equation 2.3 described in Chapter 2.

The approach was first tested and optimized with methyl viologen which, due to its ubiquity as a redox mediator, has a well-established and accepted extinction coefficient for its one-electron reduced state.²⁰⁻²² Once the parameters which could reproduce the expected slope, which yielded the reported extinction coefficient for methyl viologen was established, this method was applied to the mediators described in this chapter. Though these mediators have three spectral features which absorb in the visible for the one electron reduced state which could potentially be used to monitor for determining the extinction coefficient, the feature which appeared between 450 and 515 nm was concluded to produce the most reliable measurements and so was chosen for this experiment. The feature which appears in the near UV, typically around 400 nm, has an extremely high extinction coefficient (>10000), and so reached absorbances greater than 1 before the completion of the study resulting in large standard deviations. The other absorbance feature, which generally appeared in the near IR had the converse problem. The extinction coefficient for this feature is quite low and so it was difficult

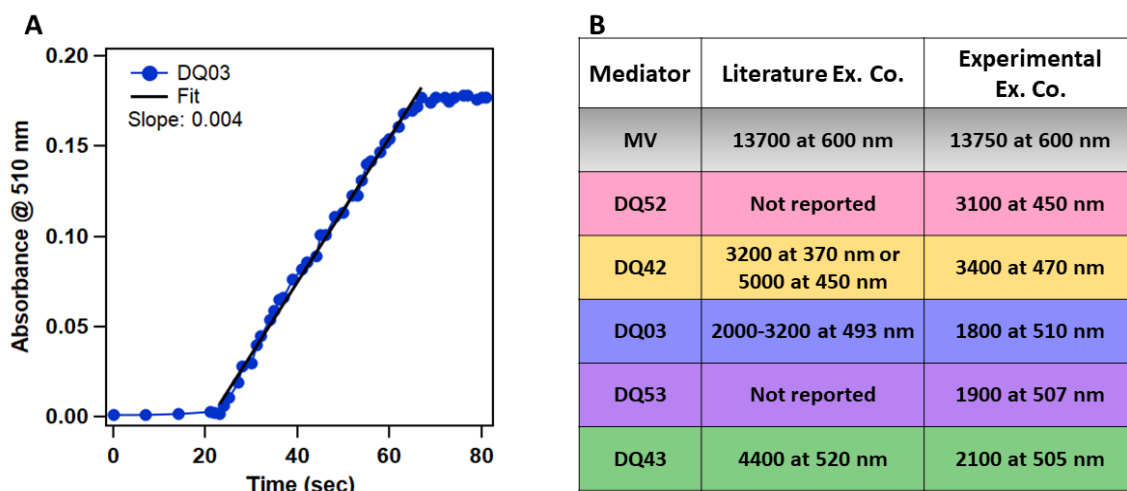


Figure 3.2 Summary of chronopotentiometry results. A) Example of chronopotentiometry data acquired for DQ03. B) A table summarizing the experimentally determined extinction coefficients compared to their literature expected extinction coefficients where available.

to generate radical populations large enough to achieve a signal-to-noise ratio sufficient for reliable measurements. Thus, the feature monitored for this study (appearing between 450 and 515 nm) absorbed strongly enough to yield measurements with a clean signal-to-noise ratio but not so strongly that it deviated from the linearity of the measurement minimizing the error of the measurement. The results from this study are summarized in Figure 3.2B above, where the reported literature extinction coefficients are also listed for comparison when available.

3.3.3 Quantum Efficiency of Photo-driven Mediator Reduction with CdSe Quantum Dots

The first step in the electron shuttle process for photo-driven catalysis is ET from the conduction band (CB) of the excited CdSe QD to the mediator. We performed steady-state photo-illumination experiments to determine the quantum efficiency for reduction of the mediator (QE_{rad}) as shown in Fig. 3.3. Illumination of the CdSe QD with blue light (405 nm) produces an exciton state, which the mediator quenches by extracting an electron from the CB, generating a population of the reduced mediator radical cation (mediator^{*+}). The hole left in the VB of the CdSe QD is scavenged by the sacrificial electron donor (SED), mercaptopropionic acid (MPA). This ET event (k_{CS}) is depicted schematically in Fig. 3.4 along with the relative LUMO energies of the mediators. The absorbance spectra of the radical cations are shown in Fig.3.4A. The absorbance at either 450 nm or 510 nm was monitored for each mediator depending on whether the spectrum belonged to a 2C or 3C linked molecule, respectively.

The concentration of the reduced mediator *versus* the illumination time (Fig.3.4) is determined from the measured extinction coefficient of each radical species (Fig 3.2). QE_{rad} was determined by dividing the moles of radicals generated by the moles of photons absorbed by the solution and correcting for reflection from the front face of the cuvette. We calculated quantum yield from the first 10 seconds of illumination, before the concentration of mediator^{*+} builds up, thus minimizing contributions from back ET (k_{CR}) and other parasitic processes that lead to mediator degradation.⁷ The rate of formation of mediator^{*+} is constant for the first 10 seconds but begins to decline after this initial phase (Fig. 3.4). The decrease in the rate of formation of mediator^{*+} is attributed to the consumption of the mediator di-cation and to an increased rate of charge recombination at high concentrations of the mediator^{*+}. At longer time periods, the rate of mediator reduction and charge recombination are balanced, and the system reaches a steady

state. The initial rates of mediator^{•+} formation and steady state concentrations vary with the reduction potential of the mediator (Fig. 3.4B), with the 2C linker mediators having significantly faster initial rates and reaching larger steady state populations than the 3C linker ones. It is clear that the 2C linker molecules, DQ42 and DQ52, have the highest net QE_{rad} are best explained by considering the fastest k_{CS} and the slower k_{CR} observed for the 2C linked mediators relative to the 3C linked ones. The result of the faster k_{CS} and the slower k_{CR} is a net higher QE_{rad} and therefore larger steady-state populations of the reduced mediator, as strongly suggested by the steady-state

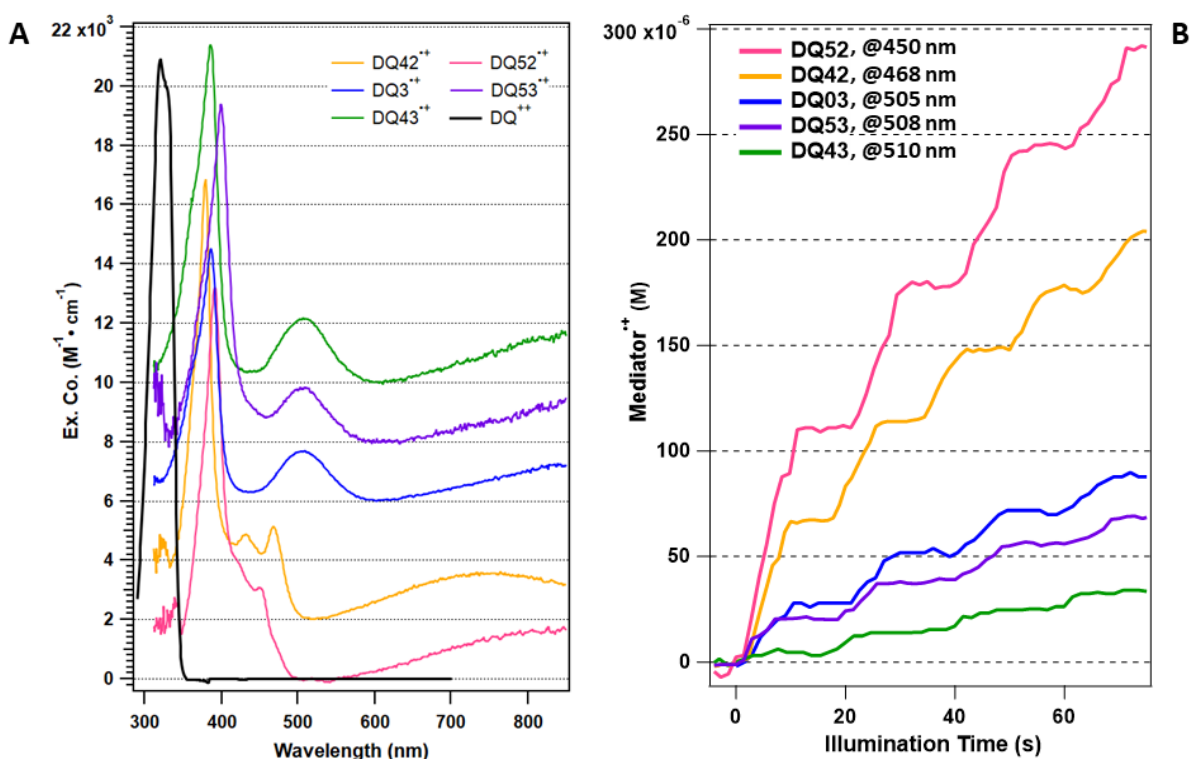


Figure 3.3 Radical UV-Vis spectra and representative plots of radical concentration vs time from photo-driven QE_{rad} measurements. A) UV-vis molar extinction spectra for reduced mediators (spectra have been offset for clarity.) B) Representative plots of radical concentration vs illumination time from photo-driven mediator reduction experiments. Both plots A and B follow color scheme: pink = DQ52^{•+}; yellow = DQ42^{•+}; blue = DQ03^{•+}; purple = DQ53^{•+}; green = DQ43^{•+}

data. The differences in the ET rates and net QE_{rad} for this series of mediators can be understood in terms of the reduction potentials, which influence both the forward and reverse ET reactions.²³ Fig. 3.4B shows the dependence of the net QE_{rad} on the reduction potential of the mediator. The energetics of this process is illustrated in Fig 3.4C, where the relative energy levels were determined from the reduction potentials of the mediators and the band edge of the CdSe QDs. The 2C linker mediators with more positive redox potentials (lower energy LUMOs) have a larger downhill driving force for forward ET and a smaller driving force for back ET, resulting in the larger k_{CS} and the smaller k_{CR} (normal Marcus regime). The net result is a long-lived charge separated state and a high QE_{rad} . The situation is more complex for the 3C linker mediators, since their more negative reduction potential yields a driving force for back ET in the Marcus inverted regime, resulting in a decrease in k_{CR} .

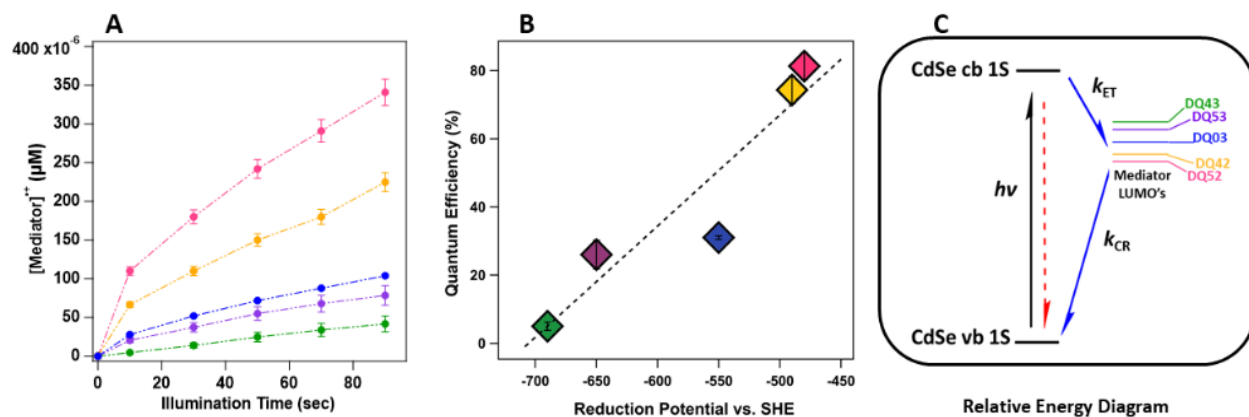


Figure 3.4 Steady-state experiments with CdSe QDs and mediators. (A) Kinetics of photo-reduction of the mediator, quantified by monitoring the absorbance at 450 or 510 nm for 2C or 3C linked radical species, respectively. (B) Dependence of quantum efficiency for reduction of mediators on reduction potential. (C) Schematic illustration of the ET processes and energies of the CdSe QD conduction band (CB) and the valence band (VB) relative to the mediator LUMO energies.

It is also likely that the rate of ET from the QD to the mediator and the net QE_{rad} are affected by the differences in the reorganization energy for forward and reverse ET across this series. The reorganization energy is influenced by the torsional twist between the pyridyl rings of the mediators, since the reduced mediator adopts a more planar structure.¹⁶ Thus, the reorganization energy for the more highly twisted 3C linker molecules is expected to be larger than that for the 2C linker molecules. This increased reorganization energy is expected to slow down the ET to the 3C linker molecules relative to the 2C linker ones, leading to less efficient charge separation. For example, the net QE_{rad} drops dramatically from 74% to 31% between DQ42 and DQ03 as the twist in the bipyridyl core is increased from ~22 degree to ~55degree. A further study would be required to assess the relative contributions of the reorganization energy and the driving force to the difference in the net QE_{rad} , but both are likely important.

3.3.4 Quantum Efficiency of Photo-driven Hydrogen Production

The next step in the electron shuttle process is ET from the mediator⁺⁺ to the hydrogenase and the turnover of the enzyme to produce hydrogen (QE_{hyd}). We measured the hydrogen production efficiency for a hybrid system consisting of CdSe QDs, mediator and the [NiFe] SHI from *Pyrococcus furiosus* (*Pf*) as the hydrogen production catalyst. *Pf* SHI is a robust catalyst, having high thermal stability and oxygen tolerance.²⁴ It also has a high turnover rate at neutral pH (100 s^{-1} at room temperature) and operates close to the thermodynamic potential of the hydrogen couple. Hydrogen production assays were carried at pH 7.1 under conditions analogous to those used in the mediator photoreduction experiments. Fig.3.6A shows the time-dependent yields of light driven hydrogen production for each of the mediators. Furthermore, addition of a mediator to this hybrid system significantly improves the overall quantum yield for hydrogen production compared to related systems that rely on direct ET from the NCS material

to the hydrogenase. The net production of H₂ and the corrected QE_{hyd} for each mediator are summarized in Table 3.2.

Trends in the QE_{hyd} indicate a strong correlation between the reduction potential of the mediator and the amount of H₂ produced as shown in Fig. 3.6B. Previously, we investigated the effect of the mediator reduction potential on the efficiency of a related hybrid CdSe/CdS nanorod-hydrogenase photocatalytic system.⁷ We compared two mediators, methyl viologen (MV²⁺, $E_{0'} = -446$ mV vs. NHE) and DQ03 and found a significantly better performance with DQ03, due to its greater driving force for ET to the surface exposed FeS cluster of SHI. With DQ03 and nanorods, we achieved the highest reported quantum yield for hydrogen production with such hybrid photocatalytic systems.⁷ The current results are consistent with the previous ones, showing a greater overall efficiency of hydrogen production with an increased driving force for electron transfer from the reduced mediator to the enzyme. The highest observed QE for H₂ production is modest (QE_{hyd} = 16.8%) compared to previous results with nanorods (QE_{hyd} = 52% for similar conditions). This difference in efficiency is primarily due to the NCS photosensitizer, since the nanorod structure has a significantly longer exciton lifetime than the QD, leading to a greater efficiency of the charge separation process. Nevertheless, the yields for the three highest performing mediators in the present work are significantly higher than what has been previously with CdSe QDs.²⁵

The correlation of photocatalytic hydrogen production efficiency with reduction potential of the mediator is inverse to the trend observed for the steady-state mediator photoreduction experiments. This observation highlights the complex interplay between the net yield of hydrogen production and the rates of charge separation, charge recombination and ET to the enzyme, as shown in the scheme in Fig.3.6, panel D. Optimum hydrogen production requires a

balance between the driving force for the two forward ET processes; decreasing the mediator LUMO energy decreases the driving force for the ET to the catalyst (k_{ET}), but at the same time increases the driving force for reduction of the mediator (k_{CS}). Thus, while the mediators that are easier to reduce (lower LUMO energies) exhibit a less effective in reducing the enzyme and producing hydrogen. In contrast, charge recombination becomes more rapid as the LUMO energy is increased, which lowers the net yield of photoreduction in the absence of enzyme. In the presence of enzyme, however, ET to the enzyme is competitive with charge recombination and thus efficient hydrogen production can be achieved.

Further insight into the optimum parameters for hydrogen production is provided by considering the solution potential achieved under illumination at a steady state. Fig.3.6C shows the production of the reduced mediator as a function of the illumination time for DQ03, DQ43, and DQ53 mediators with and without hydrogenase. The reduced mediator concentration increases initially, and then reaches a constant value; a lower steady state population is reached in the presence of hydrogenase, due to the ET to the enzyme. In all cases the system reaches the steady state (constant mediator^{•+} concentration) within an hour. Therefore, we determined the steady state solution potential by measuring the concentration of the reduced mediator from the radical absorbance after 5000 s of illumination. The Nernst equation was then used to calculate the solution potential from the relative concentration of the mediator^{•+}/ mediator⁺⁺, yielding values shown in Table 3.2. For comparison, at pH 7.1 the hydrogen couple is at -419 mV. The most efficient mediators DQ03, DQ53 and DQ43 reach steady state solution potentials close to or more negative than the hydrogen couple. In contrast, with DQ42 and DQ52 the steady state solution potentials are significantly more positive than the hydrogen couple and therefore proton reduction is not favorable for the 2C linker mediators.

The hydrogen production efficiency peaks with DQ53 even though it does not have the most negative reduction potential. DQ53^{•+} concentration levels close to those observed for the DQ03^{•+} are achieved when the solution contains solely dots and mediator (Fig.3.6C). When the enzyme is present, however, steady state illumination produces a barely observable population of DQ53^{•+}, indicating that its consumption by the enzyme is rapid. Based on this evidence, it is

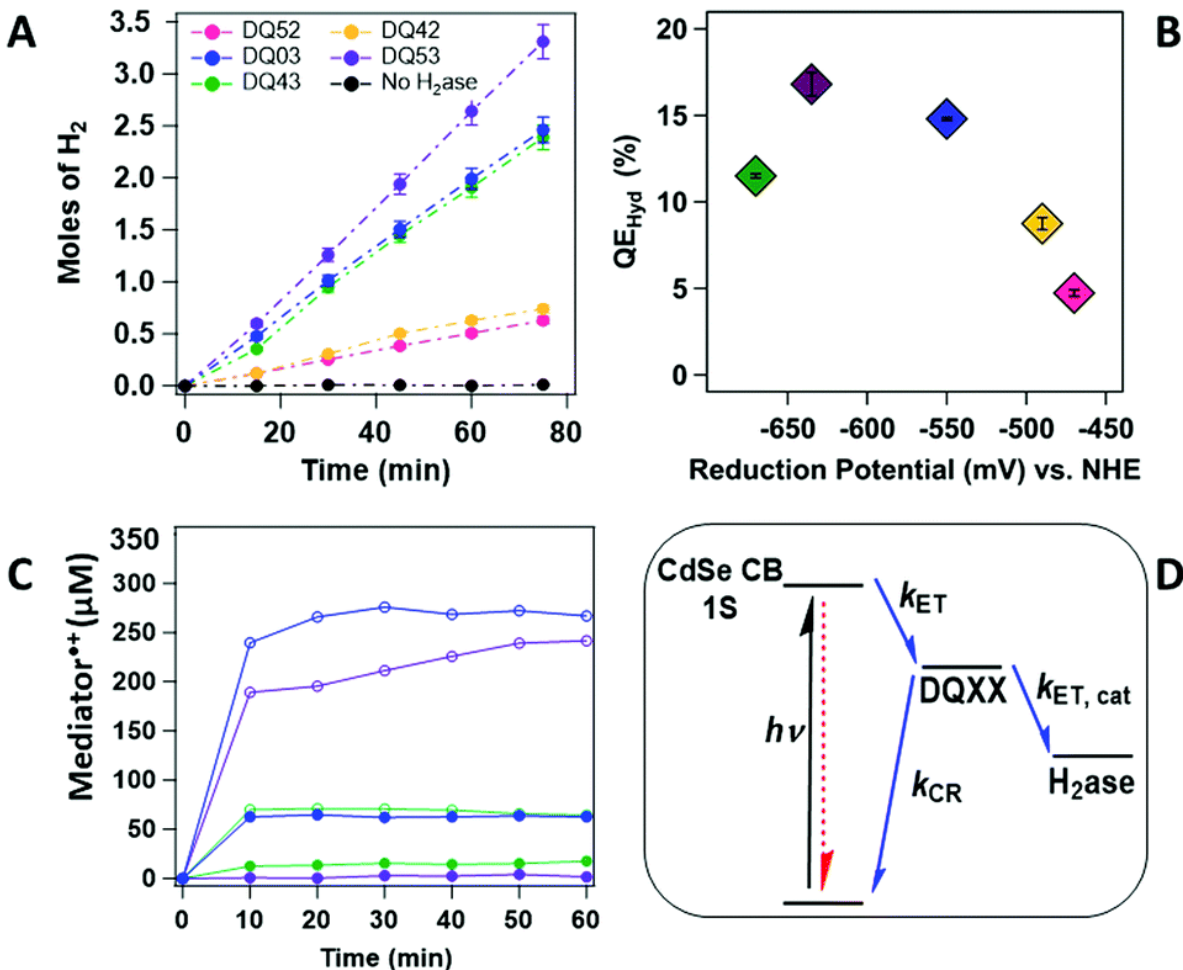


Figure 3.5 Steady-state H₂ production. (A) H₂ production as a function of the laser illumination time: DQ53 (purple), DQ43 (green), DQ03 (blue), DQ42 (yellow), DQ52 (pink), and with no mediator (black). (B) Correlation of H₂ generation efficiency (QE_{Hyd}) with reduction potential. (C) Production of the reduced mediator versus the illumination time with H₂ase (closed circles) and without H₂ase (open circles). (D) Relative energy diagram of ET steps between QD conduction band, mediator LUMO and hydrogenase.

likely that the conditions are not fully optimized for hydrogen production in the case of DQ53. Utilization of a photosensitizer with a longer-lived exciton, such as a nanorod, would increase the QE_{hyd} produced with DQ53, since it would increase QE_{rad} . The lower QE_{hyd} observed with DQ43 is in part due to the inefficient ET to the enzyme despite its more negative reduction potential, resulting in a higher steady state population of the mediator^{•+} compared to DQ53 (Fig. 3.6C). A slower ET to the enzyme for DQ43 might be an indication of entrance into the Marcus inverted regime, wherein having an increased driving force slows the ET to the enzyme, resulting in a lower than expected QE_{hyd} .

<i>Steady-state Hydrogen Production at 5000 sec</i>			
	Solution Potential (mV)	Mols of H ₂	QE_{corr} (%)
DQ52	-375	$4.09 \cdot 10^{-7}$	4.73
DQ42	-385	$8.13 \cdot 10^{-7}$	7.85
DQ03	-410	$2.70 \cdot 10^{-6}$	14.8
DQ53	-425	$3.70 \cdot 10^{-6}$	16.78
DQ43	-495	$2.65 \cdot 10^{-6}$	11.5

Table 3.2 Summary of solution potential from reduced mediator population, photo-driven hydrogen production results and quantum efficiency. Solution potential is reported vs. SHE;

determined from the Nernst Equation: $\Delta E = \Delta E^\circ - \frac{RT}{F} \ln \frac{[\text{Med}^{+}]}{[\text{Med}^{2+}]}$.

3.3.5 Spectral Characteristics of Mediator Radical Decomposition Product

Previously, it has been observed, that over time a decomposition product will form in solution when a sufficient concentration of radical is generated.⁷ To explore this, we performed a series of steady-state experiments to identify the spectral characteristics of such a product and to identify any patterns in formation by comparing this formation between multiple mediators.

By illuminating a sample containing DIR and mediator only, with the same illumination source as before, we monitored for the formation of both the expected radical species and any spectral characteristics that could be assigned to the decomposition product described previously. The sample was illuminated for 3 hours to encourage the formation of this decomposition product. To aid in the identification of these features, difference spectra were generated for the three mediators examined (DQ03, DQ53 and DQ43) by subtracting an initial spectrum (when only radical related absorbances were observable) from an absorbance spectrum taken near the end of the experiment. The results of this analysis are pictured in Fig. 3.7A. In the spectra indicated, DQ03 (blue) shows a large positive absorbance feature at 410 nm and two negative absorbance features at 508 nm and 800 nm. The two negative absorption features are clearly consistent with peaks associated with the expected radical product. The positive feature at around 410 nm is consistent with previously reported results⁷ and cannot be attributed to any other species present in solution so must be related to the expected decomposition product. Similar features were also observed when the same analysis was performed with spectra for the DQ43 mediator. Two negative features associated with the DQ43 radical form (at 510 nm and 800 nm) and a strong positive feature around 410 nm. These results indicate that not only do both DQ03 and DQ43 form a decomposition product similar to one another, but at the time of this subtraction, the population of radical that was generated in the “initial” spectrum has

decreased substantially to result in the negative features observed in the difference spectra. Interestingly, the difference spectra generated for the same experiment with DQ53 yielded none of these observed results. No positive feature around 410 nm is observed, nor are there any negative features associated with a reduced DQ53 observed. This observation indicates that the concentration of radical generated remains consistent through the duration of the experiment.

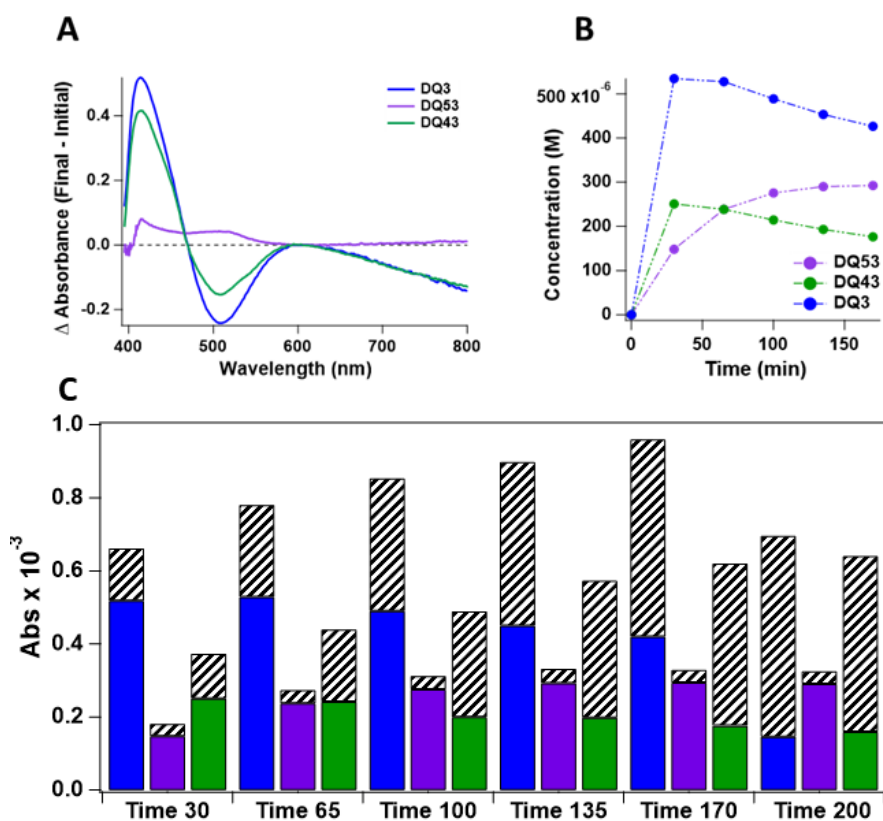


Figure 3.6 Radical decomposition product spectra and analysis. A) Difference spectra comparing final absorbances after subtracting initial radical populations. B) Concentration of mediator radical in solution over time. C) Bar graph summarizing the relative populations of decomposition product to radical over time. Color Scheme for figure is as follows: Blue = DQ03; Purple = DQ53; Green = DQ43.

Even more interesting, when the concentration of reduced mediator for all 3 mediators is plotted vs time (Fig 3.6B), the population of reduced mediator initially grows strongly for all three mediators. However, while the population of DQ53 reaches equilibrium around 100 min, DQ43 and DQ03 radical populations begin to decay around half this time mark (50 min). When a bar graph which plots relative absorbances of both the radical (colored bar) and decomposition (striped bar) product absorbances relative to each other is generated, two patterns are clear. First, as observed with the data presented in Fig 3.2B, the radical population for DQ53 (purple) grows until an equilibrium is achieved, from which point the radical population remains relatively constant and little to none of the decomposition product (striped bar) is observed. The opposite trend is observed for DQ43 and DQ03. While initially, for the first 50 min the radical population grows and remains relatively constant for a brief period. After this though, a sharp decline in the radical population for both DQ43 and DQ03 is observed while the absorbance of the decomposition product grows substantially until there is almost no radical left and the solution is dominated by decomposition product. These results present many interesting questions for the future of this work and the viability of these molecules as redox mediators for studies on longer timescales. Such as: what is the decomposition product? Could the rate of formation of this decomposition product be controlled by modifying sample conditions or would synthetic modifications be necessary to prevent this decomposition pathway from occurring? Considering that DQ53 does not seem to form a decomposition product, as was observed with DQ43 and DQ03, it seems likely that modification to these mediators would be necessary to prevent this decomposition pathway from occurring.

3.4 Transient Studies of Electron Quenching by Mediator Population and Charge Recombination

To better understand the ET mechanism unique to these mediators and further explain the trends in quantum efficiency observed in the steady state, transient absorbance visible kinetics were used to examine ET events occurring on the picosecond to microsecond timescale. This approach allows us to probe the influence structure and LUMO energy may have on charge transfer rate. By deepening our understanding of the role structural and electronic properties may have on ET in the formation and decay kinetics of the charge separated state, we aim to develop a more complete picture of how these types of systems might be improved or expanded.

3.4.1 Excited State Electron Quenching by Mediator LUMO

Upon excitation, a bleach, indicative of a localized electron-hole pair,^{7, 26-27} is generated in the CdSe QD with a lifetime of 100's of picoseconds (Fig 3.8A). Excited state bleach decay is consistent with charge extraction and indicates a return to the ground state of this material. By monitoring the band edge associated with the excited state of the CdSe QD (508 nm), we can effectively obtain the rate for the formation of the charge separated state (τ_{CS}). The kinetic measurements obtained from monitoring at 508nm were fit to a sum of exponentials to account for multiple electronic processes as well as inhomogeneities in the QD surface.^{23, 28} From this sum of exponentials amplitude weighted lifetimes were calculated to compare relative electron transfer rates between mediators and are listed in Table 3.3 at the end of this section.

The DQ42 mediator featured the fastest rate, with a τ_{CS} of 25.8 ps. Interestingly, the other mediator of a relatively low-lying energy LUMO had a τ_{CS} nearly twice this at 49.3 ps. This lifetime is very close to that of DQ03 (56.9 ps.) A similar trend is observed with DQ53 and DQ43, that is the lower energy LUMO featured the lifetime of charge separated state formation, 322 and 204 ps respectively.

In general, it was found that the rate of electron transfer from the quantum dot to the mediator correlates approximately with the mediator LUMO energy. However, given that the rates observed were opposite of what would be expected with a driving force argument when comparing DQ52 to DQ42 or DQ53 to DQ43, this is not sufficient to rationalize these observations. It is tempting to interpret these results as evidence of a structural effects on this

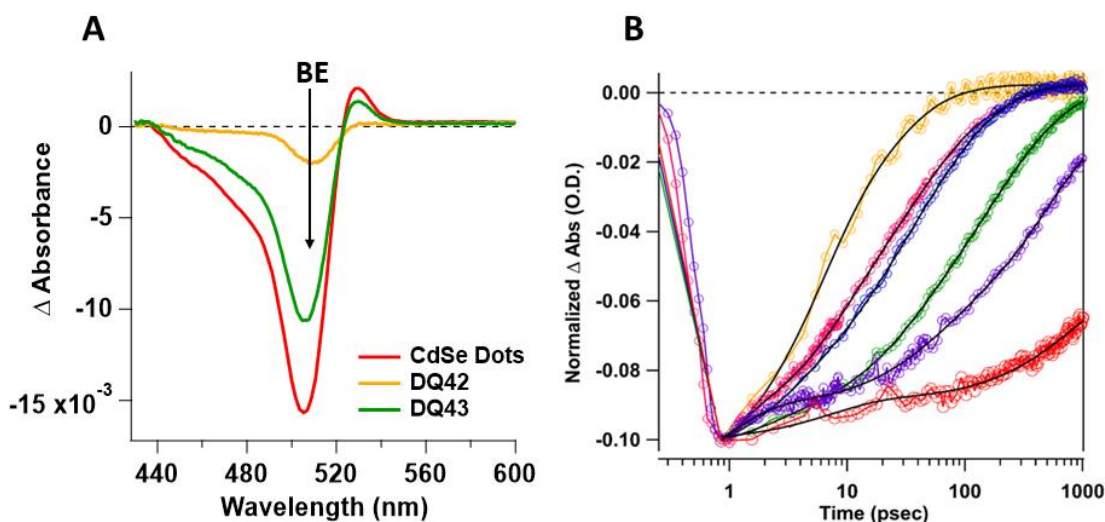


Figure 3.7 Ultrafast and nanosecond transient kinetics of mediator radical formation and decay.

A) Averaged absorbance spectra over 20 femtoseconds comparing CdSe QD band edge bleach decay in the presence of different mediators B) Normalized CdSe QD band edge bleach recovery kinetics comparing mediators. Mediator color scheme is as follows: . Yellow = DQ42, Pink = DQ52, Blue = DQ03, Purple = DQ53 and Green = DQ43

rate of ET. That the methyl groups have sufficient steric bulk to perturb the orbital overlap of the mediator to the quantum dot surface. This results in a longer τ_{CS} for those mediators with methyl groups in the 5-position. It is well established, that the degree of orbital overlap^{10, 13, 29-33} and distance between the donor acceptor³⁴ influences the rate of electron transfer. These results seem to fit this standard and indicate that the positioning of the methyl groups may provide enough steric hindrance to perturb this ET mechanism.

	Red. Pot. vs. SHE	ΔG_{CS} (eV)	AWL (ps)	$k_{CS,apparent}$ (ps ⁻¹)	Radical lifetime (μ s)	k_{CR} (μ s ⁻¹)
DQ52	-470 mV	0.27	49.3	0.02	2.84	0.35
DQ42	-490 mV	0.25	25.8	0.038	2.506	0.4
DQ3	-550 mV	0.19	56.9	0.018	.46	2.17
DQ53	-635 mV	0.105	322	0.003	1.15	.87
DQ43	-670 mV	0.07	204	0.005	1.43	.7

Table 3.3 Summary of transient data examining radical formation and lifetime rates.

3.4.2 Mediator Radical Charge Recombination

In the nanosecond to microsecond timescale, a broad absorbance feature at ~780 nm forms (Fig. 3.9A), similar to what is observed in the steady-state radical absorbance spectrum. The formation of this feature supports the conclusion that the mediator is performing electron extraction and forming a charge separated state. Because this feature is observed only with the formation of mediator radical and does not overlap with any other spectral features it can be used to monitor CR as the mediator^{•+} species is quenched. When no sacrificial donor is present in solution to quench the hole remaining in the photosensitizer material, back electron transfer from the acceptor to the donor will eventually occur. Capping ligands, such as MPA, can serve as hole

acceptors^{23, 35-37} and so some population of holes are likely quenched by this process along with those holes being quenched by CR.

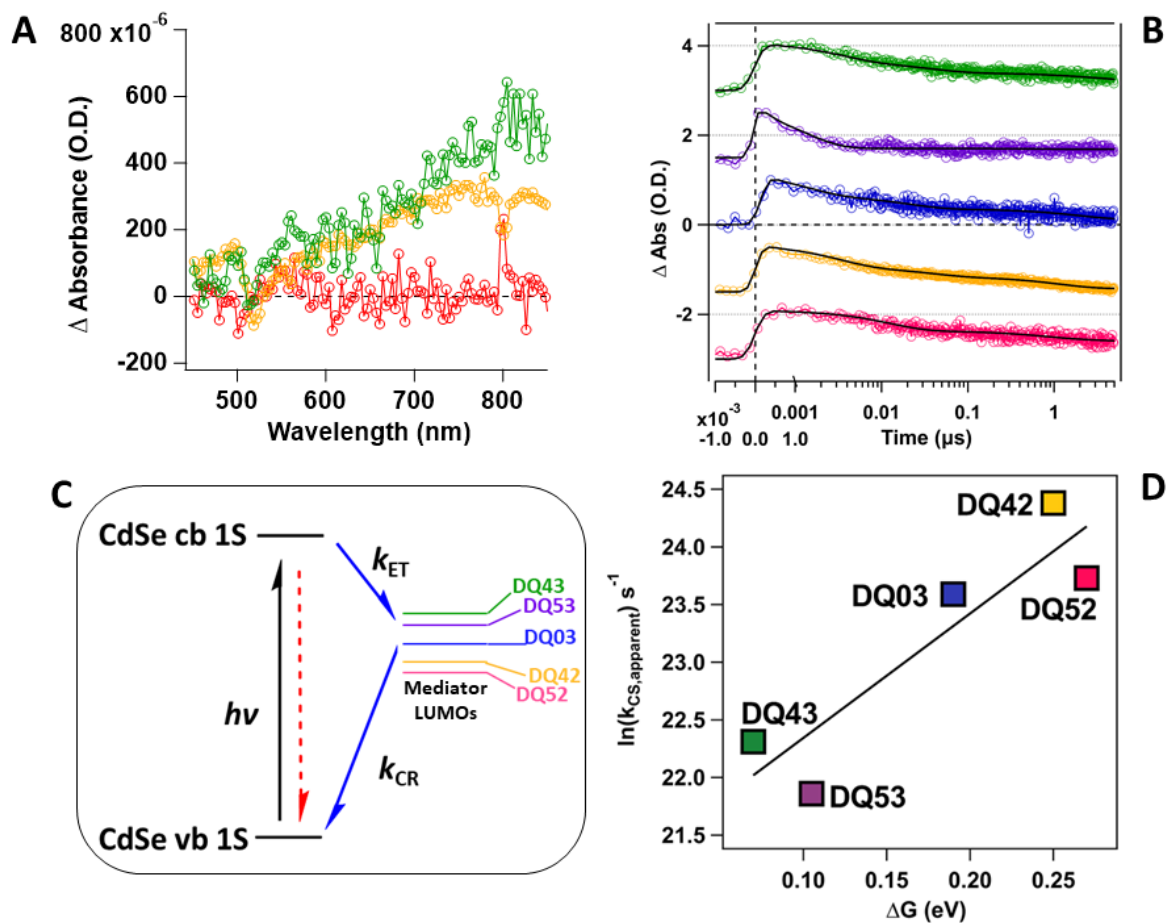


Figure 3.8 Nanosecond transient absorbance kinetics of mediator radical decay. A) Averaged absorbance spectra over 10's of nanoseconds comparing CdSe QD to mediators, DQ42 and DQ43. B) Kinetics of mediator radical decay over microseconds. C) Relative Energy diagram of mediator LUMOs and CdSe QD conduction band and valence band. D) Marcus plot of change in energy vs. natural log of rate of charge separated state formation. Mediator color scheme is as follows: . Yellow = DQ42, Pink = DQ52, Blue = DQ03, Purple = DQ53 and Green = DQ43.

From the values obtained for (τ_{CR}) by monitoring at 790 nm for each mediator, the lifetime of each radical was found to be at least as long as 0.5 μ s for DQ03 and up to nearly 3 μ s for DQ52, sufficiently long enough to reduce a catalyst or enzyme. From these results, it is apparent that the trend in τ_{CR} does not reflect those trends observed with forward electron transfer. That is, the rates largely follow the expected rates if governed exclusively by relative energy levels. This suggests that when the molecules have more comparable shape, in that they are closer to a planar configuration as predicted by computational studies, the influence of the energy of the HOMO is greater on charge recombination trends.

3.5 Conclusions

The first part of this study was primarily focused on evaluating the unique structural and electronic properties of the mediators presented by NMR, X-ray crystallography, and cyclic voltammetry. Based on the results of these analytical experiments, a clear relationship between electronic properties and structural features was established and opens the door to a convenient way to further modify or tune these redox mediators for a desired study or system.

In this body of work, we have optimized the hydrogen production efficiency of a hybrid photocatalytic system consisting of a NCS (CdSe QD) photosensitizer and a hydrogenase enzyme (*Pf* SHI). The performance was optimized by tuning the structure and reduction potential of the redox mediator that serves as an electron shuttle between the QD and enzyme. Optimum performance requires a careful balance among the rates of charge separation, ET to the enzyme and charge recombination, which can be achieved by tuning the energy of the mediator LUMO. The versatility of this modular system makes it attractive for additional studies with other photosensitizer materials and with other biological or man-made catalysts for PCET processes such as CO₂ reduction.

We also probed the electron transfer mechanism preliminarily with transient absorbance spectroscopy by determining the rates of apparent charge separation and recombination. From these values we concluded LUMO energy or a driving force argument alone is not sufficient to explain the trends in rates observed. This indicates some dependence on structure of the mediator species. The unique structural attributes of these mediators can inhibit the electron quenching process by disrupting orbital overlap between mediator and nanomaterial surface.

3.6 Appendix with Supplementary Data

Full experimental details for the ^1H NMR and electrochemistry experiments are presented in the analytical chapter.

3.6.1 ^1H NMR data of each mediator. ^1H NMR spectra of mediator salts post crystallization taken in D_2O . The three broad multiplet features that are assigned to the bridging protons are the result of diastereotopic protons resulting from a chiral molecule.

Figure 3.9.1 ¹H NMR of DQ52 mediator.

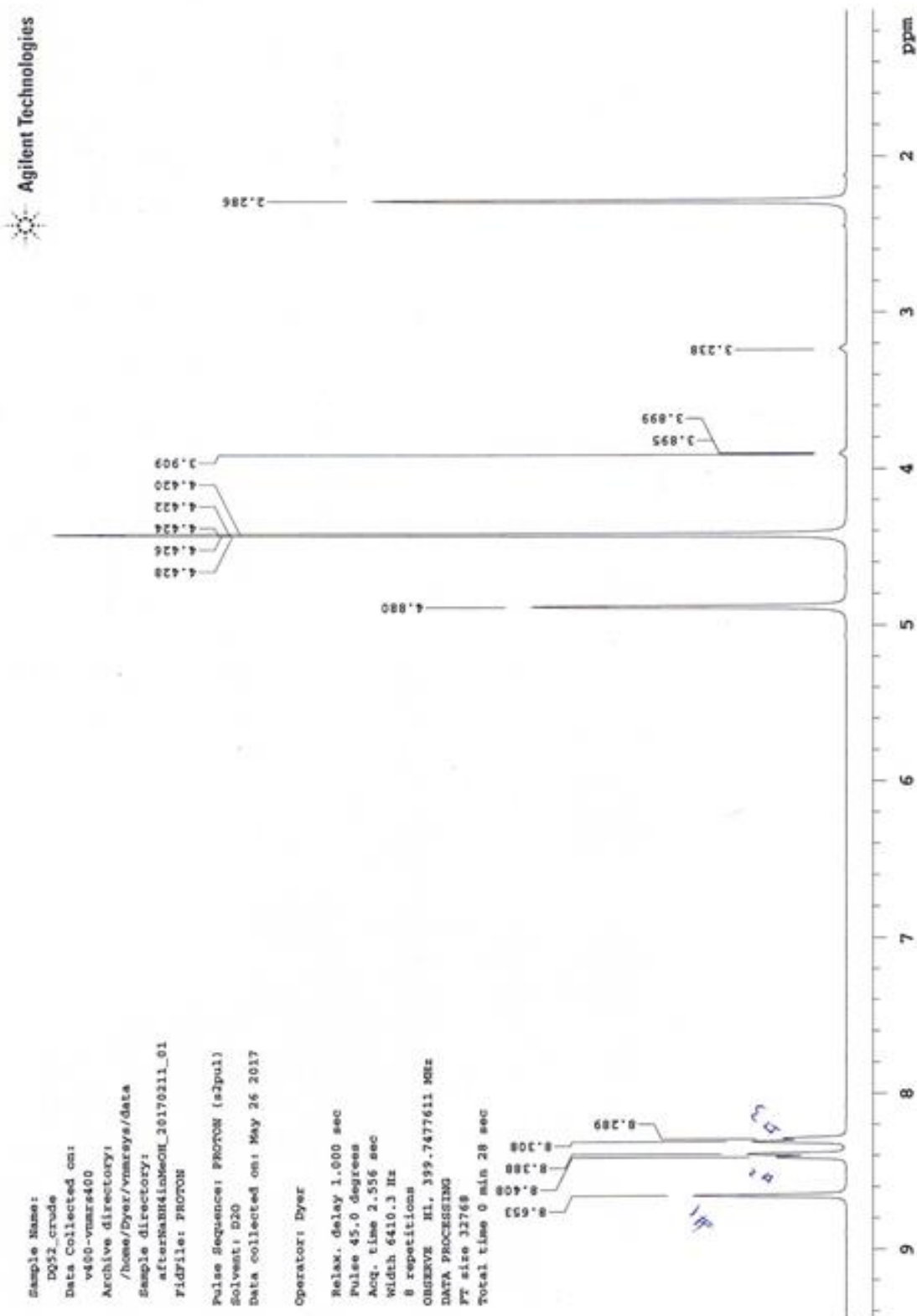


Figure 3.9.2 ^1H NMR of DQ42 mediator

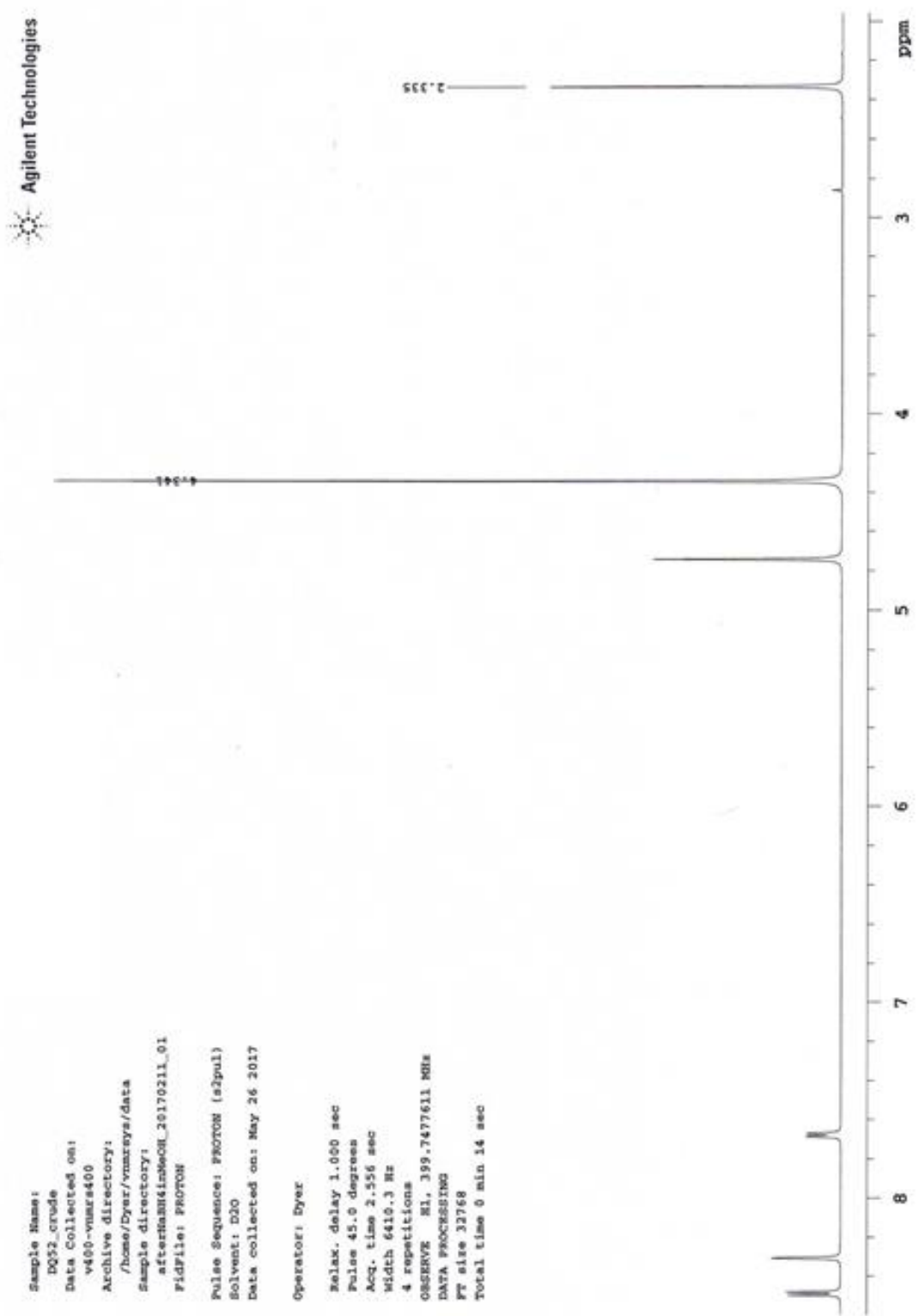


Figure 3.9.3 ^1H NMR of DQ03 mediator

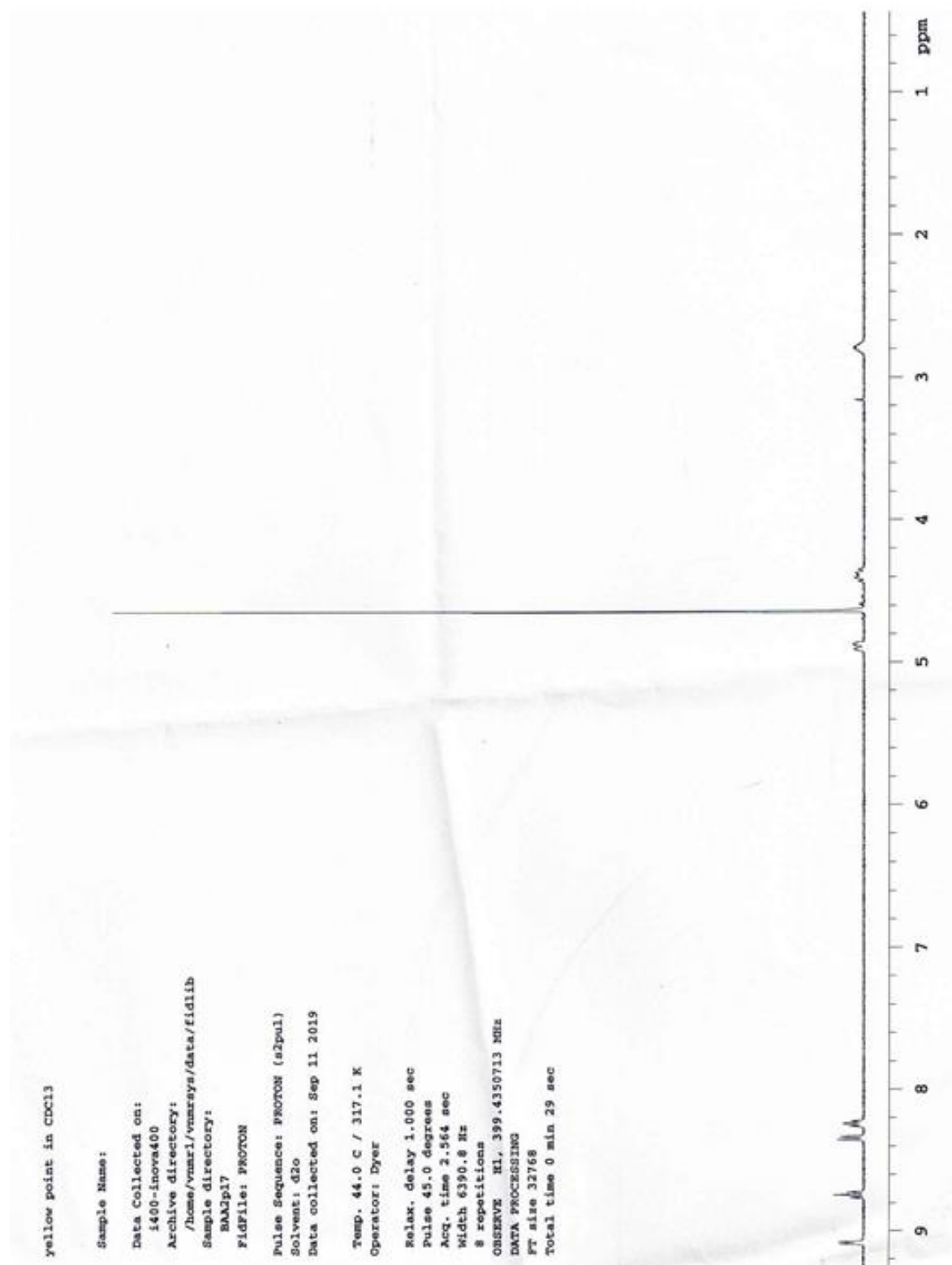


Figure 3.9.4 ¹H NMR of DQ53 mediator

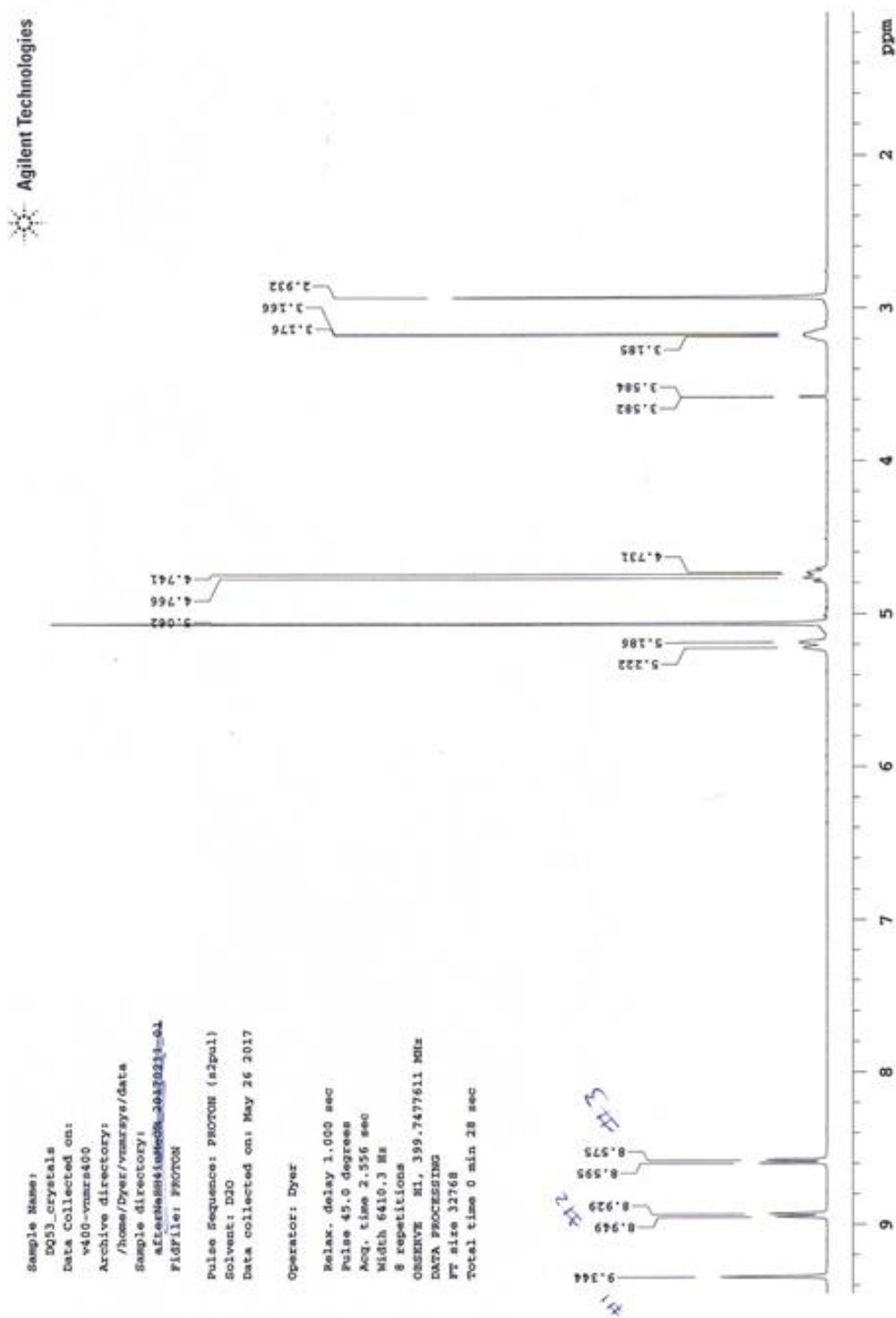
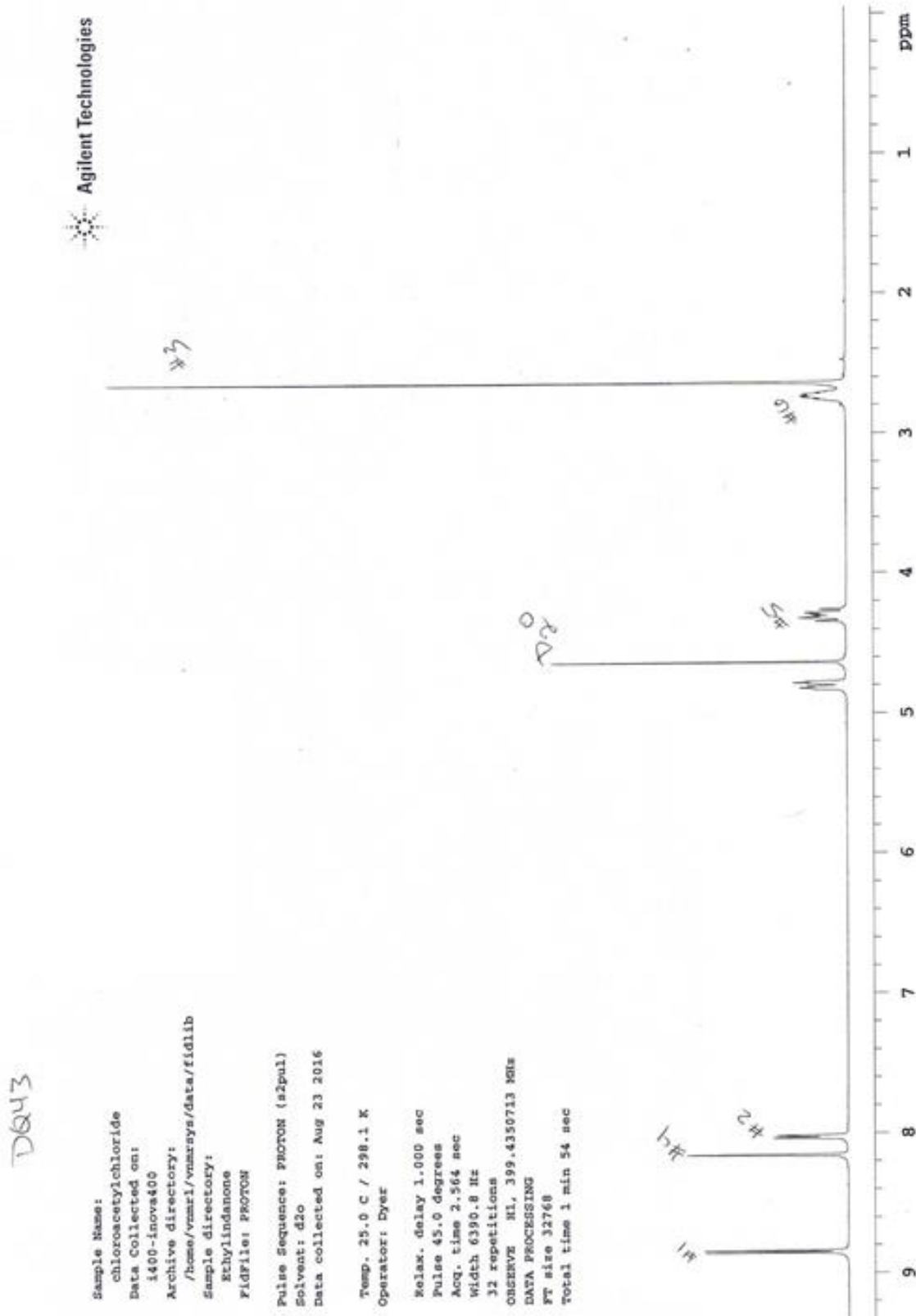


Figure 3.9.5 ^1H NMR of DQ43 mediator



3.6.2 Cyclic Voltammograms for each of the mediators. Full experimental details are included in the analytical chapter of this thesis.

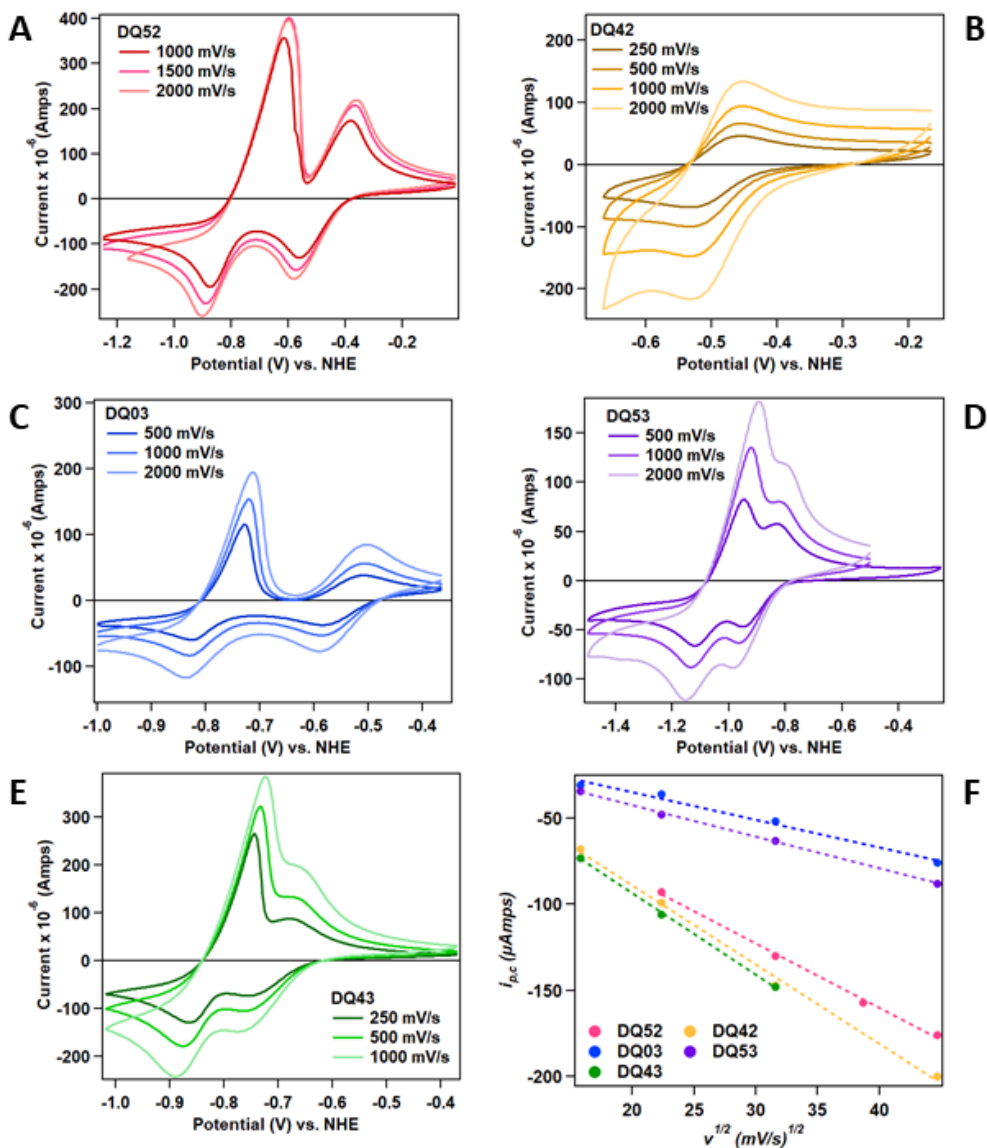


Figure 3.10 Cyclic voltammograms in water for each of the mediators pictured above: a) DQ42, b) DQ52, c) DQ03, d) DQ53, e) DQ43 and f) a plot of $v^{1/2}$ vs. $i_{p,c}$. These experiments were performed at pH 10 in borate buffer.

In the cyclic voltammograms (plots a-e), the peak-to-peak separation observed in the first cathodic wave when scanning at rates from 0.25 V/s up to 2 V/s for all 5 of the mediators indicates a high degree of reversibility for the first ET event of the first cathodic wave. The linear dependence on the scan rate is observed in plot f of Figure 3.5.2F indicates that the mediators remain homogeneous through the redox event.

Table 3.4 summary of Cyclic Voltammetry Data

	ΔE_p (mV)	E° (mV) vs. NHE	$I_{p,c}$ (μ Amps)
*DQ52	150	-470	-94
DQ42	75	-490	-100
DQ03	70	-550	-36
DQ53	108	-635	-34
DQ43	70	-670	-74

**Values reported for DQ52 are for data collected at 500 mV/s*

3.6.3 Summary of X-ray Diffraction Data

Deposition numbers from the Cambridge Crystallographic Data Centre: DQ52, 1896283;

DQ42, 1896285; DQ03, 1896284; DQ53, 1896286; DQ43, 1896282.

Compound	DQ52	DQ42	DQ03	DQ53	DQ43
Formula	C ₁₅ H ₂₀ Br ₂ N ₂ O	C ₁₄ H ₁₈ Br ₂ N ₂ O	C ₁₃ H ₁₅ Br ₂ N ₂ O _{0.5}	C ₁₅ H ₂₆ Br ₂ N ₂ O ₄	C ₁₅ H ₂₀ N ₂ OBr
<i>D</i> _{calc.} / g cm ⁻³	1.628	1.742	1.766	1.606	1.632
μ /mm ⁻¹	6.213	5.443	5.857	4.297	4.926
Formula Weight	808.30	390.12	367.07	458.20	404.15
Colour	colourless	colourless	colourless	colourless	colorless
Shape	block	needle	prism	prism	prism
Size/mm ³	0.26×0.22×0.18	0.20×0.12×0.09	0.69×0.47×0.29	0.53×0.39×0.14	0.33
<i>T</i> /K	100.00(10)	100(2)	100(2)	100(2)	0.30
Crystal System	triclinic	monoclinic	monoclinic	monoclinic	0.29
Space Group	<i>P</i> -1	<i>C</i> 2/ <i>c</i>	<i>C</i> 2/ <i>c</i>	<i>I</i> 2/ <i>c</i>	100(2)
<i>a</i> /Å	7.3138(2)	20.6558(11)	44.5365(10)	21.061(2)	monoclinic
<i>b</i> /Å	10.0105(3)	11.4656(3)	14.2236(5)	6.7995(7)	<i>P</i> 2 ₁ / <i>c</i>
<i>c</i> /Å	12.1578(2)	6.9238(3)	17.4936(4)	26.557(3)	11.1474(10)
α /°	104.745(2)	90	90	90	14.4208(12)
β /°	96.597(2)	114.868(6)	94.743(2)	94.682(12)	11.2139(10)
γ /°	103.047(3)	90	90	90	90
<i>V</i> /Å ³	824.44(4)	1487.73(13)	11043.7(5)	3790.4(7)	114.1500(10)
<i>Z</i>	1	4	32	8	90
<i>Z</i> '	0.5	0.5	4	1	1644.9(2)
Wavelength/Å	1.54184	0.710730	0.710730	0.710730	4
Radiation type	CuK α	MoK α	MoK α	MoK α	1
θ _{min} /°	3.824	2.082	2.246	1.539	2.002
θ _{max} /°	77.039	30.500	30.999	30.541	30.614
Measured Refl.	9300	16543	73108	24618	21850
Independent Refl.	3321	2261	17503	5768	5049
Reflections with <i>I</i> > 2(<i>I</i>)	3209	1887	10735	5118	4201
<i>R</i> _{int}	0.0273	0.0658	0.0648	0.0305	0.0431
Parameters	188	91	658	229	190
Restraints	1	27	726	60	3
Largest Peak	0.524	0.915	1.331	0.717	1.251
Deepest Hole	-0.565	-0.592	-0.607	-0.953	-0.606
GooF	1.117	1.083	1.042	1.087	1.062
<i>wR</i> ₂ (all data)	0.0801	0.0855	0.1179	0.0772	0.0903
<i>wR</i> ₂	0.0787	0.0809	0.1004	0.0735	0.0847
<i>R</i> ₁ (all data)	0.0313	0.0496	0.1074	0.0374	0.0466
<i>R</i> ₁	0.0286	0.0374	0.0524	0.0310	0.0353

3.7 References

1. Brown, K. A.; Harris, D. F.; Wilker, M. B.; Rasmussen, A.; Khadka, N.; Hamby, H.; Keable, S.; Dukovic, G.; Peters, J. W.; Seefeldt, L. C.; King, P. W., Light-driven dinitrogen reduction catalyzed by a CdS:nitrogenase MoFe protein biohybrid. *Science* **2016**, *352* (6284), 448.
2. Đokić, M.; Soo, H. S., Artificial photosynthesis by light absorption, charge separation, and multielectron catalysis. *Chemical Communications* **2018**, *54* (50), 6554-6572.
3. Greene, B. L.; Joseph, C. A.; Maroney, M. J.; Dyer, R. B., Direct Evidence of Active-Site Reduction and Photodriven Catalysis in Sensitized Hydrogenase Assemblies. *Journal of the American Chemical Society* **2012**, *134* (27), 11108-11111.
4. Brown, K. A.; Wilker, M. B.; Boehm, M.; Hamby, H.; Dukovic, G.; King, P. W., Photocatalytic Regeneration of Nicotinamide Cofactors by Quantum Dot–Enzyme Biohybrid Complexes. *ACS Catalysis* **2016**, *6* (4), 2201-2204.
5. Brown, K. A.; Dayal, S.; Ai, X.; Rumbles, G.; King, P. W., Controlled Assembly of Hydrogenase-CdTe Nanocrystal Hybrids for Solar Hydrogen Production. *Journal of the American Chemical Society* **2010**, *132* (28), 9672-9680.
6. Woolerton, T. W.; Sheard, S.; Chaudhary, Y. S.; Armstrong, F. A., Enzymes and bio-inspired electrocatalysts in solar fuel devices. *Energy & Environmental Science* **2012**, *5* (6), 7470-7490.
7. Chica, B.; Wu, C.-H.; Liu, Y.; Adams, M. W. W.; Lian, T.; Dyer, R. B., Balancing electron transfer rate and driving force for efficient photocatalytic hydrogen production in CdSe/CdS nanorod–[NiFe] hydrogenase assemblies. *Energy & Environmental Science* **2017**, *10* (10), 2245-2255.

8. Kodaimati, M. S.; McClelland, K. P.; He, C.; Lian, S.; Jiang, Y.; Zhang, Z.; Weiss, E. A., Viewpoint: Challenges in Colloidal Photocatalysis and Some Strategies for Addressing Them. *Inorganic Chemistry* **2018**, *57* (7), 3659-3670.
9. Zhu, H.; Song, N.; Lv, H.; Hill, C. L.; Lian, T., Near Unity Quantum Yield of Light-Driven Redox Mediator Reduction and Efficient H₂ Generation Using Colloidal Nanorod Heterostructures. *Journal of the American Chemical Society* **2012**, *134* (28), 11701-11708.
10. Weiss, E. A., Designing the Surfaces of Semiconductor Quantum Dots for Colloidal Photocatalysis. *ACS Energy Letters* **2017**, *2* (5), 1005-1013.
11. Peterson, M. D.; Jensen, S. C.; Weinberg, D. J.; Weiss, E. A., Mechanisms for Adsorption of Methyl Viologen on CdS Quantum Dots. *ACS Nano* **2014**, *8* (3), 2826-2837.
12. Morris-Cohen, A. J.; Vasilenko, V.; Amin, V. A.; Reuter, M. G.; Weiss, E. A., Model for Adsorption of Ligands to Colloidal Quantum Dots with Concentration-Dependent Surface Structure. *ACS Nano* **2012**, *6* (1), 557-565.
13. Morris-Cohen, A. J.; Peterson, M. D.; Frederick, M. T.; Kamm, J. M.; Weiss, E. A., Evidence for a Through-Space Pathway for Electron Transfer from Quantum Dots to Carboxylate-Functionalized Viologens. *The Journal of Physical Chemistry Letters* **2012**, *3* (19), 2840-2844.
14. Chen, J.; Wu, K.; Rudshiteyn, B.; Jia, Y.; Ding, W.; Xie, Z.-X.; Batista, V. S.; Lian, T., Ultrafast Photoinduced Interfacial Proton Coupled Electron Transfer from CdSe Quantum Dots to 4,4'-Bipyridine. *Journal of the American Chemical Society* **2016**, *138* (3), 884-892.
15. Campa, C.; Camps, J.; Font, J.; De March, P., Conformational studies of annulated 2,2'-bipyridinium salts. *The Journal of Organic Chemistry* **1987**, *52* (4), 521-525.

16. Brienne, S. H. R.; Boyd, P. D. W.; Schwerdtfeger, P.; Bowmaker, G. A.; Cooney, R. P., Infrared spectra and theoretical studies of bridged diquaternary 2,2'-dipyridinium compounds. *Journal of Molecular Structure* **1995**, 356 (2), 81-94.
17. Amao, Y.; Abe, R.; Shiotani, S., Effect of chemical structure of bipyridinium salts as electron carrier on the visible-light induced conversion of CO₂ to formic acid with the system consisting of water-soluble zinc porphyrin and formate dehydrogenase. *Journal of Photochemistry and Photobiology A: Chemistry* **2015**, 313, 149-153.
18. Yasui, S.; Itoh, K.; Ohno, A.; Tokitoh, N., Effect of structural change in viologen acceptors on the rate of single electron transfer from tributylphosphine. *Organic & Biomolecular Chemistry* **2006**, 4 (15), 2928-2931.
19. Pedersen, S. U.; Bo Christensen, T.; Thomasen, T.; Daasbjerg, K., New methods for the accurate determination of extinction and diffusion coefficients of aromatic and heteroaromatic radical anions in N,N-dimethylformamide. *J. Electroanal. Chem.* **1998**, 454 (1), 123-143.
20. Zhao, F.; Li, Q.; Han, K.; Lian, T., Mechanism of Efficient Viologen Radical Generation by Ultrafast Electron Transfer from CdS Quantum Dots. *The Journal of Physical Chemistry C* **2018**, 122 (30), 17136-17142.
21. Tsukahara, K.; Wilkins, R. G., Kinetics of reduction of eight viologens by dithionite ion. *Journal of the American Chemical Society* **1985**, 107 (9), 2632-2635.
22. Anderson, R. F.; Patel, K. B., Radical cations of some low-potential viologen compounds. Reduction potentials and electron-transfer reactions. *Journal of the Chemical Society, Faraday Transactions 1: Physical Chemistry in Condensed Phases* **1984**, 80 (10), 2693-2702.

23. Zhu, H.; Yang, Y.; Wu, K.; Lian, T., Charge Transfer Dynamics from Photoexcited Semiconductor Quantum Dots. *Annual Review of Physical Chemistry* **2016**, *67* (1), 259-281.
24. Greene, B. L.; Wu, C.-H.; McTernan, P. M.; Adams, M. W. W.; Dyer, R. B., Proton-Coupled Electron Transfer Dynamics in the Catalytic Mechanism of a [NiFe]-Hydrogenase. *Journal of the American Chemical Society* **2015**, *137* (13), 4558-4566.
25. Kundu, S.; Patra, A., Nanoscale Strategies for Light Harvesting. *Chemical Reviews* **2017**, *117* (2), 712-757.
26. Wilker, M. B.; Utterback, J. K.; Greene, S.; Brown, K. A.; Mulder, D. W.; King, P. W.; Dukovic, G., Role of Surface-Capping Ligands in Photoexcited Electron Transfer between CdS Nanorods and [FeFe] Hydrogenase and the Subsequent H₂ Generation. *The Journal of Physical Chemistry C* **2018**, *122* (1), 741-750.
27. Wilker, M. B.; Shinopoulos, K. E.; Brown, K. A.; Mulder, D. W.; King, P. W.; Dukovic, G., Electron Transfer Kinetics in CdS Nanorod-[FeFe]-Hydrogenase Complexes and Implications for Photochemical H₂ Generation. *Journal of the American Chemical Society* **2014**, *136* (11), 4316-4324.
28. Huang, J.; Huang, Z.; Yang, Y.; Zhu, H.; Lian, T., Multiple Exciton Dissociation in CdSe Quantum Dots by Ultrafast Electron Transfer to Adsorbed Methylene Blue. *Journal of the American Chemical Society* **2010**, *132* (13), 4858-4864.
29. Matsumoto, H.; Uchida, H.; Matsunaga, T.; Tanaka, K.; Sakata, T.; Mori, H.; Yoneyama, H., Photoinduced Reduction of Viologens on Size-Separated CdS Nanocrystals. *The Journal of Physical Chemistry* **1994**, *98* (44), 11549-11556.

30. Scholz, F.; Dworak, L.; Matylitsky, V. V.; Wachtveitl, J., Ultrafast Electron Transfer from Photoexcited CdSe Quantum Dots to Methylviologen. *ChemPhysChem* **2011**, *12* (12), 2255-2259.
31. Matylitsky, V. V.; Dworak, L.; Breus, V. V.; Basché, T.; Wachtveitl, J., Ultrafast Charge Separation in Multiexcited CdSe Quantum Dots Mediated by Adsorbed Electron Acceptors. *Journal of the American Chemical Society* **2009**, *131* (7), 2424-2425.
32. Leng, H.; Loy, J.; Amin, V.; Weiss, E. A.; Pelton, M., Electron Transfer from Single Semiconductor Nanocrystals to Individual Acceptor Molecules. *ACS Energy Letters* **2016**, *1* (1), 9-15.
33. Morris-Cohen, A. J.; Frederick, M. T.; Cass, L. C.; Weiss, E. A., Simultaneous Determination of the Adsorption Constant and the Photoinduced Electron Transfer Rate for a Cds Quantum Dot–Viologen Complex. *Journal of the American Chemical Society* **2011**, *133* (26), 10146-10154.
34. Yang, W.; Vansuch, G. E.; Liu, Y.; Jin, t.; Liu, Q.; Ge, A.; Sanchez, M. L. K.; K. Haja, D.; Adams, M. W. W.; Dyer, R. B.; Lian, T., Surface ligand “liquid” to “crystalline” phase transition modulates the solar H₂ production quantum efficiency of CdS nanorod/mediator/hydrogenases assemblies. *ACS Applied Materials & Interfaces* **2020**.
35. Cline, R. P.; Utterback, J. K.; Strong, S. E.; Dukovic, G.; Eaves, J. D., On the Nature of Trapped-Hole States in CdS Nanocrystals and the Mechanism of Their Diffusion. *The Journal of Physical Chemistry Letters* **2018**, *9* (12), 3532-3537.
36. Wu, K.; Du, Y.; Tang, H.; Chen, Z.; Lian, T., Efficient Extraction of Trapped Holes from Colloidal CdS Nanorods. *Journal of the American Chemical Society* **2015**, *137* (32), 10224-10230.

37. Song, N.; Zhu, H.; Jin, S.; Lian, T., Hole Transfer from Single Quantum Dots. *ACS Nano* **2011**, *5* (11), 8750-8759.

Chapter 4

Laser-Induced Potential-Jump: a Method for Rapid Electron Injection into Oxidoreductase Enzymes

Reproduced in part with permission from

Monica L. K. Sanchez,[†] Sara E. Konecny, [†] Sarah M. Narehood,[†] Edward Reijerse,[‡] Wolfgang Lubitz,[‡] James A. Birrell,^{‡*} R. Brian Dyer^{†*}. Laser-Induced Potential-Jump: a Method for Rapid Electron Injection into Oxidoreductase Enzymes.

Journal of Physical Chemistry B. **2020**, Accepted

4.1 Abstract

Oxidoreductase enzymes often perform technologically useful chemical transformations in a highly efficient manner under ambient conditions. However, without a well characterized and optimized approach to study these naturally occurring biocatalysts, progress in understanding how they work is limited. We have developed an approach for rapidly injecting electrons into a catalytic system to produce a solution potential jump, which then initiates turnover via electron transfer (ET) to the catalyst. Necessary for making this approach widely applicable, however, is detailed optimization of ET events at the nanomaterial-mediator-catalyst interfaces. For this purpose, we have employed a series of redox-active molecules ranging in redox midpoint potentials from -550 mV to -670 mV (vs SHE), CdSe/CdS core-shell nanorods, and an [FeFe] hydrogenase from *Chlamydomonas reinhardtii* (CrHydA1) as our model electron shuttles, photosensitizer and catalyst, respectively. With these components we screened a variety of experimental conditions such as, pH, mediator concentration, protein concentration, photosensitizer concentration and photon flux. Supported by results from steady state photoreduction and hydrogen production measurements, it is evident that the efficiency of the ET system is quite sensitive to the experimental conditions. Transient absorption spectroscopy measurements have yielded insight into the factors affecting the ET mechanism and efficiency of the potential jump. By manipulating these experimental conditions, we have shown the potential of simple modifications to improve the tunability of our system for application to study sensitive biocatalysts. We have also explored the use of a new material as photosensitizer for potential jump experiments. This alternate material allows for the use of green 532 nm light as excitation source rather than potentially damaging 355 nm light which is required with CdSe/CdS dot in rod nanorods.

4.2 Introduction

Oxidoreductase enzymes, such as hydrogenase, carbon monoxide dehydrogenase (CODH) and nitrogenase, catalyze a variety of important chemical transformations with efficiency and selectivity rarely observed in manmade molecular catalysts under ambient conditions using earth abundant transition metals.¹⁻² Hence, this class of enzymes, has been studied with the aim of reproducing these properties in artificial systems.²⁻⁴ However, study of these systems presents several experimental challenges, in particular, the complexity of initiating multi-electron and coupled proton transfer reactions to activate the stable small molecule substrates (H₂, CO₂ and N₂) as well as the stability and availability of the enzyme itself. Adding to these difficulties, many commonly studied oxidoreductase enzymes typically undergo hundreds up to thousands of turnovers per second, occupying intermediate states on the sub millisecond time scale.^{1, 5-6} It is possible to observe the more stable intermediates by titrating them thermodynamically or under steady state conditions.⁷⁻¹⁰ However, often the most interesting intermediates are the more reactive, and hence transient. It is for this reason that the application of traditional enzymology techniques for studying the catalytic mechanisms of many oxidoreductases is limited.³ Techniques that can probe the sample on an appropriate timescale are needed due to the short lifetime of these intermediate populations, but are currently under-developed.

To address this gap, several new approaches aimed at accessing these transient catalytic events have been developed recently. One such approach is the incorporation of nanocrystalline semiconductors (NCS) as a way to photo-initiate catalysis in the enzyme or molecular catalyst.¹¹⁻¹³ The NCS acts as a photosensitizer by absorbing light to create an exciton, followed by electron transfer to the catalyst. This approach relies on direct electron injection from the NCS to an

enzyme attached to its surface. Promising results have been obtained with this approach, both in improving lifetime of the enzyme relative to systems that use electrodes as the initiation method and in the mechanistic study of catalysts such as nitrogenase and hydrogenase.^{11-12, 14} Despite these breakthroughs, direct electron injection from the semiconductor to the enzyme is not a robust approach because of its low efficiency. Interfacial electron transfer (ET) is slow due to the long distances involved and the difficulty of controlling the enzyme orientation on the surface. Consequently, the ET efficiency is low due to competing parasitic processes such as radiative and non-radiative exciton decay as well as exciton-exciton annihilation.¹⁵ These unproductive pathways result in short-lived excited states and present a hurdle for photo-driven systems.¹⁶⁻¹⁷ One way to circumvent this issue is to incorporate a redox mediator that can efficiently quench electrons from the semiconductor, and then deliver them to the biocatalyst before these parasitic events can occur.¹⁸ Recently, we have developed and applied this mediated ET approach for rapidly injecting electrons into hydrogenases to initiate turnover.¹⁹ This method has allowed us to monitor active site chemistry on a subturnover timescale and to improve the quantum efficiency for photo-driven catalysis with an enzyme.^{3, 18, 20-21} The initial photoinduced ET step in the photosensitizer-mediator pathway happens very fast (<10 ns) with near unity quantum efficiency,^{18, 22} and results in the accumulation of reducing equivalents in the form of 1-electron reduced mediator. This accumulation leads to an extremely fast change in solution potential or a “*potential jump*.” A potential jump induced by a short-pulsed laser can be used to trigger enzyme turnover via fast ET to the enzyme at timescales much shorter than the steady-state turnover frequency. This approach has been used successfully to study two of the three classes of hydrogenase enzymes, [NiFe] and [FeFe] hydrogenases, on sub-turnover timescales.^{18-20, 23-25} Previous application of this approach to study hydrogenase, however, raised questions about the

details of this method.^{18, 20-21} Namely, what are the limits to efficiency and solution potential jump magnitude associated with different experimental conditions? How might the rate of ET change with the introduction of different conditions? Furthermore, systems such as CODH may require more negative solution potentials to achieve similar results, or in the case of nitrogenase, more reducing equivalents. To make this a viable approach for the study of such multi-electron oxidoreductases, bigger potential jumps and more precise control of their magnitude are needed.

With the goal of optimizing the laser induced potential jump as a general method for the study of oxidoreductases, we screened several experimental conditions including pH, mediator concentration, protein concentration, photosensitizer concentration and photon flux. We optimized conditions for the potential jump using an [FeFe] hydrogenase from *Chlamydomonas reinhardtii* (CrHydA1) as our model oxidoreductase enzyme. CrHydA1 is a convenient model system because of its extremely high turnover frequency (TOF), up to several thousands of turnovers per second.²⁶⁻²⁸ The results of this study improve our understanding of the factors that control the potential jump within the context of the [FeFe] hydrogenase studied previously with this method as well as open the door to the application of this approach to study other enzymatic systems.

4.3 Results and Discussion

4.3.1 System Components: Photosensitizer, Mediators and Catalyst

System components employed in this study were chosen so that comparisons can be drawn between previously published results and those presented here.^{18, 20-22} A nanocrystalline semiconductor CdSe/CdS dot-in-rod (DIR) was used as our model photosensitizer for its previously established high quantum efficiency for ET to this class of mediator.¹⁸ Upon photoexcitation of the DIR photosensitizer, an electron is promoted to the conduction band (CB), followed by ET to the mediator LUMO (Fig. 4.1B). This ET step occurs with near-unity quantum efficiency¹⁸ and results in a rapid (≈ 10 ns) potential jump as the solution potential becomes more negative by several hundred millivolts, triggering ET to the enzyme and enzyme turnover. Prior to use in experiments, the DIRs were characterized by TEM, UV-vis and fluorescence spectroscopies to confirm their size and electronic properties (Figure 4.1D and 4.1E).

This study also surveys three different propyl-bridged 2,2'-bipyridinium salts (DQ03, DQ53 and DQ43) as electron carriers (Fig. 4.1C). The utility of these mediators as electron shuttles has been demonstrated previously^{20, 29-30} but detailed analysis and quantification of their limitations under potential jump conditions remained in need of further exploration as only a few examples of these small molecules as electron shuttles exist in the literature. Like other viologens, these mediators have the advantage of forming long lived and relatively stable radical species that can persist in solution for hundreds of microseconds up to minutes.^{18, 21} They also have more negative redox midpoint potentials (higher energy LUMOs) than other commonly used mediators, such as methyl viologen. A higher energy LUMO has the advantage of increasing the rate of forward electron transfer to the catalyst because of a greater driving force, ultimately resulting in a higher net efficiency of the system.

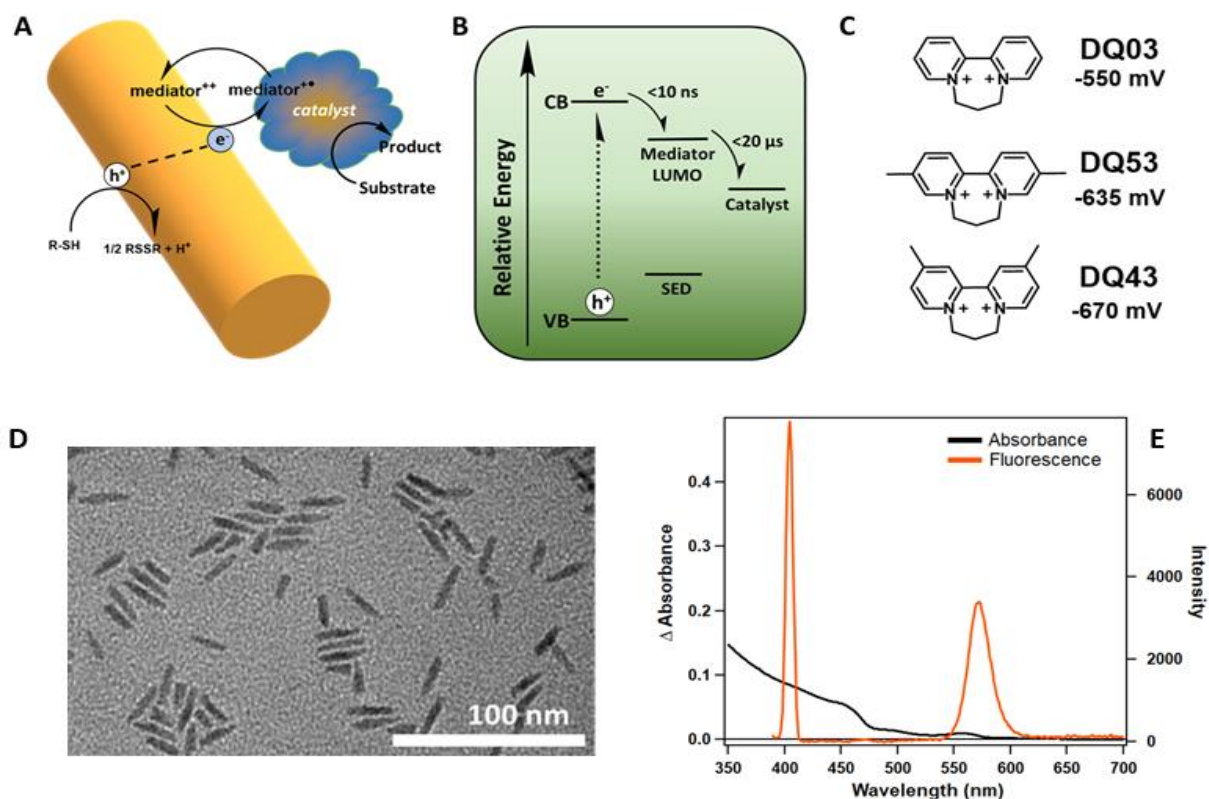


Figure 4.1 Potential Jump System Components. A) Schematic of overall ET pathway from photosensitizer to mediator to catalyst. B) Relative energy levels for each electron transfer step and component. C) The mediators investigated in this work: DQ03, DQ53 and DQ43. The nomenclature refers to the position of the methyl groups, (0= no methyl groups; 5=methyl groups in the 5-position; 4=methyl groups in the 4-position) and the number of carbons in the linker chain between the nitrogens (3=3-carbon chain). D) Transmission electron microscopy images of nanorods (NR) used for measurements presented in this chapter. E) Absorbance and emission spectra of the NRs used. *Abbreviations: VB = valence band; CB = conduction band; SED = sacrificial electron donor; LUMO = lowest unoccupied molecular orbital*

4.3.2 Steady-state Quantum Yield of Photo-driven Mediator Reduction and H₂ Production.

Steady-state photo-illumination experiments were performed to determine the quantum efficiency of light-driven mediator reduction (QE_{rad}) as a function of mediator concentration and pH. Illumination of the CdSe/CdS DIR with blue light (405 nm) produces an exciton state, which the mediator quenches by extracting an electron from the conduction band (CB) of the DIR, generating a reduced mediator population (mediator^{•+}). Representative absorbance spectra of the DQ03^{•+}, DQ53^{•+} and DQ43^{•+} species as they are generated with sample illumination are shown in Figure 4.2A. The absorbance feature at around 510 nm was monitored and used to determine the concentration of reduced mediator generated using Beer's Law. QE_{rad} was calculated using equation (1), by dividing moles of radical generated by moles of photons absorbed.^{18, 21, 31} The QE_{rad} is calculated from the first 10 s of illumination, before the concentration of mediator^{•+} builds up, thus minimizing contributions from back ET and other parasitic processes that lead to mediator degradation (full details of the calculation are presented in the SI). With this experiment, two key sets of conditions were compared, initial mediator concentration and pH, while consistently holding the concentration of photosensitizer to an optical density (OD) of 0.3 at 405 nm. This photosensitizer concentration was chosen to yield uniform excitation of the sample. An OD that is too high (greater than 0.6) leads to depletion of the pump laser and a transverse excitation gradient.

The starting concentration of the mediator is an important consideration, as use of too little can cause underperformance of the photosystem by leaving excited state electrons unquenched. On the other hand, a high starting mediator concentration relative to the concentration of nanoparticles in solution can lead to particle aggregation. The positively charged mediator associates electrostatically with the negatively charged carboxylate groups of

the mercaptopropionic acid (MPA) capping ligands on the DIR. When a concentration of mediator sufficient to neutralize the surface of the particle is reached, the nanocrystals tend to aggregate in water. This has been observed with smaller particles, MPA capped CdSe QDs,²¹ where the particles were observed to aggregate in solution when no enzyme was present and the mediator concentration was greater than 5 mM.

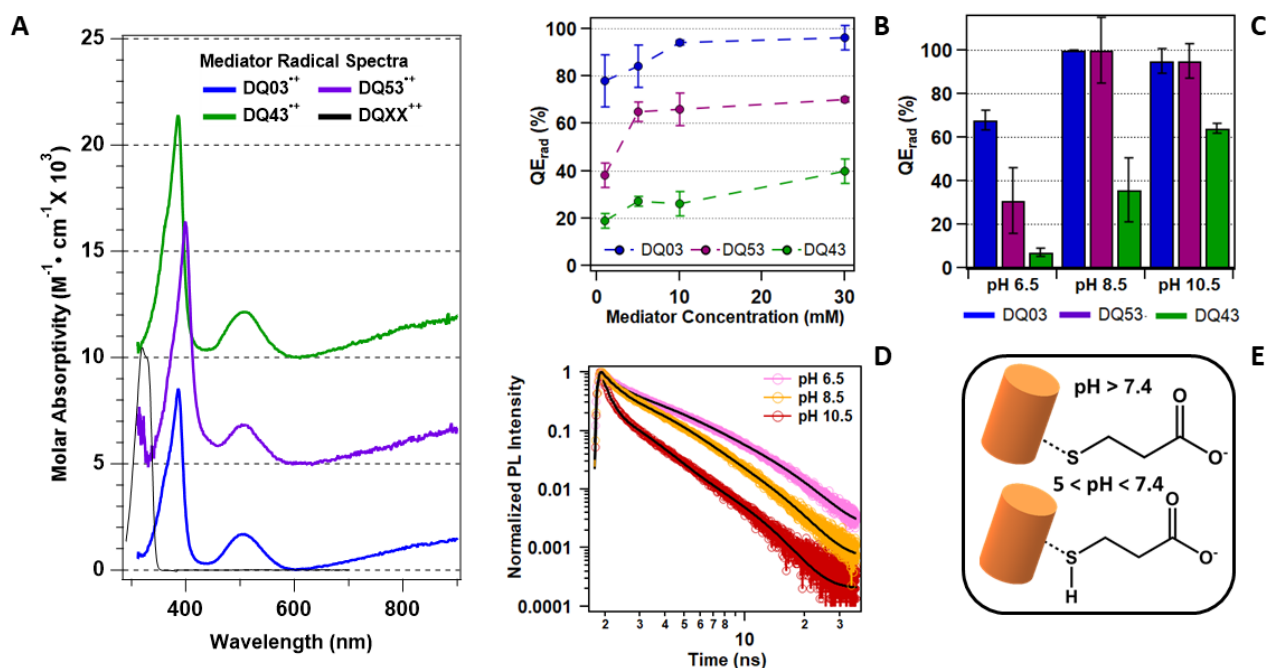


Figure 4.2 Steady-state mediator photoreduction and hydrogen production results. A) UV vis extinction spectra for reduced mediators compared to oxidized DQ03. B) Plot of mediator reduction quantum efficiency (QE_{rad}) vs mediator starting concentration at pH 7.4. C) QE_{rad} of mediator reduction vs pH with 25 mM mediator. D) Plot of the results from a time-correlated single photon counting experiment comparing hole transfer efficiency at pH 6.5, 8.5 and 10.5 (light pink = pH 6.5, gold = pH 8.5, maroon = pH 10.5) E) Schematic depicting the protonation state of mercaptopropionic acid capping ligand at denoted pHs. (*Figure adapted from poster generated by S. Narehood.*)

QE_{rad} was determined for all three mediators at four different concentrations: 1 mM, 5 mM, 10 mM, and 30 mM (at pH 7.4) and the results are summarized in Fig. 4.2B. For all three mediators, it was found that there was little benefit to having starting concentrations greater than 10 mM. Specifically, DQ03 already had a QE_{rad} of 80% at 1 mM while DQ53 and DQ43 gave lower QE_{rad} values (40% and 20%, respectively). Increasing the concentration of DQ03 to 10 mM gave a QE_{rad} of 95%, which could not be increased further. For DQ53, a concentration of 5 mM boosted the QE_{rad} to 65%, which increased slightly (to 70%) at 30 mM. For DQ43, increasing the mediator concentration gave a nonlinear increase in the QE_{rad} value up to 40% at 30 mM. The saturation behaviour observed for each mediator is due to its binding to the surface of the DIR through an electrostatic interaction between the negatively charged capping ligands of the nanomaterial and the positively charged mediator, as described earlier. Previously, we had measured the binding efficiency of DQ03 to DIR photosensitizers and found it to have a K_d of $\approx 100 \mu\text{M}$.¹⁸ Accounting for multiple binding sites on the surface of the DIR puts saturation in the 1-10 mM range. Once this saturating concentration is reached, maximum exciton quenching efficiency is achieved.

Another condition evaluated was the pH dependence of photo-driven mediator reduction. One limitation of this class of photosensitizer is that the capping ligand frequently used for application in aqueous media (mercaptopropionic acid) participates in acid base chemistry. The end that is covalently attached to the surface of the particle, a thiol group, can be deprotonated to form thiolate with a pK_a between 6 and 7. The consequence of deprotonation is an increase in exciton lifetime in the DIR (*vide supra*), improving the overall ET efficiency to the mediator. The other end of the ligand, a carboxylate, can be protonated under acidic conditions.

Protonation of the capping ligand neutralizes the DIR structure leading to aggregation and precipitation, setting the lower pH limit of around 6.

Photo-driven mediator reduction was performed across a range of pH values (6.5, 8.5 and 10.5) to evaluate this dependency and its influence on QE_{rad} while maintaining the mediator concentration at 25 mM (Fig 4.2C). From this study, it was determined that more alkaline conditions led to greater observed QE_{rad} for mediator reduction. Specifically, DQ03 had a QE_{rad} of $\approx 60\%$ at pH 6.5 while DQ53 and DQ43 gave lower QE_{rad} values (35% and 7%, respectively). Increasing the pH of the solution to pH 8.5 gave a QE_{rad} greater than 90%, for both DQ03 and DQ53. For DQ43, a solution pH of 8.5 increased the QE_{rad} to 37%. The QE_{rad} of DQ43 continued to improve slightly at even more basic conditions (to 60%).

We reasoned that this pH dependent trend was likely related to pH dependent-hole transfer effects. Because the nanomaterial capping ligand MPA can act as a hole acceptor for the initial excitonic state, the hole transfer efficiency is affected by the charge of the capping ligand.^{18, 32} If the thiol group of the capping ligand is deprotonated (thiolate), more efficient hole transfer is expected compared to when it is protonated. The presence of hydroxide can also be a contributing factor as hydroxide has been shown to actively participate in hole scavenging.³³ More efficient hole scavenging reduces the parasitic process of back electron transfer, thereby increasing the efficiency of mediator reduction. Because hole filling quenches the photoluminescence (PL) of the nanomaterial, PL lifetimes are a direct probe of hole transfer rates.³⁴⁻³⁶ We measured the PL lifetimes using time correlated single photon counting in order to compare hole transfer efficiencies at different pH values (Fig 4.2D). As the pH was increased, faster hole transfer rates to the capping ligand were observed compared to acidic pH. The hole transfer lifetime for the DIR sample can be determined by fitting the change in PL intensity to a

sum of exponential functions and calculating the amplitude weighted lifetime (AWL). The multi-exponential behaviour of the PL intensity decay is partly due to the heterogeneity of the surface of the material, trap states and localization of holes on the DIR surface. From this experiment it was found that the DIR sample at pH 6.5 featured a hole transfer lifetime ($\tau = 3.24$ ns) that was approximately 7 times slower than for the sample at pH 10.5 ($\tau = 0.46$ ns).

Finally, the mediators were compared for their efficacy as electron carriers to *CrHydA1* by the production of H₂ gas. This experiment was performed at pH 7.5 with 25 mM mediator, conditions chosen to optimize the performance of the catalyst while balancing the efficiency of the DIR-mediator system. The amount of H₂ generated was determined by monitoring the change in pressure vs. illumination time (Fig. 4.3A) using a home-built pressure sensor mounted in the cuvette cap. DQ43 gave the highest rate of H₂ production, over two times higher than the poorest performing mediator, DQ03. We reasoned this is due to the more negative solution potential generated by using a mediator that has a more negative redox midpoint potential leading to an overall greater increase in driving force for forward electron transfer to *CrHydA1*. Indeed, by monitoring the UV-vis spectrum during the assay, we were able to quantify the amount of reduced mediator generated (Figure 4.3B). These results showed that DQ43 achieved a much more negative solution potential (-0.55 mV) than DQ53 and DQ03 (-0.47 mV and -0.42 mV respectively.) We conclude that the significant difference in solution potential reached for each mediator, and so driving force for enzyme reduction, is responsible for the observed trend in hydrogen production.

In all cases, the observed rate of H₂ production was far less than the maximum turnover rate of up to several thousand per second measured for *CrHydA1* under similar conditions.³⁷ Because the rate of mediator radical formation (ranging between 0.5 and 1.5 s⁻¹) is closely

correlated with the rate of H₂ production, it is clear the rate of radical formation was the limiting factor in these experiments. The rate of production of reduced mediator is in turn limited by the fluence of the diode laser light source, because the overall quantum yield of this process approaches unity. Thus, a higher laser fluence should yield a greater H₂ production rate, closer to what has been observed previously for this enzyme when the electron source is not limited.

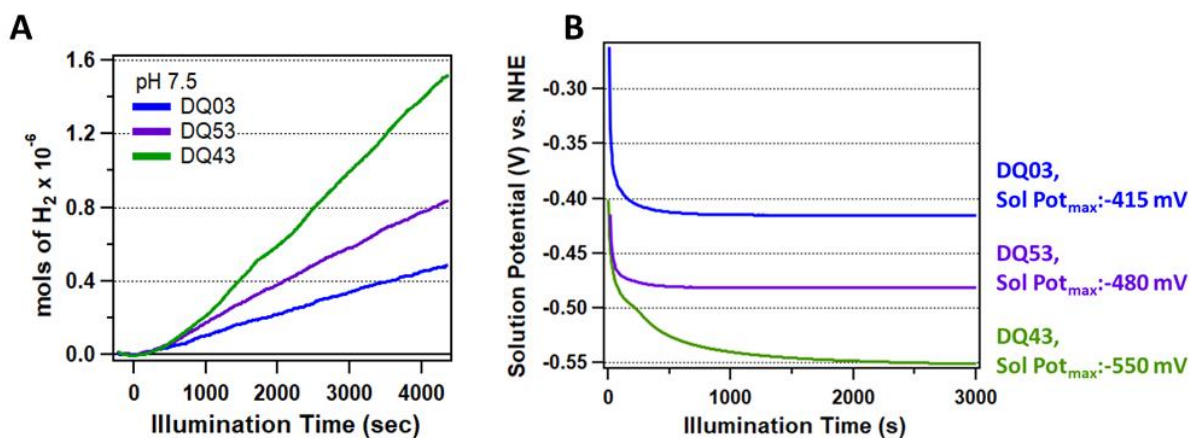


Figure 4.3 Steady-state hydrogen production study. A) Light-driven H₂ production assays with DIR-mediator-CrHydA1 under optimized conditions at pH 7.5 with 25 mM mediator. (Blue = DQ03, purple = DQ53, and green = DQ43) B) A plot of solution potential (mV) vs Illumination Time (sec). Sol Pot_{max} has been calculated at 2500 sec using the Nernst

$$\text{Equation: } \Delta E = \Delta E^\circ - \frac{RT}{F} \ln \frac{[\text{med}^{\cdot+}]}{[\text{med}^{2+}]}$$

4.3.3 Factors Affecting Potential Jump

The broad application of the laser induced potential jump technique to the study of oxidoreductase enzymes requires the elucidation of factors which tune its magnitude and lifetime. Like the approach taken in the steady-state experiments, a variety of conditions were surveyed: photon flux, photosensitizer concentration, mediator midpoint potential and pH dependence. These factors were each found to contribute considerably to the magnitude of the jump, and thus to the transient change in solution potential.

For this study, visible transient absorption (TA) spectroscopy was used to monitor the transient radical population. The production of reduced mediator and decay was monitored by probing the near IR absorbance band of the one electron reduced state of these mediators at 785 nm. Because the timescale of the transient measurements could potentially report on changes in the ground-state of the DIR, a probe wavelength that does not overlap with any of the DIR absorbance bands is needed. So rather than using the feature around 510 nm as in the steady-state experiments, the 785 nm wavelength was used to probe the population of mediator^{•+} without potential convolution from transient features related to the DIR. A 510 nm probe is appropriate for steady-state experiments because it gives a better signal-to-noise ratio and is performed on a timescale too slow to capture any changes in absorbance related to the DIR. For these reasons, 785 nm is the more reliable probe to quantify the concentration of reducing equivalents generated in the time-resolved experiments. The samples were prepared anaerobically with a mediator concentration of 25 mM and DIR absorbance of 0.2 at 355 nm (except for samples containing 2X the amount of nanorods) to maintain consistent photon absorption between samples. The first condition evaluated was the laser fluence. The range of laser fluence explored spanned 25 mJ per cm² to 150 mJ per cm² for each mediator at pH 6.5, 7.5, or 8.5. A

representative data set is presented in Figure 4.4A. The 785 nm absorption signal due to mediator radical formation rises with an instrument limited lifetime of <10 ns. The concentration of radical produced varied between 100 μM and 10 mM depending on pump power and sample conditions. From the change in absorbance (ΔA) at 1 μs , the concentration of reduced mediator

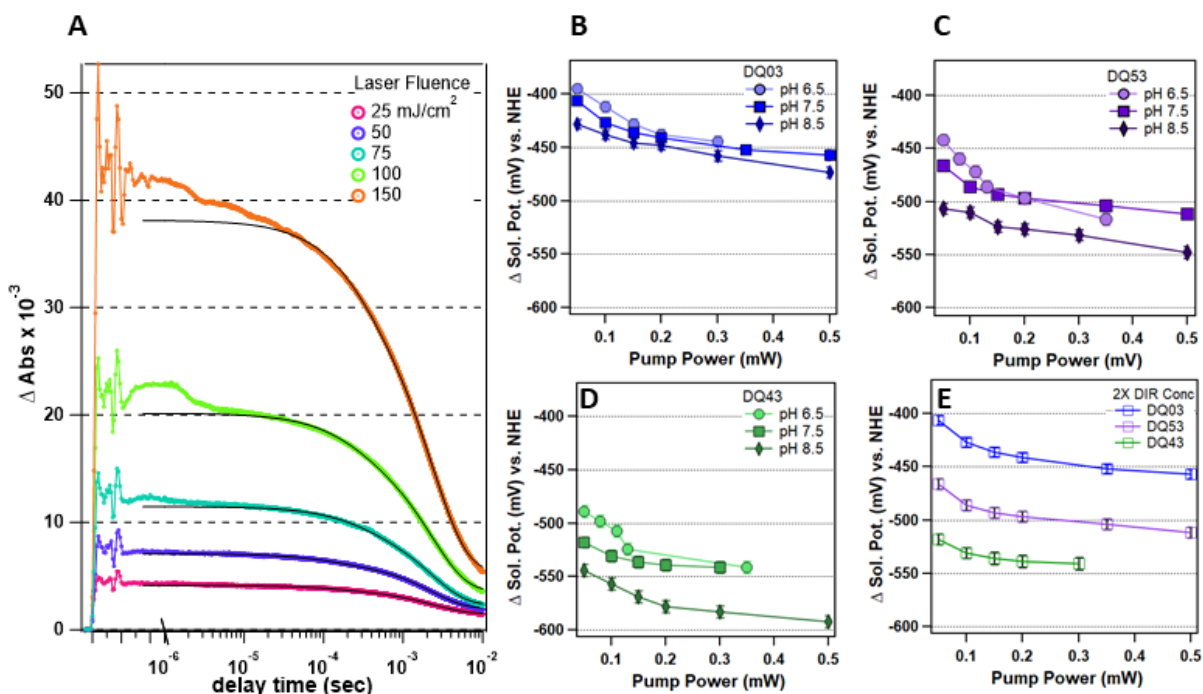


Figure 4.4 Representative transient absorbance data examining the pump power dependence under various conditions and how it relates to changes in solution potential. A) Representative set of pump power dependence and TA data for DQ53 at pH 8.5. (Color scheme: magenta = 25 mJ/cm^2 , blue = 50 mJ/cm^2 , turquoise = 75 mJ/cm^2 , light green = 100 mJ/cm^2 , and orange = 150 mJ/cm^2) B) Summary of pump power dependence data at different pH values for DQ03. C) Summary of pump power dependence data at different pH values for DQ53. D) Summary of pump power dependence data at different pH values for DQ43. E) Summary of pump power dependence data at pH 7.5 for samples containing 2X the normal concentration of DIR. Symbols: circles = pH 6.5, squares = pH 7.5, diamonds = pH 8.5

and the solution potential were calculated using Beer’s Law and the Nernst Equation (full details of these calculations are presented in the analytical portion of this thesis).^{20, 38-39}

Consistent with observations made in the steady-state photo-driven mediator reduction experiments, the greatest jumps were observed at pH values greater than 7. For example, the DQ03 sample showed an initial formation of 0.1 mM radical at the greatest pump power for pH 6.5, but 0.4 mM radical was achieved at pH 8.5. This corresponds to a solution potential ≈ 30 mV more negative at pH 8.5 than at pH 6.5 (Figure 4.4B). DQ53 and DQ43 followed a similar pattern, though because of their more negative reduction potentials, larger jumps were observed. For example, at pH 6.5 the largest jump observed for DQ53 (Fig 4.4C) had a solution potential of -505 mV, but at pH 8.5 the largest pump power resulted in a solution potential 45 mV more negative. DQ43 (Fig 4.4D) continued this trend with a jump ≈ 35 mV more negative at pH 8.5 than at pH 6.5.

When the concentration of DIR was doubled, greater jumps were observed under the same pH conditions (Fig 4.4E), leading to increases in the radical concentration at the greatest pump power. These results of the pump power and pH dependence are summarized in Table 4.1.

Pump Power (Watts)	DQ03			DQ53			DQ43		
	pH 6.5	pH 7.5	pH 8.5	pH 6.5	pH 7.5	pH 8.5	pH 6.5	pH 7.5	pH 8.5
0.05	-395	-406	-428	-442	-466	-507	-490	-536	-544
0.10	-412	-427	-438	-460	-486	-510	-498	-534	-557
0.15	-428	-436	-446	-472	-493	-524	-507	-541	-569
0.20	-438	-441	-448	-486	-497	-526	-524	-545	-578
0.35	-444	-452	-458	-513	-504	-532	-541	-547	-583
0.50		-457	-473		-512	-548		-554	-592

Table 4.1 Summary of pump power and pH dependence results from TRVis experiments.

It is worth noting that greater than 80% of the radical signal formed decays by ≈ 5 ms in these TA experiments despite the absence of an electron acceptor (e.g. hydrogenase or other catalyst). This decay occurs consistently with a half-life of ≈ 2 ms for all three mediators. The similarity in decay rates indicates an effect that is intrinsic to the mediator radical itself and is not influenced by pH. We attribute this decay to the formation of what is described as a “pimer” state or the π -stacking of two one-electron reduced mediators (Figure 4.5).⁴⁰⁻⁴¹ Upon reduction, bipyridinium molecules undergo a change in conformation from a twisted state to a more planar configuration (step 1) allowing π -stacking to occur and the pimer state to form (step 2). Once formed, the pimer state will readily undergo disproportionation to form the doubly reduced mediator and reform the dication in solution (step 3).⁴²⁻⁴³ The decay observed is due to the disappearance of the mediator^{•+} in favor of formation of mediator⁺⁺ and mediator⁰. It has been reported that the formation of the pimer state causes a small redshift in the near IR absorbance band, which may also contribute to the observed decay.

The doubly reduced mediator⁰ is insoluble in water and therefore not likely to be an effective electron carrier. We were unable to identify a spectroscopic signature for this state, so we do not know how long it persists in solution following the disproportionation reaction. Furthermore, the TR-IR measurements (Fig. 4.6) indicate that the doubly reduced mediator⁰ produced in the slow disproportionation process does not reduce the enzyme (no enzyme reduction occurs on this timescale). We conclude that the process of pimer disproportionation is an unproductive pathway that limits the potential jump to the ms timescale. Nevertheless, the

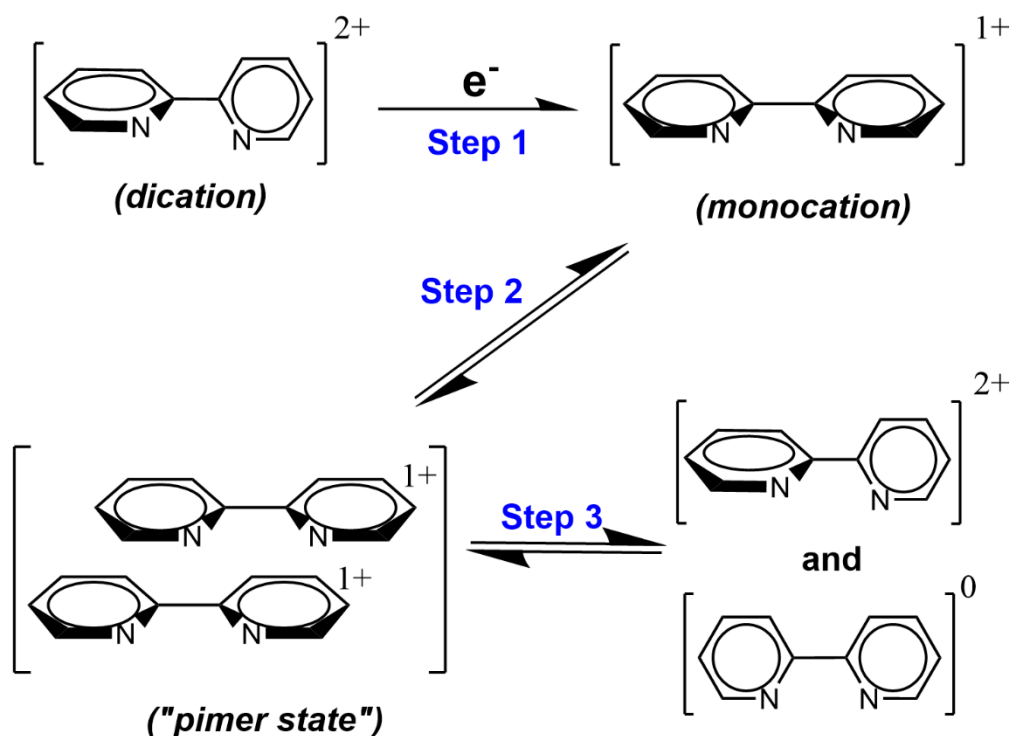


Figure 4.5 Schematic describing the pimer formation process. Upon one electron reduction of the dication mediator (step 1) to form the monocation species, a change in orientation of the two pyridine rings results in a more planar configuration of the mediator. This planar configuration allows for the formation of the “pimer state”(step 2) and from which disproportionation can occur (step 3). *Bridging carbons and methyl groups have been omitted from this scheme for clarity.

radical population persists long enough to drive catalysis in the case of hydrogenase. If the reaction of reduced mediator with the target enzyme is slow (on the ms timescale), this radical decay pathway will greatly reduce the efficiency of the system. This is observed even in hydrogenase experiments when a low enzyme concentration is used.²⁰ For other enzymes, the ET might be intrinsically slow (not diffusion limited) and therefore inherently inefficient due to this parasitic pathway.

Even though the presence of the parasitic process of pimer disproportionation limits the potential jump to the ms timescale, the radical population persists long enough to drive catalysis. However, if the reaction of reduced mediator with the target enzyme is slow (on the ms timescale), this radical decay pathway will greatly reduce the efficiency of the system. This is observed even in hydrogenase experiments when low enzyme concentration is used.²¹ For other enzymes, the ET might be intrinsically slow (not diffusion limited) and therefore inherently inefficient due to this parasitic pathway.

4.3.4 Kinetics of ET to *CrHydA1* Hydrogenase

A laser induced potential jump coupled with transient absorbance (TA) in the visible and infrared were used to follow the kinetics of ET from mediator to *CrHydA1* and subsequent formation of intermediate states on a sub-turnover timescale, respectively. Two potential jump samples containing *CrHydA1* were prepared with differing enzyme concentrations (1 mM and 4 mM) at pH 7.4, 25 mM DQ03 mediator and 100 mM MPA as SED. These enzyme concentrations were chosen to examine the effect on the kinetics of varying the ratio of reducing equivalents to protein. The radical concentration generated in the potential jump is held constant in these experiments, yielding a ratio of reducing equivalents: enzyme of approximately 1:2 for the 1 mM sample and 1:8 for the 4 mM sample. Although DQ03 did not perform as well as DQ43 for light driven H₂ production, we chose DQ03 for these experiments to directly compare performance to results previously obtained with *CrHydA1* and CdSe/CdS NRs.²⁰ The radical population was monitored in the same way as in the previous TA experiments, when no enzyme was present, by probing at 785 nm. Additionally, intermediate populations were monitored in the infrared to determine if there is a difference in population flux through different intermediate states when exposed to varying concentrations of radical.

The population of mediator radical was monitored by TA at 785 nm (Fig. 4.6C), showing significant differences in decay of the radical signal for the 1 mM and 4 mM samples. For the lower enzyme concentration (1 mM), three kinetics phases were observed (Fig. 4.6C), with lifetimes of 15 μ s, 60 μ s and 2.2 ms. There are 3 possible radical decay pathways: charge recombination (CR), ET to enzyme (ET) and pimer disproportionation (PD). The three lifetimes observed for the 1 mM enzyme sample correspond to these three pathways; the same 15 μ s and 2.2 ms phases are observed in control experiments without the enzyme (Fig. 4.6A), therefore we

assign them to the CR and PD processes, respectively. The intermediate phase ($\tau = 60 \mu\text{s}$) represents ET to the enzyme. The fastest kinetics phase may also have some contribution from ET to the enzyme, based on the TR-IR data (Fig. 4.6). Although there is an excess of enzyme present, some radical still decays by the PD pathway with its characteristic lifetime of 2.2 ms. We postulate that pimer formation is fast and competitive with the ET pathway under these conditions, and that its decay rate is determined by the rate of disproportionation. All three radical decay pathways are bimolecular (they require mediator:rod, mediator:enzyme or mediator:mediator collisions, respectively) and thus should be concentration dependent up to a point of saturation.²⁰ When the *CrHydA1* enzyme concentration is increased to 4 mM, the radical population decayed monoexponentially to zero with a 20 μs lifetime. With the increased enzyme concentration, the ET pathway is as fast as the CR pathway, therefore only a single exponential decay is observed. Furthermore, the PD pathway is no longer observed in this case, likely because pimer formation is no longer competitive with ET.

The populations of multiple intermediate states of the active site (H-cluster) in the [FeFe] hydrogenase were also monitored to determine the influence of the magnitude of this first reduction step on intermediate population dynamics (Fig. 4.6). The H-cluster is composed of a canonical [4Fe-4S] cluster attached to a unique [2Fe] cluster containing two terminal CO and two terminal CN⁻ ligands, a bridging CO ligand, and a bridging 2-azapropane 1,3-dithiolate ligand (Fig 4.6A).²⁸ The CO and CN⁻ ligands have vibrational frequencies in a mid IR region free of protein absorbance (1800 cm^{-1} – 2200 cm^{-1}). The vibrational frequencies of the CO ligands are particularly sensitive to the oxidation and protonation states of the H-cluster and so the distribution of catalytic intermediates can be followed by tuning in to a specific CO frequency (Fig. 4.6B). The CO peaks are easily monitored by TA methods because of their relatively large

extinction coefficients and because there are often multiple frequencies assigned to an intermediate, aiding the selection of a frequency which reports on a single intermediate population.

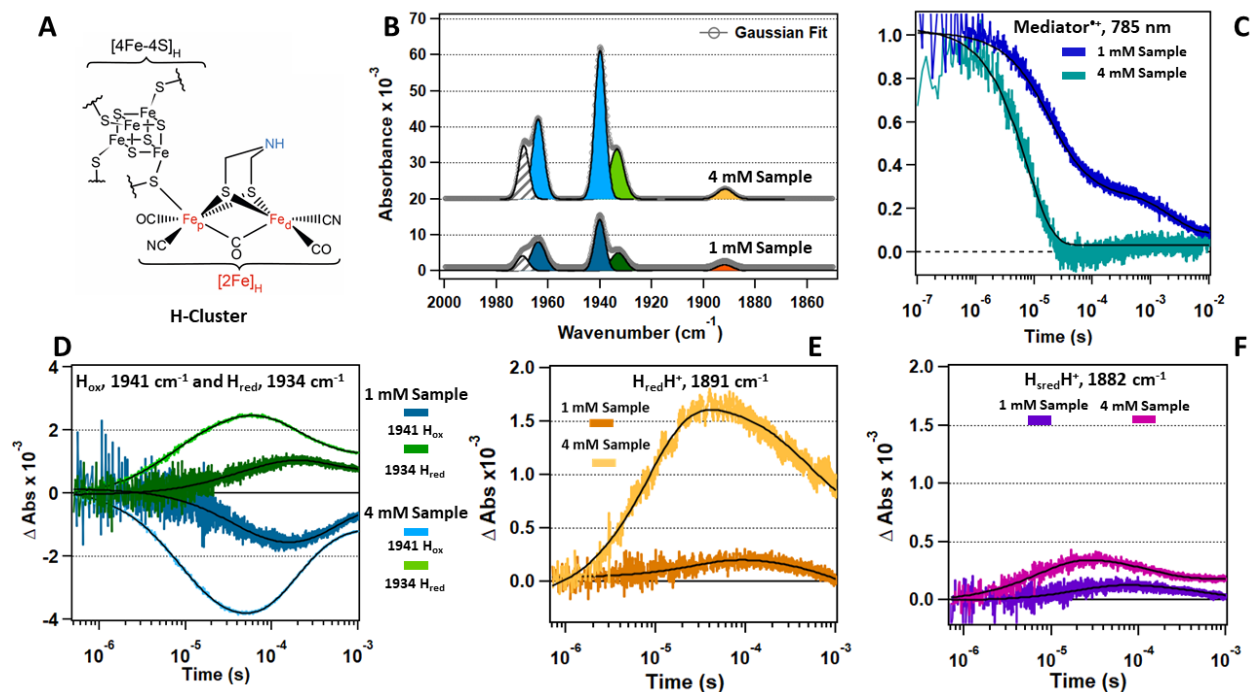


Figure 4.6 Time-resolved Visible (TR-Vis) and IR (TR-IR) measurements with samples containing 1 mM and 4 mM CrHydA1 at pH 7.4 in the presence of CdSe/CdS DIR and 25 mM DQ03. A) Diagram of the active site (H-cluster) of CrHydA1 [FeFe] Hydrogenase. B) FTIR of both 1 mM and 4 mM CrHydA1 containing samples used for transient absorbance measurements. The 4 mM sample has been offset for clarity. C) TR-Vis traces of DQ03 at 785 nm for 1 mM sample (blue) and the 4 mM sample (turquoise). D) TR-IR traces of CrHydA1 in the Hox (1941 cm⁻¹, blue) and Hred (1934 cm⁻¹, green) states in 1 mM enzyme samples (dark color) and 4 mM enzyme samples (light color). E) TR-IR traces of the HredH⁺ state (1891 cm⁻¹) in samples 1 mM (orange) and 4 mM (yellow). F) TR-IR traces of the HsredH⁺ state (1882 cm⁻¹) in 1 mM samples (purple) and 4 mM samples (magenta).

Under mildly oxidizing conditions (in the absence of H₂), the H-cluster is in the active oxidized state H_{ox} with the most intense IR band at ≈ 1941 cm⁻¹. One electron reduction yields two different reduced states, commonly called H_{red} and H_{red}H⁺. H_{red} is thought to have most of the extra electron density located on the [4Fe-4S] cluster site, resulting in only small (5-10 cm⁻¹) red-shifts to the IR bands. Hence, the most intense IR band of the H_{red} state is observed at ≈ 1934 cm⁻¹. The H_{red}H⁺ state is thought to have the electron density shifted more onto the [2Fe] site giving much larger (20-60 cm⁻¹) shifts in the IR bands. The most intense peak for H_{red}H⁺ is, therefore, observed at 1891 cm⁻¹. Finally, one electron reduction of the [4Fe-4S] cluster in the H_{red}H⁺ state gives the H_{sred}H⁺ state with a major band at 1882 cm⁻¹. Here, we followed the transition from H_{ox} to H_{red} and H_{red}H⁺ as well as the transition to form H_{sred}H⁺ in *CrHydA1*.

The rates of depletion and formation of the H_{ox} and H_{red} intermediate populations were calculated from the values obtained by fitting the transient data to a sum of exponential functions (details and final fitting coefficients are summarized in the supplemental information). The bleach of H_{ox} feature at 1941 cm⁻¹ (Fig 4.6D) corresponds with the one electron reduction of the H-cluster to give H_{red} and H_{red}H⁺. Both the 1 mM and 4 mM *CrHydA1* containing samples featured bi-exponential decays of their H_{ox} populations. For instance, the 1 mM sample had H_{ox} decay rates of 28 and 90 μ s while the 4 mM sample had H_{ox} decay rates of 7 and 35 μ s. Similar biexponential reduction of *CrHydA1* has been observed before and was attributed to two different pathways through the protein for ET to the active site.²⁰ This interpretation is further supported by the biexponential rate of formation of the H_{red} intermediate (Fig. 4.6D). Both the 1 mM and 4 mM samples feature two formation constants that closely match the two decay lifetimes of the H_{ox} population, 20 and 94 μ s for the 1 mM sample and 5 and 24 μ s for the 4 mM sample. The biexponential behavior is not observed with the formation of H_{red}H⁺ (Fig. 5E)

intermediates however, though its formation also matched the faster rate of H_{ox} decay with lifetimes of 29 and 9 μs for the 1 and 4 mM samples, respectively. Interestingly, very little formation of the 2-electron intermediate, $H_{sred}H^+$, was observed in these experiments, suggesting that, even at the lower enzyme concentration, predominantly a single electron transfer to the enzyme occurs. Production of a small population of $H_{sred}H^+$ monitored at 1882 cm^{-1} (Fig. 4.6F), is likely the result of one electron reduction of the H_{red} population that is present at the beginning of the experiment (Fig. 4.6B). Its formation rate (8 μs) is similar to the rate of formation of the 1-electron intermediates, H_{red} and $H_{red}H^+$. Since the H_{red} and $H_{red}H^+$ states form on very similar timescales, proton transfer to the H-cluster must be on the same timescale or faster than electron transfer from the mediator to the enzyme.

4.4 Utilization of 532 nm light for Excitation with CdSe NRs

Previously, CdSe/CdS dot-in-rod nanorods (NRs) were the photosensitizer of choice in not only our group but in other light driven studies^{44-45, 18, 21} due to all the features previously listed, i.e. high extinction coefficient, long lived exciton, and stability. Also as previously noted the excitation source for these particles is usually in the UV or near UV, typically either 355 nm or 405 nm light. However, some catalysts and proteins which might benefit from a light driven study using photosensitizer and mediator, have a demonstrated sensitivity to near UV light. Because of this sensitivity, we determined there was a need for a material which can be excited at lower energy wavelengths, such as in the visible rather than the near-UV, 355 nm. By making simple modifications to the CdSe quantum dot core normally used to seed the growth of our CdSe/CdS NRs, we explored the use of CdSe NRs as our photosensitizer. CdSe NRs of sufficient

size and morphology have a band edge that is red shifted relative to the CdSe/CdS NRs (Figure 4.7) and so are strong absorbers in the visible.

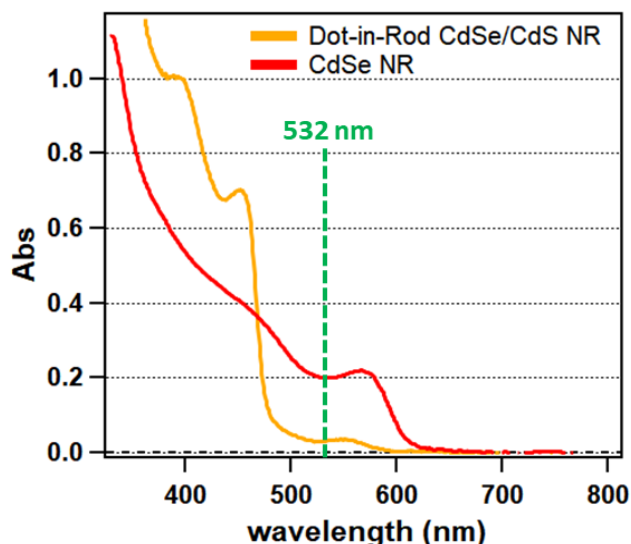


Figure 4.7 UV-Vis absorbance spectra comparing band edge shift of CdSe NRs (red) relative to Dot-in-Rod CdSe/CdS NRs (gold). The excitation wavelength, 532 nm is highlighted with the green dashed line.

One important drawback with using a 355 nm excitation source is that protein bands frequently absorb strongly at this wavelength. This has the potential to screen some needed photons from the photosensitizer and decrease overall efficiency. However, at 532 nm this screening effect is minimal and so the potential for this photosensitizer mediator method is maximized. Thus, by this relatively simple switch we can achieve large jumps, with minimal risk of damage to the sample.

4.4.1 Steady-state Photo-driven Mediator Reduction

In order to assess CdSe NRs as photosensitizers with our mediator system, steady-state photo-driven mediator reduction experiments were performed. These assays (Figure 4.8) were completed the same as with the CdSe/CdS NRs except using green light (532 nm) as the excitation source. It was found that these materials feature slightly lower QE, at ~ 50% efficiency, than what is observed with the CdSe/CdS NRs (near unity).^{18, 21}

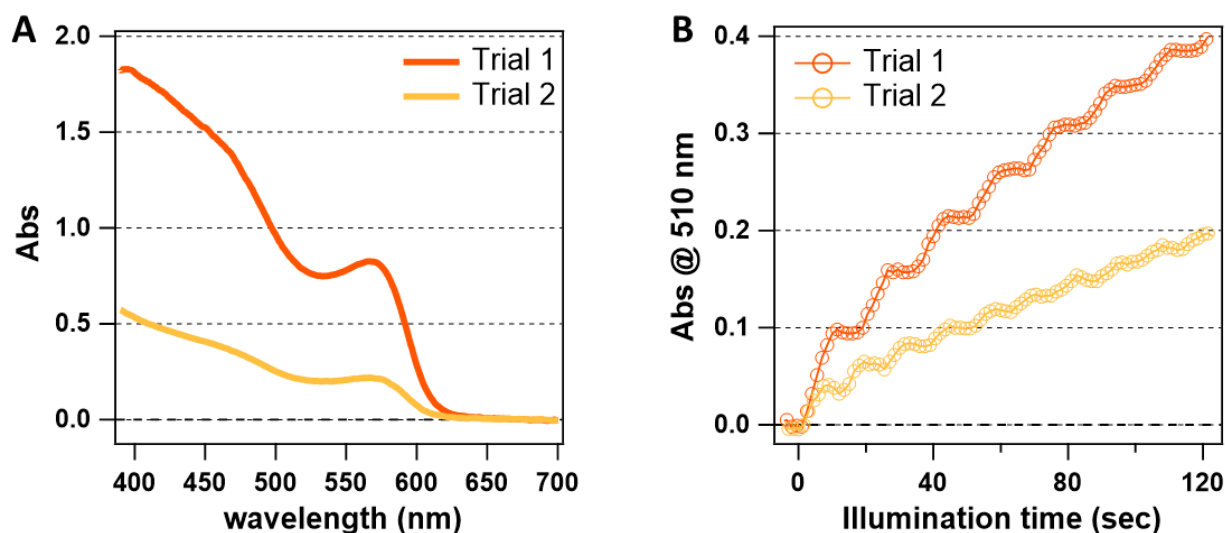


Figure 4.8. Steady-state photo-driven mediator reduction using CdSe NRs and 532 nm excitation light. A) UV-Vis absorbance spectra of initial sample. B) Plot of Abs @ 510 nm for each trial.

This discrepancy can be attributed to a higher degree of defects present on the surface of the rods.^{12, 46} In comparison to those materials which have a shell over the core provides two key benefits: the first is that utilizing a heterostructure allows for the physical separation of the electron hole pair.⁴⁷⁻⁵⁰ That is the hole becomes confined to the core while the electron can migrate to the surface of the shell.⁵¹ A hole that is confined can also be more efficiently quenched, a key to improving quantum efficiency and lengthening the exciton lifetime.⁵² This

allows the exciton pair to enjoy an extended excited state lifetime relative to a material which does not have this heterostructure. The second advantage of having a shell is that the annealing of the shell in the growth process fills in defects of the core surface. Defects on the surface of the material become problematic as they can trap electrons that have migrated to the surface of the material.^{35, 48, 52-54} The extended exciton lifetime and decrease in surface defects both work in conjunction to improve the overall efficiency of electron transfer from the material to the excited state electron quencher.^{53, 55-56}

The next step for the utilization of these particles in more potential jump studies might be optimizing the synthesis and core size and preparing particles which have a shell grown over the core. Such improvements might potentially bring the QE from ~50% closer to the near unity efficiency that is observed with the DIR particles used elsewhere.

4.4.2 Pump-Power Dependence with CdSe NRs

To characterize these materials as photosensitizers in a potential jump system in a pump-probe system, a pump power dependence study measuring the mediator radical generation was performed over a series of pump powers.

The results of this study show a nearly linear correlation between pump power and radical generation concentration for the pump powers measured, a useful characteristic for anticipating reducing equivalents generated with each pump. Extremely high radical concentrations (mM range) were also observed making this a very valuable tool for mechanistic studies in which multiple reducing equivalents are needed to initiate catalysis or observe multi-electron intermediates.

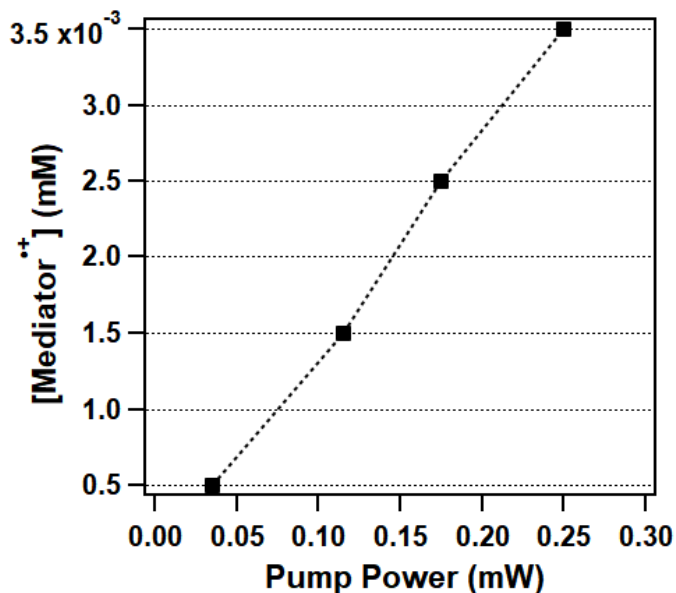


Figure 4.9 Pump power dependence of mediator radical generation in a potential jump sample composed of nanorods and mediator.

4.5 Conclusions

Previously, we established the viability of a method of shuttling electrons to a catalyst via viologen based mediators in the context of a mechanistic study of a specific enzyme (hydrogenase), though the general utility of the approach not yet been well established.^{18, 21} Also lacking from previous work was careful measurement of the timescale and magnitude of the laser induced potential jump, characteristics necessary to determine the applicability of this technique for study of other systems. In the work presented here, several parameters were screened to address these unresolved questions as well as to provide the framework for the application of this system for the study of other biocatalysts, including pH, mediator midpoint potential and concentration, photosensitizer concentration, protein concentration, and photon flux. An alternate material as a “new” photosensitizer was also explored for potential jump measurement application, CdSeNRs. CdSe NRs have multiple advantages as a photosensitizer, though the most compelling reason for their use is their strong absorbance at 532 nm.

In steady-state measurements, it was observed that the QE_{rad} of electron quenching by the mediator is quite sensitive to pH and mediator concentration. These observations are due to hole transfer effects and surface coverage by the mediator, respectively and indicate that careful tuning of these two conditions can maximize the quantum efficiency of photo-driven catalysis with oxidoreductases. When the CdSe NRs were utilized, the observed QE_{rad} for the photo-driven reduction of DQ03 was ~50% under the conditions observed making it a reasonable choice as photosensitizer.

In kinetics studies, it was found that the magnitude of the jump varied with sample conditions as observed in the steady-state experiments. The expected correlation between laser power and radical production allows tuning of the magnitude of the potential jump simply by

increasing the pump power. At the highest pump power tested, the solution potential was lowered by several hundred millivolts in response to the laser pulse. Despite having the poorest QE_{rad} in steady-state measurements, DQ43 produced the largest change in solution potential, achieving a final solution potential of -600 mV under one set of conditions. The change in solution potential is generated within the time of the laser pulse (10 ns in the present work), which is fast enough to observe flux through intermediate states of very fast catalysts like hydrogenase. In addition, the potential jump is sufficiently negative to permit the study previously of previously inaccessible catalytic events in enzymes such as CODH that require highly reducing conditions to drive catalysis. Also, the magnitude of the jumps achieved in the experiments presented here do not represent the upper limit of jumps attainable. Based on these results, even larger jumps could be expected by varying some of the conditions explored, such as using higher concentrations of photosensitizer. The ability to achieve a large potential jump allows for the exploration of both 1 and 2 ET processes and to compare their rates since multi-electron catalysts often require increasingly negative reduction potentials for subsequent reductions (i.e. the catalyst gets harder to reduce after the first ET).

The CdSe NRs were also assessed as photosensitizers in a potential jump experiment and were found to be a reasonable candidate for use in light driven mechanistic studies. Despite the lower QE_{rad} relative to that which is observed with CdSe/CdS DIRs, the amount of radical generated under potential jump conditions is sufficiently large (mM range) to make it a candidate for use in light driven mechanistic studies of not only hydrogenase but other systems which might be sensitive to UV excitation sources or require multiple reducing equivalents.

The lifetime of the potential jump is another important characteristic for establishing its applicability to fast enzyme reactions. The risetime of the potential jump in our experiments was

limited by the laser pulse width of 10 ns, although we have previously shown that ET from the photosensitizer to the mediator occurs on the picosecond timescale. Diffusion of the mediator and ET to the enzyme will clearly be rate limiting in most cases. The rate of ET to the hydrogenase enzyme was manipulated (increased or decreased) by altering the protein concentration. Increasing the concentration from 1 mM to 4 mM resulted in a doubling of the rate of radical consumption indicating this first ET step is at least partially diffusion-controlled. The persistence of the potential jump is limited by the phenomenon of pimer formation and disproportionation, which causes the radical population to decay on the millisecond timescale. Though not ideal, this decay does not hinder study of fast oxidoreductases, provided ET to the enzyme occurs before this decay on the ms timescale.

Finally, the optimum mediator for driving a specific enzyme reaction depends on both the midpoint potential of the enzyme and its turnover frequency. For example, when two different hydrogenases (one [NiFe] and the other [FeFe]) with approximately the same midpoint potentials are compared in the same photo-driven system, a significant difference in the optimum mediator for light-driven H₂ production becomes apparent. We have shown previously that [NiFe] SHI from *Pyrococcus furiosus* had the highest turnover rate when paired with the DQ53 mediator,²¹ and the rate of H₂ production decreased when the more negative redox mediator DQ43 was used. In contrast, the *CrHydA1* [FeFe] hydrogenase used in the present study performed best when paired with the most negative redox mediator, DQ43. We reasoned that this is due to the approximately 100 times slower turnover rate of [NiFe] hydrogenase relative to *CrHydA1*. The greater driving force of ET from the more negative mediator DQ43 accelerates parasitic charge recombination (CR), such that it becomes competitive with ET to the [NiFe] hydrogenase. The faster turnover rate of *CrHydA1* allows it to outcompete CR with DQ43, resulting in more

efficient overall performance. This example highlights the need for careful matching of the enzyme turnover frequency and the driving force of the ET from the mediator to the enzyme to maximize efficiency of this process.

Cumulatively, these results lay the foundation for the application and expansion of this technique to enable the study of other biocatalytic systems, such as CODH or nitrogenase. In principle, they also demonstrate the potential for the substitution of other mediators or photosensitizers to tailor this approach for the desired study.

4.6 References

1. Cai, R.; Minteer, S. D., Nitrogenase Bioelectrocatalysis: From Understanding Electron-Transfer Mechanisms to Energy Applications. *ACS Energy Letters* **2018**, *3* (11), 2736-2742.
2. Evans, R. M.; Siritanaratkul, B.; Megarity, C. F.; Pandey, K.; Esterle, T. F.; Badiani, S.; Armstrong, F. A., The value of enzymes in solar fuels research – efficient electrocatalysts through evolution. *Chemical Society Reviews* **2019**, *48* (7), 2039-2052.
3. Greene, B. L.; Schut, G. J.; Adams, M. W. W.; Dyer, R. B., Pre-Steady-State Kinetics of Catalytic Intermediates of an [FeFe]-Hydrogenase. *ACS Catalysis* **2017**, *7* (3), 2145-2150.
4. Woolerton, T. W.; Sheard, S.; Chaudhary, Y. S.; Armstrong, F. A., Enzymes and bio-inspired electrocatalysts in solar fuel devices. *Energy & Environmental Science* **2012**, *5* (6), 7470-7490.
5. Banerjee, R.; Jones, J. C.; Lipscomb, J. D., Soluble Methane Monooxygenase. *Annual Review of Biochemistry* **2019**.
6. Wang, V. C. C.; Maji, S.; Chen, P. P. Y.; Lee, H. K.; Yu, S. S. F.; Chan, S. I., Alkane Oxidation: Methane Monooxygenases, Related Enzymes, and Their Biomimetics. *Chemical Reviews* **2017**, *117* (13), 8574-8621.
7. Sommer, C.; Adamska-Venkatesh, A.; Pawlak, K.; Birrell, J. A.; Rudiger, O.; Reijerse, E. J.; Lubitz, W., Proton Coupled Electronic Rearrangement within the H-Cluster as an Essential Step in the Catalytic Cycle of [FeFe] Hydrogenases. *J. Am. Chem. Soc.* **2017**, *139* (4), 1440-1443.
8. Rodríguez-Maciá, P.; Pawlak, K.; Rüdiger, O.; Reijerse, E. J.; Lubitz, W.; Birrell, J. A., Intercluster Redox Coupling Influences Protonation at the H-cluster in [FeFe] Hydrogenases. *Journal of the American Chemical Society* **2017**, *139* (42), 15122-15134.

9. Senger, M.; Mebs, S.; Duan, J.; Shulenina, O.; Laun, K.; Kertess, L.; Wittkamp, F.; Apfel, U.-P.; Happe, T.; Winkler, M.; Haumann, M.; Stripp, S. T., Protonation/reduction dynamics at the [4Fe-4S] cluster of the hydrogen-forming cofactor in [FeFe]-hydrogenases. *Physical Chemistry Chemical Physics* **2018**, *20* (5), 3128-3140.
10. Ratzloff, M. W.; Artz, J. H.; Mulder, D. W.; Collins, R. T.; Furtak, T. E.; King, P. W., CO-Bridged H-Cluster Intermediates in the Catalytic Mechanism of [FeFe]-Hydrogenase CaI. *J. Am. Chem. Soc.* **2018**, *140* (24), 7623-7628.
11. Brown, K. A.; Harris, D. F.; Wilker, M. B.; Rasmussen, A.; Khadka, N.; Hamby, H.; Keable, S.; Dukovic, G.; Peters, J. W.; Seefeldt, L. C.; King, P. W., Light-driven dinitrogen reduction catalyzed by a CdS:nitrogenase MoFe protein biohybrid. *Science* **2016**, *352* (6284), 448.
12. Brown, K. A.; Wilker, M. B.; Boehm, M.; Hamby, H.; Dukovic, G.; King, P. W., Photocatalytic Regeneration of Nicotinamide Cofactors by Quantum Dot–Enzyme Biohybrid Complexes. *ACS Catalysis* **2016**, *6* (4), 2201-2204.
13. Brown, K. A.; Dayal, S.; Ai, X.; Rumbles, G.; King, P. W., Controlled Assembly of Hydrogenase-CdTe Nanocrystal Hybrids for Solar Hydrogen Production. *Journal of the American Chemical Society* **2010**, *132* (28), 9672-9680.
14. Mulder, D. W.; Guo, Y. S.; Ratzloff, M. W.; King, P. W., Identification of a Catalytic Iron-Hydride at the H-Cluster of [FeFe]-Hydrogenase. *Journal of the American Chemical Society* **2017**, *139* (1), 83-86.
15. Utterback, J. K.; Wilker, M. B.; Mulder, D. W.; King, P. W.; Eaves, J. D.; Dukovic, G., Quantum Efficiency of Charge Transfer Competing against Nonexponential Processes: The Case

of Electron Transfer from CdS Nanorods to Hydrogenase. *J. Phys. Chem. C* **2019**, *123* (1), 886-896.

16. Wilker, M. B.; Shinopoulos, K. E.; Brown, K. A.; Mulder, D. W.; King, P. W.; Dukovic, G., Electron Transfer Kinetics in CdS Nanorod–[FeFe]-Hydrogenase Complexes and Implications for Photochemical H₂ Generation. *Journal of the American Chemical Society* **2014**, *136* (11), 4316-4324.

17. Brown, K. A.; Wilker, M. B.; Boehm, M.; Dukovic, G.; King, P. W., Characterization of Photochemical Processes for H₂ Production by CdS Nanorod–[FeFe] Hydrogenase Complexes. *Journal of the American Chemical Society* **2012**, *134* (12), 5627-5636.

18. Chica, B.; Wu, C.-H.; Liu, Y.; Adams, M. W. W.; Lian, T.; Dyer, R. B., Balancing electron transfer rate and driving force for efficient photocatalytic hydrogen production in CdSe/CdS nanorod–[NiFe] hydrogenase assemblies. *Energy & Environmental Science* **2017**, *10* (10), 2245-2255.

19. Greene, B. L.; Vansuch, G. E.; Chica, B. C.; Adams, M. W. W.; Dyer, R. B., Applications of Photogating and Time Resolved Spectroscopy to Mechanistic Studies of Hydrogenases. *Accounts of Chemical Research* **2017**, *50* (11), 2718-2726.

20. Sanchez, M. L. K.; Wu, C.-H.; Adams, M. W. W.; Dyer, R. B., Optimizing electron transfer from CdSe QDs to hydrogenase for photocatalytic H₂ production. *Chemical Communications* **2019**, *55* (39), 5579-5582.

21. Sanchez, M. L. K.; Sommer, C.; Reijerse, E.; Birrell, J. A.; Lubitz, W.; Dyer, R. B., Investigating the Kinetic Competency of CrHydA1 [FeFe] Hydrogenase Intermediate States via Time-Resolved Infrared Spectroscopy. *Journal of the American Chemical Society* **2019**, *141* (40), 16064-16070.

22. Zhao, F.; Li, Q.; Han, K.; Lian, T., Mechanism of Efficient Viologen Radical Generation by Ultrafast Electron Transfer from CdS Quantum Dots. *The Journal of Physical Chemistry C* **2018**, *122* (30), 17136-17142.
23. Greene, B. L.; Wu, C.-H.; Vansuch, G. E.; Adams, M. W. W.; Dyer, R. B., Proton Inventory and Dynamics in the Nia-S to Nia-C Transition of a [NiFe] Hydrogenase. *Biochemistry* **2016**, *55* (12), 1813-1825.
24. Greene, B. L.; Wu, C.-H.; McTernan, P. M.; Adams, M. W. W.; Dyer, R. B., Proton-Coupled Electron Transfer Dynamics in the Catalytic Mechanism of a [NiFe]-Hydrogenase. *Journal of the American Chemical Society* **2015**, *137* (13), 4558-4566.
25. Greene, B. L.; Joseph, C. A.; Maroney, M. J.; Dyer, R. B., Direct Evidence of Active-Site Reduction and Photodriven Catalysis in Sensitized Hydrogenase Assemblies. *Journal of the American Chemical Society* **2012**, *134* (27), 11108-11111.
26. Sickerman, N. S.; Hu, Y., Hydrogenases. *Methods Mol Biol* **2019**, *1876*, 65-88.
27. Wittkamp, F.; Senger, M.; Stripp, S. T.; Apfel, U. P., [FeFe]-Hydrogenases: recent developments and future perspectives. *Chemical Communications* **2018**, *54* (47), 5934-5942.
28. Lubitz, W.; Ogata, H.; Rüdiger, O.; Reijerse, E., Hydrogenases. *Chemical Reviews* **2014**, *114* (8), 4081-4148.
29. Xiao, Y.; Chu, L.; Sanakis, Y.; Liu, P., Revisiting the IspH Catalytic System in the Deoxyxylulose Phosphate Pathway: Achieving High Activity. *Journal of the American Chemical Society* **2009**, *131* (29), 9931-9933.
30. Kung, J. W.; Baumann, S.; von Bergen, M.; Müller, M.; Hagedoorn, P.-L.; Hagen, W. R.; Boll, M., Reversible Biological Birch Reduction at an Extremely Low Redox Potential. *Journal of the American Chemical Society* **2010**, *132* (28), 9850-9856.

31. Zhu, H.; Song, N.; Lv, H.; Hill, C. L.; Lian, T., Near Unity Quantum Yield of Light-Driven Redox Mediator Reduction and Efficient H₂ Generation Using Colloidal Nanorod Heterostructures. *Journal of the American Chemical Society* **2012**, *134* (28), 11701-11708.
32. Liang, Y.; Thorne, J. E.; Parkinson, B. A., Controlling the Electronic Coupling between CdSe Quantum Dots and Thiol Capping Ligands via pH and Ligand Selection. *Langmuir* **2012**, *28* (30), 11072-11077.
33. Kamat, P. V.; Jin, S., Semiconductor Photocatalysis: "Tell Us the Complete Story!". *ACS Energy Letters* **2018**, *3* (3), 622-623.
34. Song, N.; Zhu, H.; Jin, S.; Lian, T., Hole Transfer from Single Quantum Dots. *ACS Nano* **2011**, *5* (11), 8750-8759.
35. Wu, K.; Du, Y.; Tang, H.; Chen, Z.; Lian, T., Efficient Extraction of Trapped Holes from Colloidal CdS Nanorods. *Journal of the American Chemical Society* **2015**, *137* (32), 10224-10230.
36. Thompson, C. M.; Kodaimati, M.; Westmoreland, D.; Calzada, R.; Weiss, E. A., Electrostatic Control of Excitonic Energies and Dynamics in a CdS Quantum Dot through Reversible Protonation of Its Ligands. *The Journal of Physical Chemistry Letters* **2016**, *7* (19), 3954-3960.
37. Siebel, J. F.; Adamska-Venkatesh, A.; Weber, K.; Rumpel, S.; Reijerse, E.; Lubitz, W., Hybrid [FeFe]-Hydrogenases with Modified Active Sites Show Remarkable Residual Enzymatic Activity. *Biochemistry* **2015**, *54* (7), 1474-1483.
38. Brateman, P. S.; Song, J. I., Spectroelectrochemistry of aromatic ligands and their derivatives. 1. Reduction products of 4,4'-bipyridine, 2,2'-bipyridine, 2,2'-bipyrimidine, and some quaternized derivatives. *The Journal of Organic Chemistry* **1991**, *56* (15), 4678-4682.

39. Anderson, R. F.; Patel, K. B., Radical cations of some low-potential viologen compounds. Reduction potentials and electron-transfer reactions. *Journal of the Chemical Society, Faraday Transactions 1: Physical Chemistry in Condensed Phases* **1984**, 80 (10), 2693-2702.
40. Kertesz, M., Pancake Bonding: An Unusual Pi-Stacking Interaction. *Chemistry – A European Journal* **2019**, 25 (2), 400-416.
41. Suzuki, S.; Morita, Y.; Fukui, K.; Sato, K.; Shiomi, D.; Takui, T.; Nakasuji, K., Aromaticity on the Pancake-Bonded Dimer of Neutral Phenalenyl Radical as Studied by MS and NMR Spectroscopies and NICS Analysis. *Journal of the American Chemical Society* **2006**, 128 (8), 2530-2531.
42. Lü, J.-M.; Rosokha, S. V.; Kochi, J. K., Stable (Long-Bonded) Dimers via the Quantitative Self-Association of Different Cationic, Anionic, and Uncharged π -Radicals: Structures, Energetics, and Optical Transitions. *Journal of the American Chemical Society* **2003**, 125 (40), 12161-12171.
43. Geraskina, M. R.; Dutton, A. S.; Juetten, M. J.; Wood, S. A.; Winter, A. H., The Viologen Cation Radical Pimer: A Case of Dispersion-Driven Bonding. *Angewandte Chemie* **2017**, 129 (32), 9563-9567.
44. Kodaimati, M. S.; McClelland, K. P.; He, C.; Lian, S.; Jiang, Y.; Zhang, Z.; Weiss, E. A., Viewpoint: Challenges in Colloidal Photocatalysis and Some Strategies for Addressing Them. *Inorganic Chemistry* **2018**, 57 (7), 3659-3670.
45. Wu, K.; Hill, L. J.; Chen, J.; McBride, J. R.; Pavlopolous, N. G.; Richey, N. E.; Pyun, J.; Lian, T., Universal Length Dependence of Rod-to-Seed Exciton Localization Efficiency in Type I and Quasi-Type II CdSe@CdS Nanorods. *ACS Nano* **2015**, 9 (4), 4591-4599.

46. Cline, R. P.; Utterback, J. K.; Strong, S. E.; Dukovic, G.; Eaves, J. D., On the Nature of Trapped-Hole States in CdS Nanocrystals and the Mechanism of Their Diffusion. *The Journal of Physical Chemistry Letters* **2018**, *9* (12), 3532-3537.
47. Weiss, E. A., Designing the Surfaces of Semiconductor Quantum Dots for Colloidal Photocatalysis. *ACS Energy Letters* **2017**, *2* (5), 1005-1013.
48. Weiss, E. A., Controlling Interfacial Processes in Excitonic Nanoparticles. *The Journal of Physical Chemistry Letters* **2014**, *5* (2), 361-362.
49. Peterson, M. D.; Jensen, S. C.; Weinberg, D. J.; Weiss, E. A., Mechanisms for Adsorption of Methyl Viologen on CdS Quantum Dots. *ACS Nano* **2014**, *8* (3), 2826-2837.
50. Knowles, K. E.; McArthur, E. A.; Weiss, E. A., A Multi-Timescale Map of Radiative and Nonradiative Decay Pathways for Excitons in CdSe Quantum Dots. *ACS Nano* **2011**, *5* (3), 2026-2035.
51. Zhu, H.; Song, N.; Lian, T., Controlling Charge Separation and Recombination Rates in CdSe/ZnS Type I Core–Shell Quantum Dots by Shell Thicknesses. *Journal of the American Chemical Society* **2010**, *132* (42), 15038-15045.
52. Wu, K.; Chen, Z.; Lv, H.; Zhu, H.; Hill, C. L.; Lian, T., Hole Removal Rate Limits Photodriven H₂ Generation Efficiency in CdS-Pt and CdSe/CdS-Pt Semiconductor Nanorod–Metal Tip Heterostructures. *Journal of the American Chemical Society* **2014**, *136* (21), 7708-7716.
53. Knowles, K. E.; Peterson, M. D.; McPhail, M. R.; Weiss, E. A., Exciton Dissociation within Quantum Dot–Organic Complexes: Mechanisms, Use as a Probe of Interfacial Structure, and Applications. *The Journal of Physical Chemistry C* **2013**, *117* (20), 10229-10243.

54. Zhu, H.; Yang, Y.; Hyeon-Deuk, K.; Califano, M.; Song, N.; Wang, Y.; Zhang, W.; Prezhdo, O. V.; Lian, T., Auger-Assisted Electron Transfer from Photoexcited Semiconductor Quantum Dots. *Nano Letters* **2014**, *14* (3), 1263-1269.
55. Reiss, P.; Protière, M.; Li, L., Core/Shell Semiconductor Nanocrystals. *Small* **2009**, *5* (2), 154-168.
56. Smith, A. M.; Nie, S., Semiconductor Nanocrystals: Structure, Properties, and Band Gap Engineering. *Accounts of chemical research* **2010**, *43* (2), 190-200.

Chapter 5

Mechanistic Studies of [FeFe] Hydrogenase

Reproduced in part with permission from

Monica L. K. Sanchez,[†] Constanze Sommer,[‡] Edward Reijerse,[‡] James A. Birrell,^{‡*} Wolfgang

Lubitz,^{‡*} R. Brian Dyer^{†*} Investigating the Kinetic Competency of CrHydA1 [FeFe]

Hydrogenase Intermediate States via Time-resolved Infrared Spectroscopy. *Journal of the*

American Chemical Society **2019**, 141 (40), 16064-16070

copyright 2019 American Chemical Society

5.1 Abstract:

Hydrogenases are metalloenzymes that catalyze the reversible oxidation of H_2 . The [FeFe] hydrogenases are generally biased toward proton reduction and have high activities. Several different catalytic methods have been proposed for the [FeFe] enzymes based on the identification of intermediate states in equilibrium and steady state experiments. Here, we examine the kinetic competency of these intermediate states in the [FeFe] hydrogenase from *Chlamydomonas reinhardtii* (*CrHydA1*) and *Desulfovibrio desulfuricans* (*DdHydAB*), using a laser-induced potential jump and time-resolved IR (TRIR) spectroscopy. A nanocrystalline semiconductor employed as the photosensitizer and a redox mediator efficiently transfers electrons to the enzyme. A pulsed laser induces a potential jump, and TRIR spectroscopy is used to follow the population flux through each intermediate state. The results presented in this chapter clearly establish the kinetic competency of all intermediate populations examined: H_{ox} , H_{red} , $H_{red}H^+$, $H_{sred}H^+$, H_{hyd} . Additionally, a new short-lived intermediate species with a CO peak at 1896 cm^{-1} was identified. These results establish a kinetics framework for understanding the catalytic mechanism of [FeFe] hydrogenases.

Detailed mechanistic studies to better understand transitions between these intermediates have also been completed by utilizing a mutant variant of the *CrHydA1* enzyme. This mutant has allowed us to evaluate whether the first intermediate transition from H_{ox} to H_{red} is proton coupled or not. Other intermediate transitions were also studied by completing a series of potential jump studies at different pHs to determine which steps might be proton coupled and which are ET only with an [FeFe] hydrogenase from *Desulfovibrio desulfuricans* (*DdHydAB*).

5.2 Introduction

Hydrogenases catalyze the reversible cleave of H₂ with high turnover frequency and minimal overpotential, using earth abundant transition metals.¹⁻² These highly efficient enzymes have inspired chemists for decades in an effort both to understand their mechanisms and to reproduce their chemistry in biomimetic systems.³⁻¹⁰ [FeFe] hydrogenases are particularly interesting because of their high activity, especially in hydrogen production.^{1, 7, 11} For these reasons, numerous studies have probed the catalytic cycle of [FeFe] hydrogenases, including extensive pH-dependent FTIR spectroelectrochemical experiments.^{2, 11-14} These studies have led to the identification of a series of resting states of the H-cluster differing by one or two electrons, or one proton, or both.^{12, 15} Although it is tempting to align these states as intermediates in a catalytic cycle,^{12-13, 15-16} questions remain whether all of these states are on pathway and whether other short-lived intermediates are involved that cannot be stabilized as resting states. Furthermore, several different catalytic cycles have been proposed, involving distinct ET/PT intermediates, some involving stepwise ET/PT with variations in the ordering of the steps^{12-13, 15, 17} and others involving concerted PCET^{2, 11, 14, 16}. Therefore, a detailed kinetics investigation of each of the intermediate states proposed to be catalytically relevant is critical to building a comprehensive catalytic model of [FeFe] hydrogenases. Capturing these intermediate states kinetically has proven challenging, however, due to the very rapid turnover rate of [FeFe] hydrogenases.

In this study, we employ a laser-induced potential jump coupled with the time-resolved infrared (TRIR) spectroscopy to study the catalytic mechanism of the [FeFe] hydrogenase from *Chlamydomonas reinhardtii* (CrHydA1). This methodology was previously demonstrated to be

capable of following the time-dependent population of hydrogenase intermediates on sub-turnover time scales.¹⁸⁻¹⁹ Using this approach, we address the critical questions of which intermediates are kinetically competent to be part of the catalytic cycle and determine the flux through each state during turnover of *CrHydA1*. The results presented here provide a framework for addressing which intermediates are significantly populated as part of the catalytic cycle, by (a) identifying distinct transient spectroscopic signatures for all relevant intermediate states, such that the kinetics of each can be probed on sub-turnover time scales; (b) demonstrating the kinetic competency of all of these states; and (c) identifying the critical rate-determining step (RDS) of the catalytic cycle.

Because of the similarity between *CrHydA1* and *DdHydAB* [FeFe] H₂ase active sites, it is assumed that these two proteins have the same catalytic cycle.¹ That is each protein will exhibit flux through the same intermediate populations despite key structural differences.^{12, 17, 20-21} This assumption has come into question more frequently in recent years as it has been shown that some intermediates are favored more than others.^{15, 22} Another key consideration is whether some steps are proton coupled or not. Steady-state spectroelectrochemical results have indicated conflicting evidence as displayed in Fig 5.1. To investigate these questions, kinetic measurements of the aforementioned intermediates were made with the *DdHydAB* [FeFe] hydrogenase and compared to the results of the kinetics study with the *CrHydA1* variant. The pH dependence of intermediate transformations have been measured as well as the use of a mutant [FeFe] hydrogenase to investigate which steps of the catalytic cycle are proton limited or not.

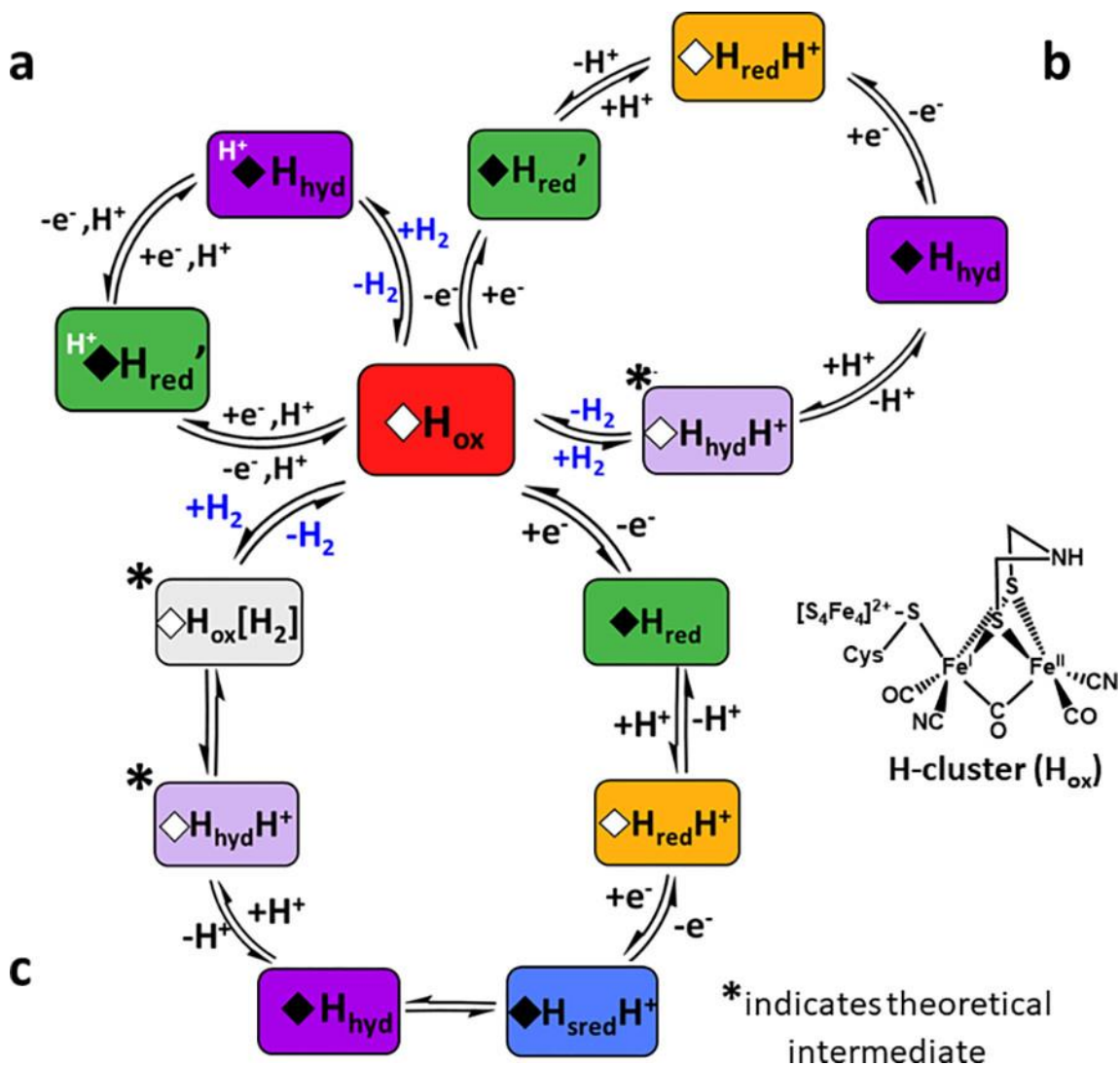


Figure 5.1 Scheme relating simplified versions of three recently proposed catalytic cycles for CrHydA1 [FeFe] hydrogenase. (a) Adapted from ref (16). (b) Adapted from ref (15) (simplified to show only main pathway for Cr). (c) Adapted from ref (17). \blacklozenge = $[\text{Fe}_4\text{S}_4]^{1+}$ cluster; \diamond = $[\text{Fe}_4\text{S}_4]^{2+}$ cluster. Colored rectangles indicate different H-cluster intermediate states identified in steady state measurements: Red = oxidized; green = 1 e^- reduced; yellow = 1 e^- and 1 H^+ ; blue = 2 e^- and 1 H^+ ; purple = hydride; light purple = hydride and 1 H^+ ; * = postulated intermediate. H_{hyd} and $\text{H}_{\text{hyd}}\text{H}^+$ labels refer to the same state and reflect literature variations in the nomenclature.

5.3 Investigating the Kinetic Competency of Proposed Intermediates

5.3.1 Rapid Initiation of Hydrogenase Turnover using a Potential Jump

In previous work, we established an approach to photo-initiate turnover of a hydrogenase using a photosensitizer and electron carrier to produce a potential jump on the sub-turnover time scale.^{19, 23-24} Here, we have applied this technique to study the mechanism of *CrHydA1* [FeFe] hydrogenase. All experiments were performed at pH = 8.4 because the rods are more stable and the yield of reduced mediator is optimized at this pH. We employed a nanocrystalline semiconductor CdSe/CdS dot-in-rod (DIR) as the photosensitizer and a propyl bridged 2,2'-bipyridinium (DQ03) as the electron carrier.²⁵⁻²⁶ Coupling this photo-triggering method with nanosecond time-resolved infrared (TRIR) spectroscopy yields a powerful tool to monitor the chemistry occurring at the active site.¹⁹ Upon pulsed laser excitation of the DIR photosensitizer, an electron is promoted to the conduction band, followed by ET to the mediator LUMO. This ET step occurs with near-unity quantum efficiency²⁷ and results in a rapid (~10 ns) potential jump as the solution potential becomes more negative by 400-500 millivolts, triggering turnover via ET to the enzyme.

The magnitude of the change in solution potential and the rate of ET to the enzyme were determined with visible transient absorption (TA) spectroscopy by monitoring the DQ03 chromophore. The reduced redox mediator, (DQ03 radical), has a strong and broad absorption band in the red spectral region whereas the oxidized mediator DQ03²⁺ does not absorb in this region.²⁷ Thus, the production of the reduced mediator and subsequent ET to the enzyme was monitored with TA probing at 785 nm and the change in solution potential is calculated using the Nernst equation. The relative time scales and energy levels of these ET events are depicted in the diagram in Figure 5.2B.

Two samples were compared, both containing the same concentrations of DQ03 and DIR but differing in whether they contained either *CrHydA1* or a reference protein, deoxyMb. The absorbance of the deoxyMb reference at 355 nm is matched to that of the hydrogenase sample to account for any inner filter effects of the protein absorbance. Representative 785 nm absorption transients for the *CrHydA1* deoxyMb samples are compared in Fig 5.2C. In both samples, the 785 nm absorption signal due to DQ03 radical formation rises with an instrument limited lifetime of <10 ns. The concentration of radical produced was between 400 and 500 μM on average depending on pump power. The rate of ultrafast reduction of DQ03^{2+} by the DIR photosensitizer has been well-established²⁷⁻²⁸ and agrees well with the results of this control experiment. The deoxyMb reference transient features a small amplitude single exponential decay of radical population with a lifetime of 16 μs . This initial decay is due to charge recombination, i.e. back electron transfer from the radical to the remaining hole in the DIR; this process is inefficient because it competes with hole quenching by the thiolate sacrificial electron donor. After this small initial decay, the TA signal remains constant out to tens of ms, indicating the stability of the reduced mediator in the absence of an electron acceptor. In contrast, a multiexponential decay of the 785 nm radical absorption is observed for the hydrogenase sample. Most of the decay (~65%) occurs in two initial phases with lifetimes of 16 and 61 μs , indicating that the bulk of the enzyme is reduced on this time scale. A slightly slower phase with a lifetime of 291 μs (25%) is also observed, meaning ~90% of the radical is consumed on a time scale faster than the turnover time (~2 ms) previously found for this enzyme.⁹ We also measured the steady state turnover rate of the enzyme under the potential jump conditions (pH 8.4, nanorod photosensitizer, mediator). Continuous illumination generates a steady state population of reduced mediator, which in turn causes steady state turnover of the enzyme. The steady state

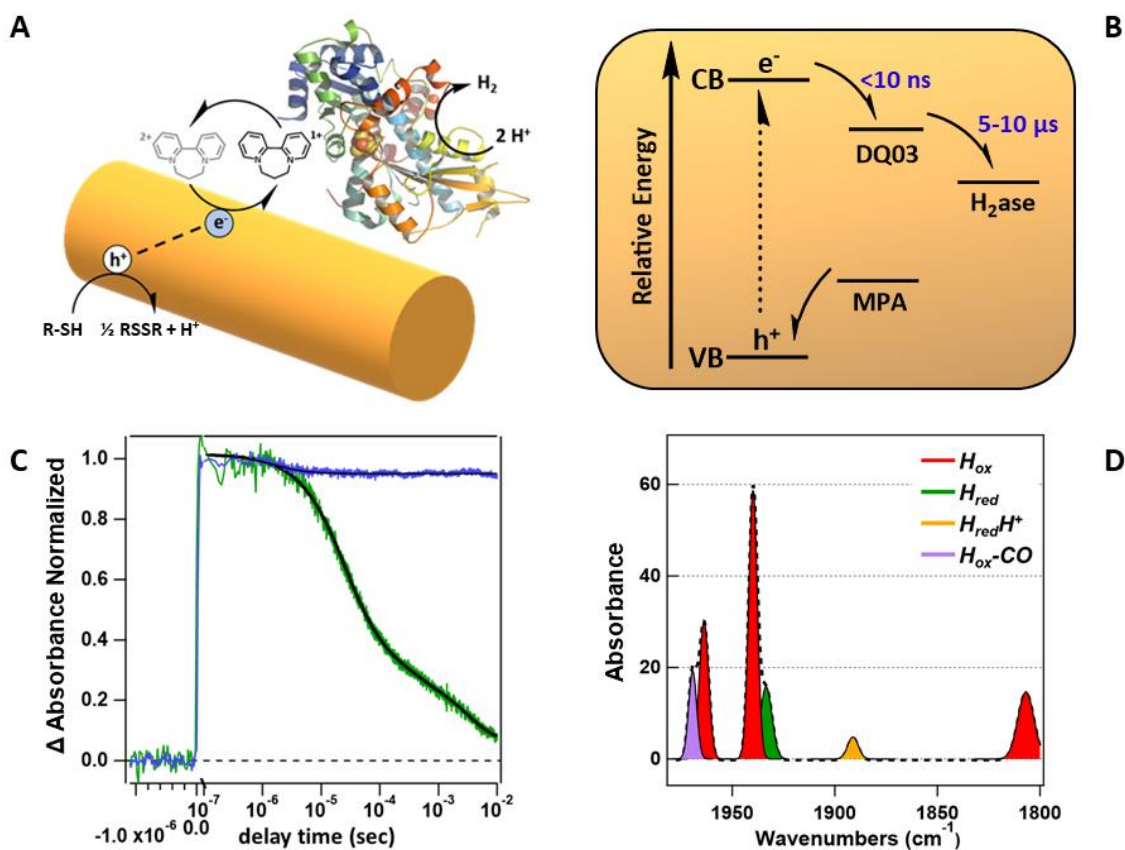


Figure 5.2. Laser-induced potential jump. (A) Electron transport pathway: light absorption generates exciton in CdSe/CdS nanorod, followed by reduction of DQ03 mediator and ET to CrHydA1 (crystal structure of apo-CrHydA1 adapted from ref (44), PDB 3LX4). (B) Energy diagram depicting the relative energy level and rates (ref (27)) of each ET step; MPA = mercaptopropionic acid, present as the DIR capping ligand and acting as the sacrificial electron donor; h^+ = hole remaining in the valence band (VB) of the material. (C) Potential jump monitored by transient absorbance (TA) of the radical at 785 nm for the HydA1 sample (green) compared to the deoxyMb (blue) reference. (D) Representative FTIR spectrum of the CrHydA1 sample used for laser-induced potential jump measurements. Intermediate populations are colored as follows: Mauve = $H_{ox}-CO$, Red = H_{ox} , Green = H_{red} , Gold = $H_{red}H^+$

rate we observe under these conditions (900 s^{-1}) is slightly faster than what was reported previously, but still consistent with the potential jump results.

Several groups have observed degradation of [FeFe] hydrogenase samples after some period of light exposure.²⁹⁻³⁰ The observed product of degraded protein is a CO inhibited H-cluster, termed $\text{H}_{\text{ox}}\text{-CO}$ has been well characterized and features an oxidized H-cluster with the additional CO bound in a terminal position on the distal Fe.³¹⁻³³ We tested the photostability of *CrHydA1* during the course of the experiments by measuring the FTIR spectrum before and after data collection. Based on the FTIR spectra collected, we consistently found <10% growth of the $\text{H}_{\text{ox}}\text{-CO}$ population under the conditions of our potential jump experiments. We attribute the photostability of the enzyme in these experiments to the high extinction coefficient of the CdSe/CdS nanorods ($>100,000 \text{ M}^{-1} \text{ cm}^{-1}$)³⁴ compared to that of the enzyme ($\sim 35,000 \text{ M}^{-1} \text{ cm}^{-1}$) at the pump wavelength. Apparently, the strongly absorbing rods protect the enzyme from light damage.

5.3.2 Photoprotection of the Enzyme by Photosensitizer

Potential jump experiments on the CO-inhibited enzyme provide further support for the photoprotection of the enzyme by the photosensitizer. They also demonstrate the importance of careful selection of the probe frequency to avoid overlapping absorbances of multiple species. For example, a probe frequency of 1954 cm^{-1} should report on both the $\text{H}_{\text{red}}\text{-CO}$ and the $\text{H}_{\text{sred}}\text{H}^+$ absorbance at 1882 cm^{-1} gives a very different transient response, corresponding to the slower conversion of $\text{H}_{\text{red}}\text{-CO}$ to $\text{H}_{\text{sred}}\text{H}^+$. The presence of any CO inhibited enzyme in the sample has the potential to obscure the detection of this and other catalytic intermediates. Therefore, we

selected probe frequencies corresponding to unique CO absorptions not overlapped with other states to follow the sub-turnover kinetics of intermediate states of the H-cluster.

We also conducted laser induced potential jump experiments on the CO inhibited enzyme under the same conditions as for the uninhibited enzyme, to determine whether if with a sample containing mostly CO-inhibited enzyme we might see some evidence of photolysis (Fig. 5.3A). However, no CO-photolysis was observed in these experiments, based on the previously established transient IR signatures for photolysis and rebinding of CO to the active site.³⁵ This finding supports our conclusion that the strongly absorbing CdSe/CdS DIR photo-protects the

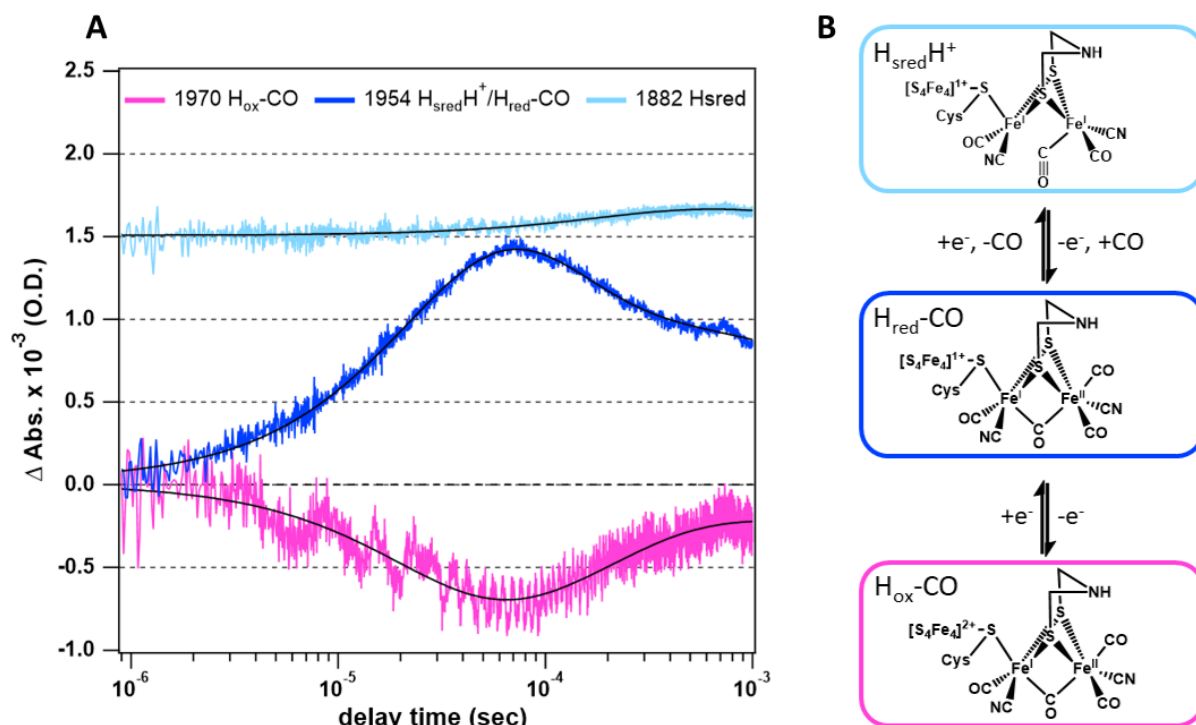


Figure 5.3 TRIR kinetics of CO-inhibited intermediate states. A) Proposed reaction scheme for reductive activation of CO inhibited H-cluster as it undergoes sequential ET steps and loss of CO to produce $H_{sred}H^+$. B) Kinetics traces collected at IR frequencies associated with each of these intermediates (1882 trace has been offset by 1.5 mOD for clarity).

enzyme and prevents CO-photolysis. And in fact, rather than photodegradation, we observed reactivation of the CO inhibited enzyme by the potential jump, which reduces the enzyme and releases CO, consistent with steady-state observations (Fig. 5.3B).^{13, 17} The initial decay of the H_{ox}-CO species monitored at 1970 cm⁻¹ ($\tau = 20 \mu\text{s}$) corresponds in time with the rise of the H_{red}-CO absorbance at 1954 cm⁻¹. The subsequent decay of the H_{red}-CO absorbance ($\tau = 290 \mu\text{s}$) coincides well with the rise of the of an absorbance at 1882 cm⁻¹, assigned to H_{sred}H⁺. These results support the previously proposed pathway for reactivation of CO inhibited enzyme: H_{ox}-CO \rightarrow H_{red}-CO \rightarrow H_{sred}H⁺.

We also found that two of the CO peaks associated with H_{sred}H⁺ (1882 and 1954 cm⁻¹) featured significantly different kinetics. The TRIR data measured at 1954 cm⁻¹ are almost identical to those collected at a wavenumber associated with H_{red}-CO (1967 cm⁻¹) and have no similar characteristics to those measured at 1882 cm⁻¹, a frequency identified as exclusively belonging to H_{sred}H⁺. Comparison of the lifetimes derived from multi exponential fits leads us to conclude that any activity measured at the 1954 cm⁻¹ region arise primarily from H_{red}-CO rather than H_{sred}H⁺, particularly when there is H_{ox}-CO present.

5.3.3 H-cluster Sub-turnover Kinetics at 8.4

The TA results indicate that *CrHydA1* is reduced on a subturnover time scale by the laser-induced potential jump. Consequently, all of the intermediate states of the H-cluster can be probed by TRIR spectroscopy on this time scale using their unique infrared signatures. Figure 5.4 shows frequency-dependent TRIR transients for *CrHydA1* following a laser-induced potential jump. Specific IR frequencies were selected to follow the kinetics of formation or loss of a specific intermediate state based on previous assignments of the IR spectra.¹² Only CO

frequencies were investigated because they give larger signals and better resolution for individual states compared to the CN^- bands. The enzyme sample as prepared was initially in a mixed oxidation state, with the majority being in H_{ox} , but also a significant population (~35%) of the one-electron reduced states H_{red} and $\text{H}_{\text{red}}\text{H}^+$. A sub-stoichiometric amount of a reduced mediator is produced by the potential jump (approximately a 1:5 ratio of reduced mediator to enzyme), meaning on average each enzyme receives less than a single electron. Consequently, the potential jump is insufficient to carry the population of enzyme that is initially in the oxidized state completely through the catalytic cycle, since this requires two electrons. Nevertheless, the potential jump results in complete cycling of some population of the enzyme, since some one-electron reduced enzyme is present initially. Thus, it is possible to track the population flux through all intermediate states in the potential jump experiment, although the resulting kinetics are complex.

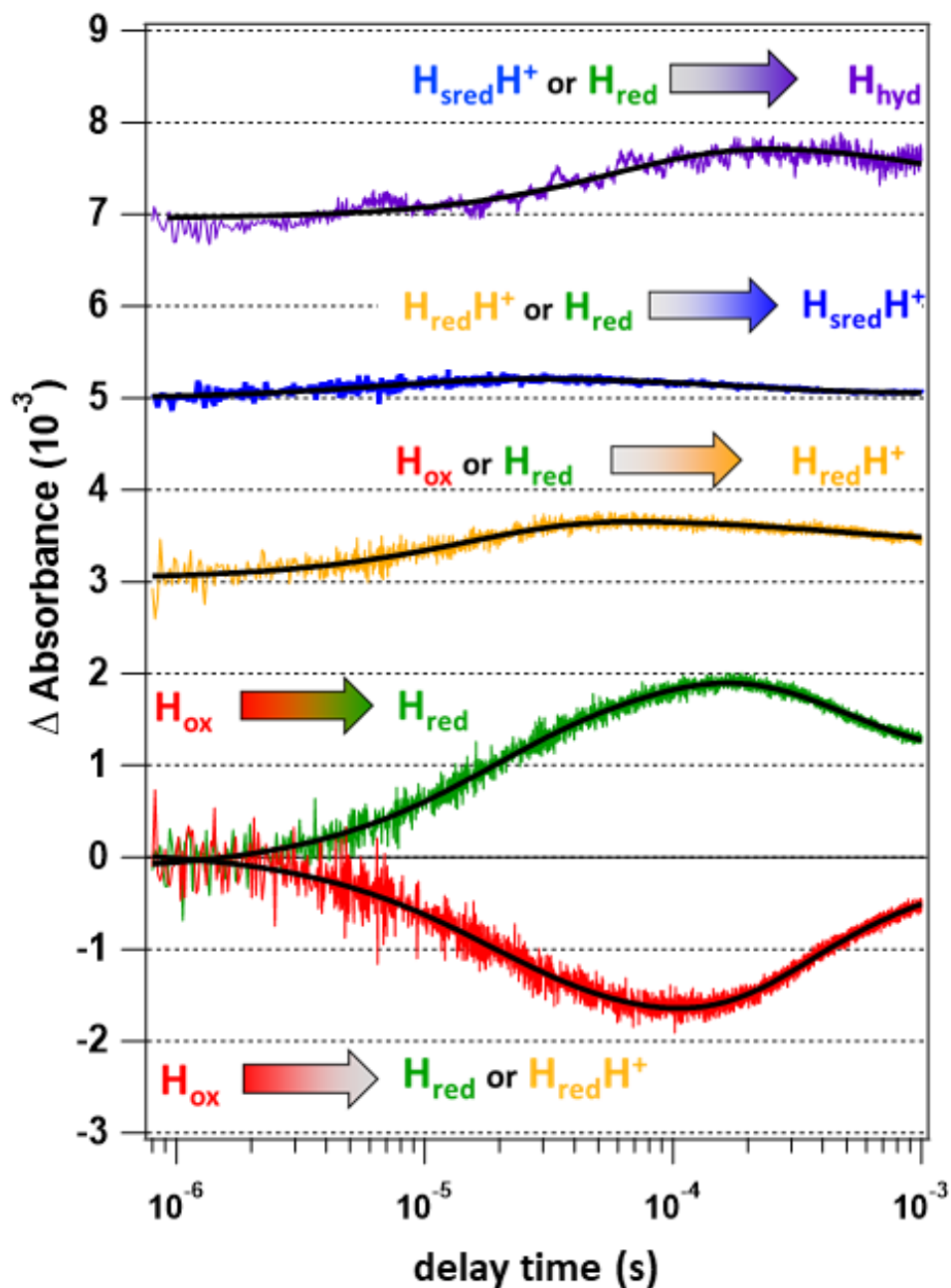


Figure 5.4. H-cluster kinetics. (Red) H_{ox} kinetics monitored at 1941 cm^{-1} ; (Green) H_{red} kinetics (1 e- reduced state) at 1934 cm^{-1} ; (Gold) $H_{red}H^+$ kinetics at 1891 cm^{-1} ; (Blue) $H_{sred}H^+$ kinetics (2 e- reduced state) at 1882 cm^{-1} ; (Purple) H_{hyd} kinetics at 1859 cm^{-1} . The indicated transitions correspond to the initial bleach or rise of each transient. The black lines represent multiexponential fits as described in the text.

H_{ox} Kinetics (1941 cm⁻¹). The rates of H_{ox} depletion and recovery establish the end points of the catalytic cycle: the bleach of the H_{ox} absorbance at 1941 cm⁻¹ corresponds to the initial one-electron reduction of the enzyme, starting the catalytic cycle, and the recovery of the bleach corresponds to the regeneration of H_{ox} at the end of the catalytic cycle. The bleach is modeled by a biexponential function with lifetimes of 14 μs (35%) and 75 μs (65%). These lifetimes are the same as those observed for the consumption of the reduced mediator DQ03 radical (16 and 61 μs) within the error of the measurement, meaning there is no observable delay between oxidation of the mediator and reduction of the H-cluster as expected for direct outer sphere ET from the mediator to the H-cluster. The two observed rates may be due to two different ET pathways into the enzyme. The native redox partner, photosynthetic electron transfer ferredoxin (PetF), forms a highly specific ET complex with CrHydA1, but this is not likely the case for the polypyridyl mediator employed here. Furthermore, there are no auxiliary FeS clusters that define a specific ET pathway in this hydrogenase, unlike for instance hydrogenases from *Desulfovibrio desulfuricans* or *Clostridium acetobutylicum*.^{1, 15-16, 21} Thus, it is not surprising that we observe multiple rates for reduction of H_{ox} by the mediator. At longer times, the recovery of the 1941 cm⁻¹ bleach corresponds to the turnover of the enzyme, which regenerates the H_{ox} state. A biexponential recovery is observed with lifetimes of 180 μs (65%) and 900 μs (35%). The 180 μs component is significantly faster than the turnover lifetime (900 s⁻¹ under the potential jump conditions or 1.1 ms lifetime), meaning it is likely to arise from some other process. We tentatively attribute this fast recovery of the H_{ox} population to disproportionation of H_{red} to yield H_{ox} and H_{sred}H⁺. The 900 μs component is slightly faster than what is predicted from the steady state turnover rate (1.1 ms). Apparently, the final chemical step that regenerates H_{ox} is not rate-

determining, meaning the steady state kinetics must be limited by some other process such as hydrogen diffusion out of the protein.

H_{red} Kinetics (1934 cm⁻¹). The production of H_{red} is monitored by the transient absorbance at 1934 cm⁻¹, which has two main components with lifetimes of 12 and 61 μs. The close correspondence of these lifetimes with those due to H_{ox} depletion is consistent with direct, one-electron reduction of H_{ox} to produce H_{red}. The H_{red} transient absorbance does not recover to baseline, because the potential jump generates a substoichiometric number of reducing equivalents and further progress through the cycle requires two electrons. The competing pathway of one-electron reduction of the initial population of H_{red} (presumably to form H_{sred}H⁺) should cause a decrease in the absorbance at 1934 cm⁻¹: such a decrease is observed at longer times, with a lifetime of 525 μs, well within the turnover lifetime. A faster phase of H_{red} reduction is likely present based on the observed fast formation of H_{sred}H⁺, but this phase is opposite in sign and therefore obscured by the rapid rise in H_{red} caused by reduction of H_{ox}. In summary, the observed reduction of H_{red} is significantly slower than H_{ox} but still within the lifetime of the catalytic cycle.

H_{red}H⁺ Kinetics (1891 cm⁻¹). A single exponential rise with a lifetime of 15 μs is observed at 1891 cm⁻¹, corresponding to a fast one-electron reduction of H_{ox} to produce H_{red}H⁺. The production of H_{red}H⁺ occurs with the same lifetime as the fast reduction of H_{ox}. These observations are consistent with a concerted ET/PT process that directly converts H_{ox} to H_{red}H⁺. It is not clear why the slower (75 μs) rate of reduction of H_{ox} does not have a corresponding rise in the H_{red}H⁺ transient. Since formation of H_{red} from H_{ox} is an ET process, whereas formation of H_{red}H⁺ involves PCET, their nearly identical formation rates means that the PT step that forms H_{red}H⁺ is fast and thus the ET and PCET processes are occurring in parallel, probably because a

pH 8.4 the proton donor for the PCET process is only partially protonated. The decay of 1891 cm^{-1} absorbance is observed with a lifetime of 540 μs . Some $\text{H}_{\text{red}}\text{H}^+$ is initially present in the sample, and its decay corresponds to a second one-electron reduction of the enzyme.

$\text{H}_{\text{sred}}\text{H}^+$ Kinetics (1882 cm^{-1}). This state is formed very rapidly, with a 7 μs rise and decays within 210 μs . The rapid rise of this state should have a corresponding depletion of the H_{red} or $\text{H}_{\text{red}}\text{H}^+$ state, but this is not observed, perhaps because it is obscured by rapid production of these states from H_{ox} , which is the dominant process in the potential jump with the present conditions. Nevertheless, it is clear this state is produced and decays well within the lifetime of the catalytic cycle.

H_{hyd} Kinetics (1859 cm^{-1}). The H_{hyd} state shows a fast rise with a lifetime of 60 μs and slow decay on the order of 1 ms. The formation lifetime of H_{hyd} is consistent with its origin being the $\text{H}_{\text{sred}}\text{H}^+$ state because the latter decays on a similar time scale to the H_{hyd} rise, although we cannot rule out direct conversion of H_{red} or $\text{H}_{\text{red}}\text{H}^+$ to H_{hyd} . Thus, the present results confirm that $\text{H}_{\text{sred}}\text{H}^+$, $\text{H}_{\text{red}}\text{H}^+$, H_{red} are each kinetically competent to form H_{hyd} . The decay of the H_{hyd} state is on the same scale as the recovery of the H_{ox} state and therefore corresponds to completion of the catalytic cycle. The 1859 cm^{-1} transient shows a small negative baseline offset at $t < \mu\text{s}$ due to imperfect subtraction of the temperature-dependent background absorbance of water. This baseline offset is easily distinguished from the protein signal due to its distinct time dependence (it rises on the nanoscale time scale of the instrument response), and it does not influence the fit of the protein signal.

5.3.4 TRIR Spectra Reveal a New Intermediate State

The kinetics experiments described above only probe intermediate states observed previously in equilibrium or steady state kinetics experiments. The question remains whether there are additional intermediates that have not been detected in steady state measurements due to their short lifetimes. For example, the protonation of H_{hyd} to form H_2 at the active site, presumably coordinated to the distal Fe, has never been observed. We searched for possible new intermediate states by measuring the complete time-resolved IR spectrum at subturnover times in the carbonyl stretching region ($1880\text{-}1958\text{ cm}^{-1}$), in response to a laser-induced potential jump. All known *CrHydA1* intermediate states have CO bands in this region, so this is a reasonable starting range to search.^{14, 16, 36} TRIR kinetics were measured from 100 ns to 10 ms stepwise at probe frequencies spaced by $1\text{-}2\text{ cm}^{-1}$ over this spectral range in order to generate TRIR spectra. Multiple (>10) IR transients were collected at each probe frequency and averaged. Figure 5.5A shows the IR transients collected at IR frequencies ($1891, 1893$ and 1895 cm^{-1}) near the CO band of the $H_{\text{red}}H^+$ intermediate. Time-resolved IR spectra are obtained as “time slices” through IR transients, by plotting the ΔA at a specific time-delay versus wavenumber (cm^{-1}) as shown in Figure 5.5C. The TRIR spectra are then fit to Gaussian line shapes with a global fitting procedure. Figure 5.5B compares the TRIR spectra at progressively longer delays to the steady-state FTIR difference spectrum obtained by subtracting the spectrum in the dark from a spectrum following continuous illumination to generate a steady-state population of reduced enzyme.

The TRIR spectra have some features in common with the steady-state FTIR difference spectrum, including the bleach at 1941 cm^{-1} corresponding to loss of H_{ox} (red) and positive features corresponding to formation of reduced active-site intermediates, H_{red} (green), $H_{\text{red}}H^+$ (yellow), and $H_{\text{sred}}H^+$ (blue), although with different relative amplitudes. There are additional

features in the TRIR spectra that are missing in the steady-state FTIR spectrum, highlighting the loss of information in steady state measurements of a dynamic system. The TRIR spectrum never quite converges to the steady-state one, even after 10 ms, likely because diffusion of H₂ out of the illuminated volume is slower than 10 ms. In contrast, on the >10 s time scale of the steady state measurement, the illuminated volume equilibrates with the surrounding solution by slow diffusion of H₂.

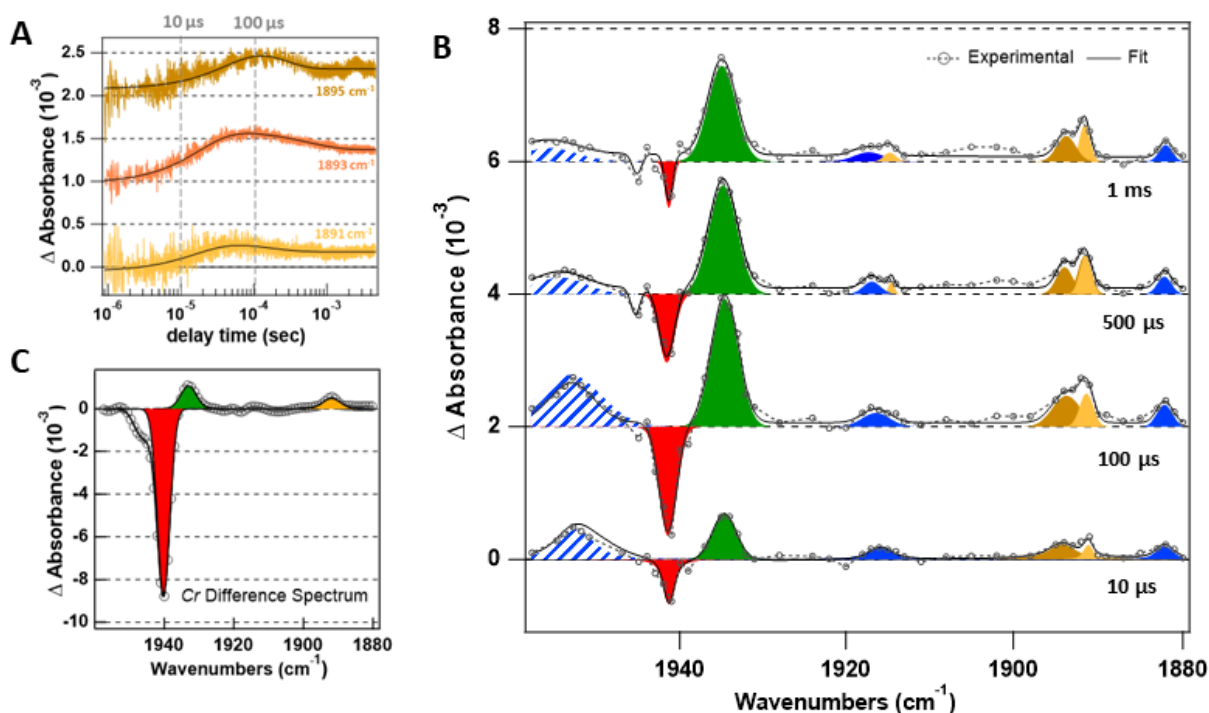


Figure 5.5 Potential jump TRIR spectra. (A) Potential jump IR transients at 1891, 1893, and 1895 cm⁻¹, offset for clarity. (B) TRIR spectra generated from IR transients, at time delays from 10 μs to 1 ms. The peaks are color coded as before; the blue shaded area >1950 cm⁻¹ is due to overlapping bands of H_{red}-CO and H_{sred}H⁺. (C) Steady-state difference FTIR spectrum of CrHydA1 in the presence of photosensitizer and mediator, generated by subtracting the spectrum in the dark from the spectrum after continuous illumination.

A new feature at 1896 cm^{-1} (brown) emerges from these TRIR spectra. This feature is in close proximity to the peak near 1891 cm^{-1} that has been assigned previously to the $\text{H}_{\text{red}}\text{H}^+$ intermediate.¹² The resulting broad transient feature in this region was best fit to two overlapping Gaussian peaks at 1891 and 1896 cm^{-1} . These two bands persist over hundreds of μs , but the ratio of amplitudes ($1896/1891$) decreases until $>1\text{ ms}$, where there are no longer two distinct populations. This observation is consistent with the transient nature of 1896 cm^{-1} band, whereas some population of the $\text{H}_{\text{red}}\text{H}^+$ state remains in the steady-state spectrum. The new feature fits to a rise time of $49\ \mu\text{s}$ and a decay time of $200\ \mu\text{s}$, distinct from the time response of the $\text{H}_{\text{red}}\text{H}^+$ absorbance at 1891 cm^{-1} as shown in Fig. 5.5A. The distinct time-dependence of these bands further supports the conclusion that they arise from distinct species. The kinetics of this feature, together with its unique CO frequency, are consistent with a new intermediate state.

5.3.5 Conclusions on the Kinetic Competency of Proposed Intermediate States

In this work, we have applied a laser-induced potential jump to initiate the catalytic cycle of the *C₇HydA1* [FeFe] hydrogenase on a much faster time scale than the steady state turnover. Concurrent TRIR and TA spectroscopies enable the measurement of time-dependent flux through all known intermediate states. In summary, several important aspects of the catalytic mechanism emerge from these kinetic measurements:

First, the rate of each one-electron reduction step is comparable to the rate of ET from the mediator to the enzyme. The interconversion rates between one-electron intermediate states induced by the potential jump do not appear to be proton limited at pH 8.4. Apparently, PT is fast enough to not be rate limiting, implying a rate of $\sim 10^{12}\text{ M}^{-1}\text{ s}^{-1}$ at pH 8.4, on the upper end of what has been observed in proteins.

All of the observed intermediates are kinetically competent to be part of the catalytic cycle. Their formation and decay rates are well within the previously determined turnover rate of the enzyme (TOF: 405 s⁻¹). Further work will be required to measure the pH-dependent flux through each state as the enzyme cycles, in order to establish the major (and possibly minor) pathway (s). nevertheless, it is difficult to reconcile the present results with simpler catalytic schemes (a and b) presented in Fig. 5.1, since we observe population flux through all of the major intermediate states as the enzyme turns over. For some intermediates we observe clear correlations between loss of one and gain of the other, indicating sequential transitions (H_{ox} → H_{red}). These observations are most consistent with mechanism c in Fig 5.1, although we cannot rule out the simpler mechanisms without pH- and isotope-dependent kinetics.

The rate-limiting step of catalysis is not the interconversion of any of the known intermediate states. We detect rapid intermolecular ET and production of H_{red}, H_{red}H⁺, H_{sred}H⁺, and H_{hyd} within 100 μs. The slowest step (reformation of H_{ox} at the end of the catalytic cycle) occurs with a lifetime of 900 μs and the disappearance of H_{hyd} has a similar lifetime, meaning the chemical steps of the catalytic cycle are complete within the turnover lifetime measured in steady state (~1.1 ms). It is reasonable to conclude that the rate-determining step of the steady state process is not any of the chemical steps but instead involves H₂ release from the protein.

A new intermediate state is observed with a CO frequency of 1896 cm⁻¹. While it is tempting to assign the new species to the H₂ bound state prior to reformation of the H_{ox} state, the CO frequency is very close to that of the H_{red}H⁺ state, suggesting it has a similar electronic structure, possibly a form with a slightly different structure around the H-cluster. Characterization of the complete spectrum of this intermediate (including the CN modes) and calculations will be necessary to assign it to a proposed structure.

In summary, this work represents the first detailed study of the sub-turnover kinetics of all of the known intermediate states of an [FeFe] hydrogenase. We have established the kinetic relevance of all non-CO inhibited intermediates, an important step toward the development of a comprehensive catalytic model for [FeFe] hydrogenases.

5.4 CrHydA1 Mechanistic Studies with the PDT mutant

One approach to mechanistic studies of [FeFe] hydrogenase is to use a variant of the wild type (WT) protein for unravelling some of the more detailed questions about the catalytic cycle of this enzyme.^{15, 37} Due to the ease of modification of the active site, a number of modifications have been made substituting atoms of different size, charge or electronic properties into the core site of catalysis (Fig. 5.6B).^{9, 14, 38-40} One of the most frequently studied active site variations is the PDT mutant, so named for the modified bridge head in which the azadithiolate bridge has been replaced with a propyldithiolate bridge.

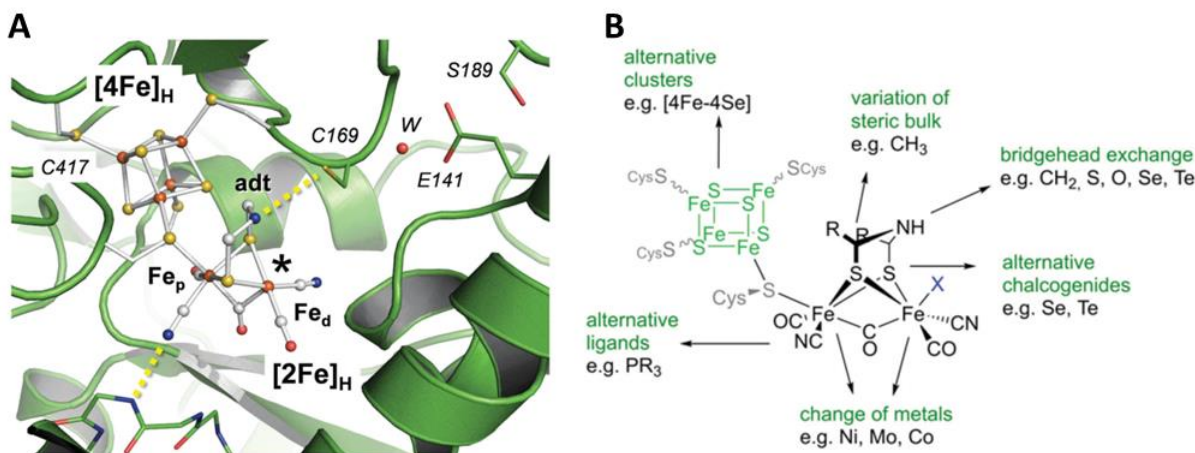


Figure 5.6 CrHydA1 active site structure and potential variations. A) Crystal structure of [FeFe]-hydrogenase from *C. pasteurianum* (*Cp*, PDB: 4XDZ) with an asterisk denoting an open coordination site on the distal iron atom (Fe_d). B) Pathways for possible alterations of the H-cluster of [FeFe] hydrogenases. *Figures A and B have been Reproduced from Ref. 11 with permission from The Royal Society of Chemistry.*

One mechanistic question which can be easily addressed with the use of the PDT mutant, is whether the first step in the catalytic cycle is proton coupled or not. It is generally accepted that the amine group of the azadithiolate bridge connecting both Fe atoms of the di iron core acts as a proton shuttle for the active site in the WT protein.^{22, 41} When the nitrogen atom of the pendant

amine is replaced with the unprotonatable group CH₂, this pendant group can no longer act as a proton shuttle and catalysis is effectively shut down, stopping the cycle at the first electron transfer step.^{14, 39} To date though, the FeFe hydrogenase community has yet to reach a consensus on whether this first step is indeed proton limited or purely ET due to conflicting literature reports. It has been demonstrated, with the PDT mutant, that the formation of the H_{red} intermediate state is a proton dependent transition leading the authors to conclude that, in the absence of the protonatable amine, forms by protonation of the nearby Fe₄S₄ cluster coordinated to the diiron core.^{39,14, 16, 39} These results conflict directly with reports which suggest that the first

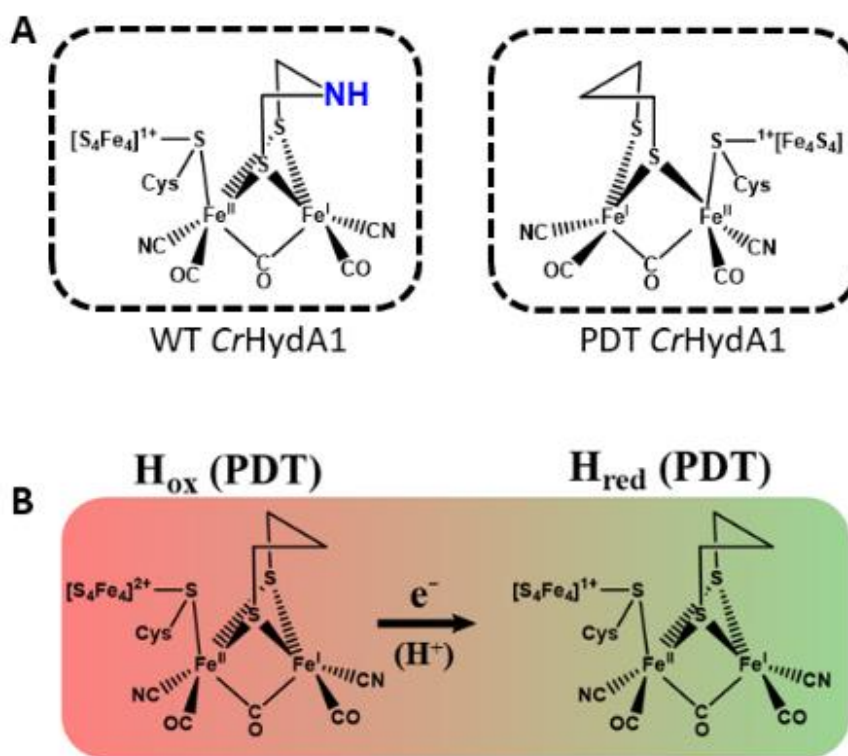


Figure 5.7 Comparison of the PDT mutant to the WT H-cluster and intermediate transformation involved. A) Cartoon of WT H-cluster vs. the PDT H-cluster. B) Intermediate transition observable using the PDT mutant.

ET step is not proton limited and that only the pendant amine serves as the protonatable site in the H-cluster.^{12, 17}

With the same PDT mutant, we sought to explore this relationship further by performing a potential jump experiment, using the same DIR/DQ03 pair that was used for the kinetic competence studies described in section 5.3 of this thesis. The advantage of using the PDT mutant rather than WT protein for this study is that the kinetics of this transition will be much simpler, as only the H_{ox} and H_{red} intermediate transitions will be observable. As demonstrated with the kinetic competency studies of section 5.3, seemingly simple transitions become complex due to the potential for other intermediates to form as an enzyme turns over.

By comparing the kinetics obtained from monitoring the H_{ox} and H_{red} intermediate states at different pHs, we can determine whether this first electron transfer step is proton limited or not. If it is the case that this first ET step is proton limited due to protonation of the Fe_4S_4 cluster, a clear difference in the rate of formation of the H_{red} intermediate dependent on the pH of the sample should be observed. If the formation of H_{red} is not proton limited, no difference in the observed rate of formation should be observed.

5.4.1 Light-titration experiments with the PDT mutant

Before we could proceed to kinetics measurements however, the distribution of intermediates observable under our conditions needed to be established. To accomplish this, we performed a light titration experiment in which we exposed the prepared samples to increasing amounts of light (355 nm) resulting in the reduction of the protein. Monitoring by FTIR gave us a detailed snapshot of the distribution of intermediate states observable under our conditions.

Two samples were prepared at pH 7.5 of *CrHydA1* hydrogenase, one containing the WT protein, the other the PDT mutant (Fig. 5.8A and 5.8C). To perform the light driven reduction experiment, both samples also contained nanorods, mediator and sacrificial electron donor as described previously.^{25, 27, 42}

In the WT sample (Fig. 5.8B), a dramatic decrease in the H_{ox} population at 1940 cm^{-1} is observed and is consistent with reduction of the active site via ET from the photosensitizer-mediator pathway. Interestingly, we do not see a concomitant rise in the H_{red} population that mirrors the decrease in the H_{ox} population. In the first 10 seconds of illumination, a slight increase in absorbance at the 1934 IR frequency is observed, however this induced absorbance is no longer observable by 20 seconds. The appearance of a population at 1954 cm^{-1} is consistent with the formation of the $H_{sred}H^+$ intermediate, except for the fact that positive features associated with the formation of this intermediate are not observed at the other frequency identified as belonging to $H_{sred}H^+$, 1881 or 1882 cm^{-1} .^{12, 17, 20, 43} Based on this observation, it seems more likely that the observed absorbance feature at 1954 cm^{-1} is related to the reduction of the population of $H_{ox}\text{-CO}$ present in the sample to form $H_{red}\text{-CO}$. It had been established previously that both $H_{sred}H^+$ and $H_{red}\text{-CO}$ have strongly overlapping bands in the region 1951 to 1955 cm^{-1} which is slightly dominated by the $H_{red}\text{-CO}$ intermediate.⁴² Based on this, it seems clear that this positive feature is actually evidence of the reduction of $H_{ox}\text{-CO}$ and not the $H_{sred}H^+$ intermediate. The other intermediate of interest is $H_{red}H^+$, which has absorbance features at 1915 cm^{-1} and 1891 cm^{-1} again based on previous steady-state measurements.^{12, 17} Very small

absorbances (less than 100 μOD) are observed at 1891 cm^{-1} indicating that perhaps this intermediate forms but is very short-lived.

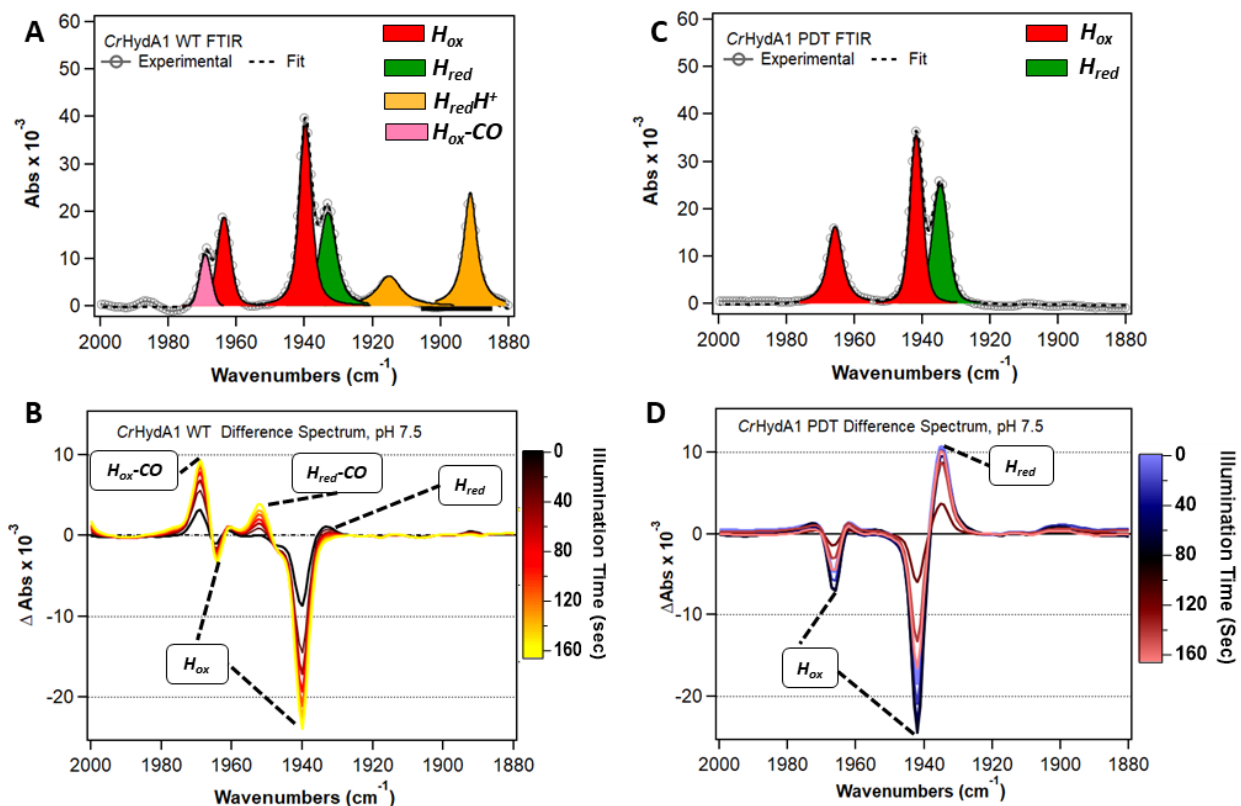


Figure 5.8 Photo-titration experiments with *CrHydA1* hydrogenase. A) Initial of WT *CrHydA1* sample. B) Initial FTIR of PDT *CrHydA1* sample. C) Results of photo-titration experiment monitored by FTIR of the WT *CrHydA1* sample. D) Results of photo-titration experiment monitored by FTIR of the PDT *CrHydA1* sample.

The observation that strong absorbances are not being observed for the H_{red} , $H_{\text{red}}H^+$ or $H_{\text{sred}}H^+$ intermediates does not indicate that these are not intermediates of interest. Rather, this observation is consistent with previous results suggesting that these are “on pathway” intermediates which should form and dissipate as the enzyme turns over. This conclusion is also consistent with results from section 5.3.4 of this thesis in which a “transient FTIR” is discussed. When these intermediates are observed on a rate relative to the rate of turnover, the distribution

of intermediates observed starkly contrasts with what is observable in the steady-state. All the aforementioned intermediates (H_{red} , $H_{\text{red}}H^+$ or $H_{\text{sred}}H^+$) are easily observable in the transient FTIR data but are unobservable in the steady-state under these conditions.

Compared to the WT photo-titration experiment, the observed changes in absorbance for the PDT sample are much simpler. The same significant bleach in the H_{ox} population is observed and is consistent with reduction of the active site. The most notable observable difference between the two experiments and their data sets is the significant formation of a population of H_{red} identifiable by the strong absorbance at the predicted IR frequency, 1935 cm^{-1} , whereas, in the WT sample a steady-state population of H_{red} is not observed. This result is expected and consistent with literature reports that the PDT mutant is essentially a short-circuited enzyme and “stops” at the H_{red} intermediate.

5.4.2 Kinetics Studies of the PDT Mutant under pH Conditions ranging from pH 6.5 to 10

With the intermediate distribution profile established, the kinetics for the H_{ox} and H_{red} intermediates were measured by monitoring 1942 and 1935 cm^{-1} respectively (Fig. 5.9). The same photo-initiation technique as with previous kinetics measurements was used, also using a 355 nm excitation wavelength.

Kinetics measurements were made with samples prepared at two different pHs to determine the extent, if any, of proton dependence there is in the H_{ox} to H_{red} intermediate transition. pH 6.5 and pH 10 were chosen as the pHs to explore with the intent that these should yield very different rates of formation of H_{red} if there is a proton dependence.

Monitoring at 1942 cm^{-1} for both the pH 6.5 and pH 10 samples shows a large and fast decay of the H_{ox} population with decay lifetimes of 26 and $29\text{ }\mu\text{s}$ respectively. Again, this is

consistent with reduction of the active site via electron transfer from the photosensitizer-mediator pathway. The rate is also similar to what has been observed with the WT protein, indicating that the lack of the pendant amine does not in any way inhibit ET to the H-cluster as expected.⁴² The disparity between the two rates is within the margin of error of the fit and so are essentially the same. Monitoring at 1935 cm^{-1} for the formation of the H_{red} intermediate state yields a similar observation. Again, a very fast increase in absorbance at the 1935 IR frequency occurs at very similar rates to the decay of H_{ox} . There is a slightly bigger difference between the two rates for the pH 6.5 and pH 10 sample (23 and 32 μs) but again this is within the margin of error of the fit and so are essentially identical. These results support the conclusion that the first ET step of the catalytic cycle of *CrHydA1* [FeFe] hydrogenase is not a proton limited step. Even though the concentration of protons in solution between the two samples are orders of magnitude different, the observed rates of formation are virtually identical. And even when compared to the kinetics measured for the WT variant little difference in rates is observed.

One unexpected observation that came out of this study is that the population of H_{red} seems to decay on longer timescales. In the pH 6.5 sample, this appears to be only a very slight decay in population. However, in the pH 10 sample, this decay is much more noticeable and seems to occur at a slightly earlier time than in the pH 6.5 sample. Concomitant with this is the slow recovery of the H_{ox} intermediate on the same timescale as the observed H_{red} population

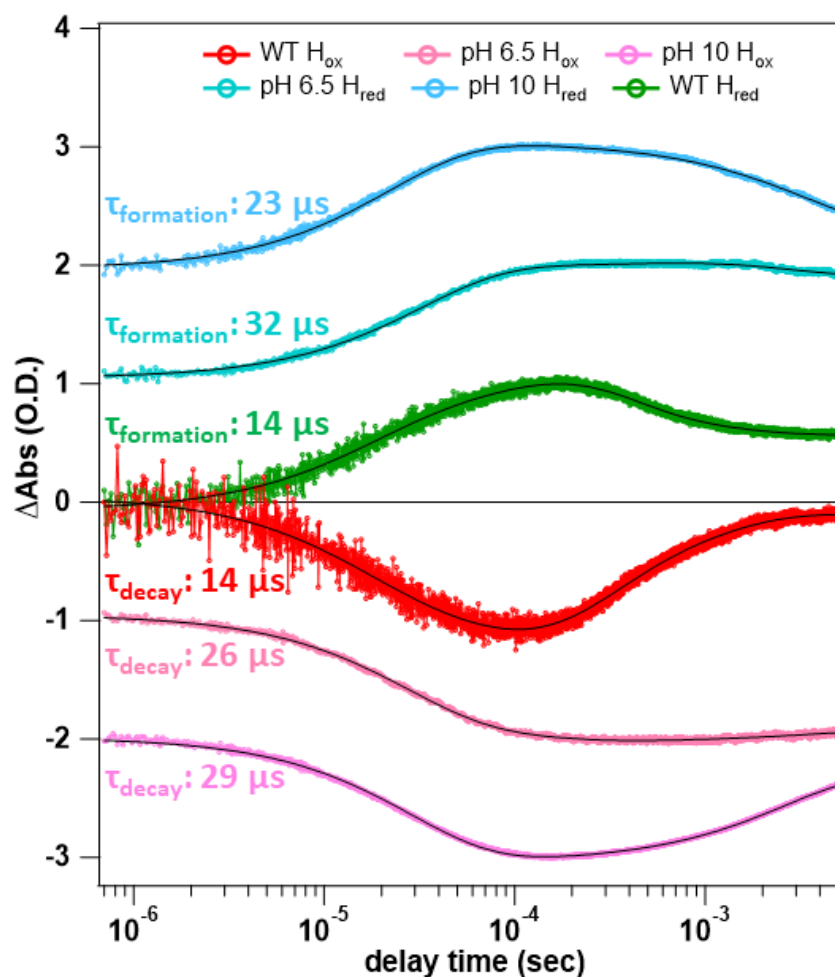


Figure 5.9 Kinetics of Hox and Hred intermediate populations of the PDT mutant, WT kinetics have been included for comparison. The coloring scheme is as follows: for the Hred intermediate, light blue = pH 10 sample; light turquoise = pH 6.5 sample and for the Hox intermediate, pink = pH 6.5 sample and light purple = pH 10 sample.

decay. This indicates, that over time the population of H_{red} is not a stable intermediate state at very alkaline pHs and that it either turns over very slowly (unlikely) or participates in some sort of disproportionation (more likely). The first scenario can be tested by monitoring other intermediate states for evidence of turnover. Other states must be populated if the enzyme is turning over so that H_2 can be released regenerating the H_{ox} intermediate. However, when other IR frequencies for other intermediate states were examined, evidence for this process could not be found. The more likely scenario is that the protein is undergoing disproportionation very slowly to form some $H_{\text{sred}}H^+$ intermediate and reform the H_{ox} intermediate. However, more investigation is needed to determine which of these are the most likely scenario.

5.5 *DdHydAB* Mechanistic Studies

Relative to the profligate body of work completed on the *CrHydA1* [FeFe] hydrogenase, considerably less work has been done to study *DdHydAB* [FeFe] hydrogenase. The H-cluster is quite similar to that of *CrHydA1*, the major difference between the two enzymes is the presence of two additional Fe_4S_4 , frequently referred to as the “F-clusters”, which form the ET pathway to the active site.⁴⁴ This seemingly minor difference has led to some interesting observations in the activity of the enzyme. Namely, that the rate of H_2 production and bias for proton reduction is much greater for the *DdHydAB* variant than it is to the *CrHydA1* enzyme.^{1, 20-21, 45} Based on our own experimental results, monitoring the rate of consumption of reduced mediator for each protein, we note that the *DdHydAB* variant consistently consumes the radical population faster than the *CrHydA1* variant (Fig. 5.10B). We suspect, this is likely due to the additional F-clusters

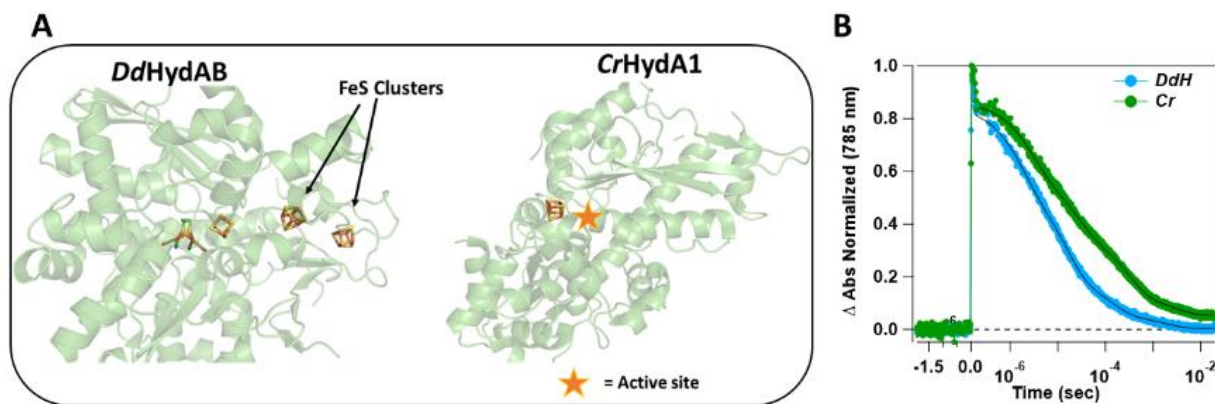


Figure 5.10 Comparison of enzyme structure between two [FeFe] hydrogenases. An [FeFe] hydrogenase from *Desulfovibrio desulfuricans*, *DdHydAB* (left). And an [FeFe] hydrogenase from *Chlamydomonas reinhardtii* *CrHydA1* (right). *DdHydAB* PDB: 1HFE (ref 44) and *CrHydA1*, PDB:3LX4 (ref 44). B) Normalized TR Vis kinetics from one potential jump experiment for *DdHydAB* (light blue) sample compared to one set for *CrHydA1* (green).

which can serve as electron reservoirs for the active site, however more studies would be needed to fully rationalize the observed results.

5.5.1 pH Dependence of Intermediate State Transitions

Understanding which transitions between intermediate states is integral to develop a complete kinetic model of the catalytic mechanism of [FeFe] hydrogenase. Though several examples of studies which seek to characterize these intermediates under a variety of conditions, including examining their relationship with pH, a comprehensive kinetics study of these intermediates under varied conditions has yet to be completed. To accomplish this, we measured kinetics for several intermediate states considered to be catalytically relevant based on several spectroelectrochemical and kinetics measurements.^{12, 21, 42} We measured the kinetics for H_{red} ,

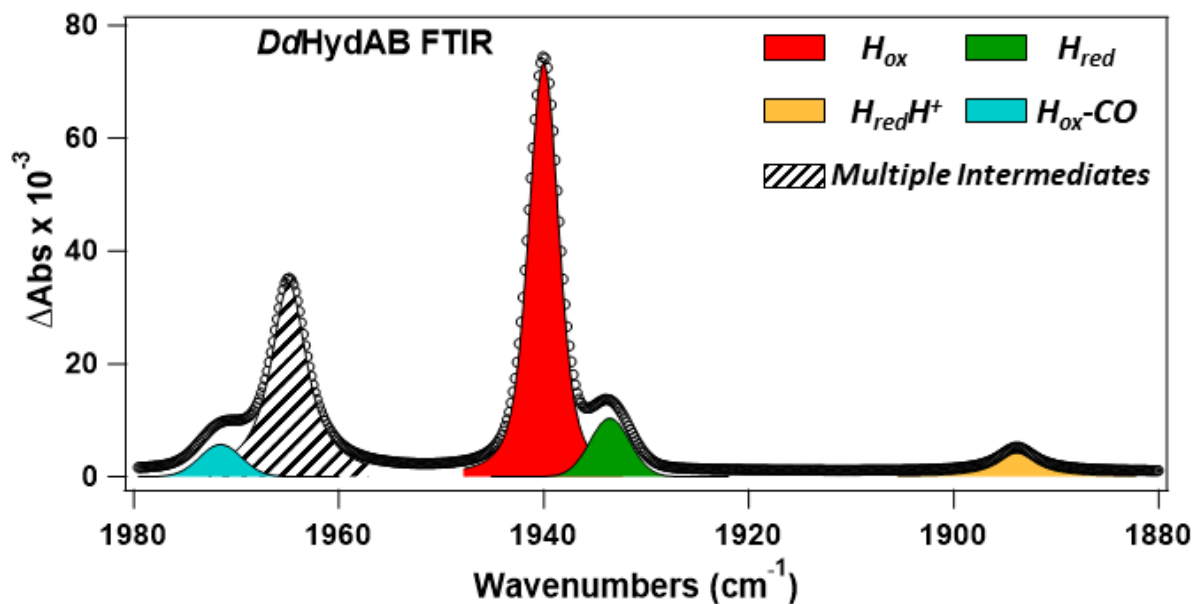


Figure 5.11 FTIR of *DdHydAB*. A) Representative FTIR of *DdHydAB* samples used in potential jump measurements. The color scheme is as follows: red = H_{ox} ; green = H_{red} ; yellow = $H_{red}H^+$; light blue = H_{ox-CO} and striped = multiple overlapping intermediates.

$H_{\text{red}}H^+$, $H_{\text{sred}}H^+$, and H_{hyd} in the *DdHydAB* enzyme with samples prepared at three different pHs: 6.5, 7.1 and 9.1. These pHs were chosen to elucidate the relationship between pH and the rate of formation and decay of each population. The results of these measurements are summarized below.

H_{red} (1934 cm^{-1}) The H_{red} intermediate has been characterized as having an oxidized active site with a 1-electron reduced Fe_4S_4 cluster.²²⁻²³ When monitoring at 1934 cm^{-1} in the pH 6.5 sample no kinetics were observed. However, in the pH 7.1 sample a small population forms and decays with lifetimes of 8 μs and 400 μs respectively. The amplitude of this population grows much larger for the pH 9.1 sample and the rate for the decay of this population is considerably slower than what was observed for the pH 7.5 sample. Overall, these results indicate that H_{red} is likely a transitional intermediate and not a resting state for the enzyme. At a pH where protons are not limited (pH 6.5) no net growth of population is observed likely because as soon as the 1-electron reduced state is formed, protonation of the H-cluster occurs and so the H_{red} intermediate population decays.

For the samples in which a monitorable population of H_{red} forms (pH 7.1 and 9.1), the rate at which they form does not vary with pH. This is consistent with an ET only step to form this intermediate. The formation constants for pH 7.1 and pH 9.1 are very similar, 8 μs and 16 μs respectively. The slight difference can be attributed to slight differences in the concentration of radical generated triggering formation by ET. Also quite clear, is the proton limited decay of the H_{red} population. This fits well with a catalytic model proposed by Lubitz et al, (Fig. 5.1)²¹ in which after H_{red} forms, the next step is protonation of the H-cluster to form $H_{\text{red}}H^+$.

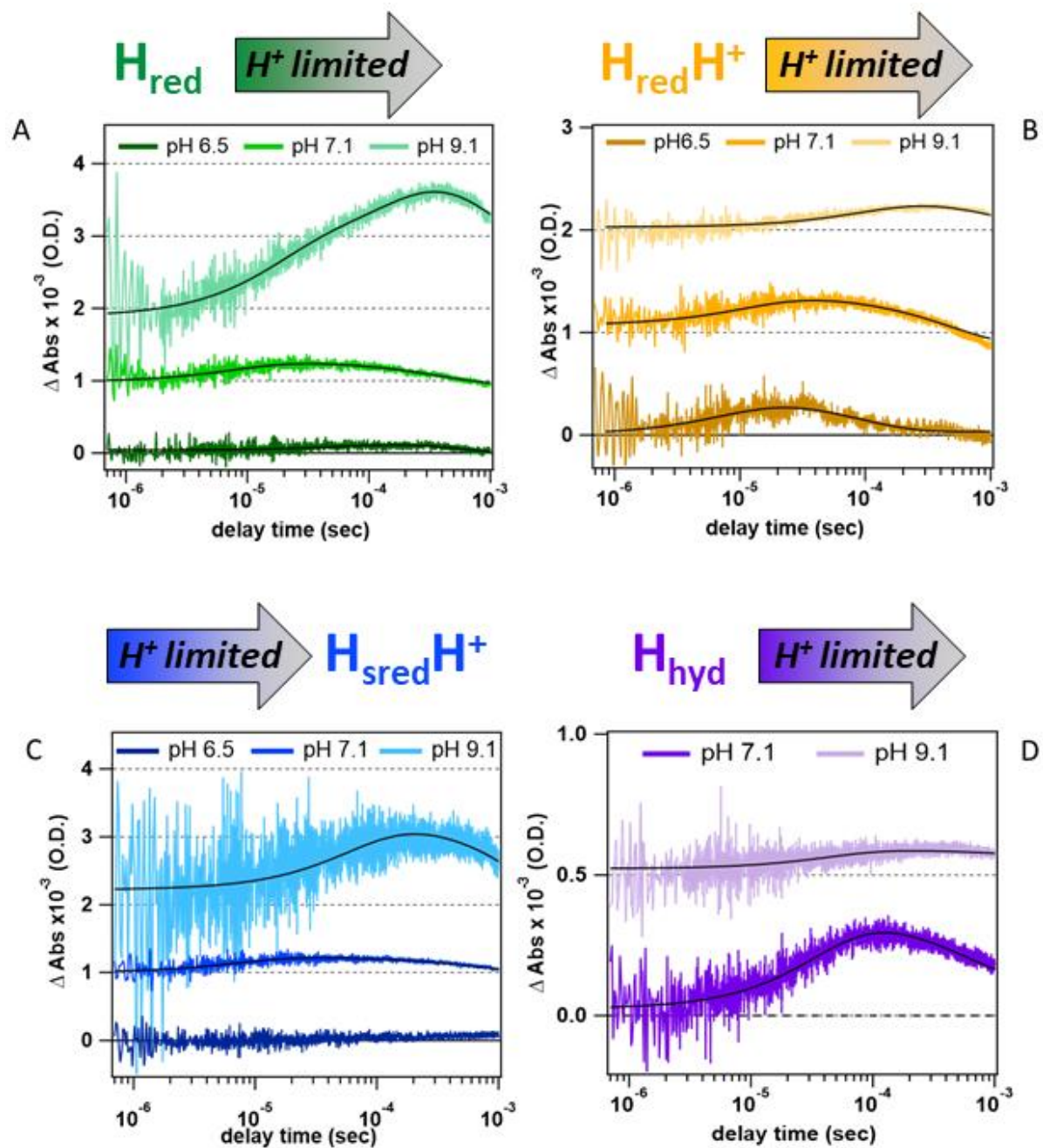


Figure 5.12 pH dependence of transitioning between intermediate states for *DdHydAB*

FeFe hydrogenases A) Monitoring the H_{red} intermediate at pH 6.5, 7.1 and 9.1 at 1934 cm^{-1}

B) Monitoring the $\text{H}_{\text{red}}\text{H}^+$ intermediate at pH 6.5, 7.1 and 9.1 at 1916 cm^{-1} C) Monitoring

the $\text{H}_{\text{sred}}\text{H}^+$ intermediate at pH 6.5, 7.1 and 9.1 at 1911 cm^{-1} D) Monitoring the H_{hyd}

intermediate at pH 7.1 and 9.1.

$H_{red}H^+$ (1911 cm^{-1}) The $H_{red}H^+$ intermediate state has been characterized as having a 1-electron reduced H-cluster and protonated pendant amine group.²²⁻²³ When kinetics for this intermediate state were obtained by monitoring at 1911 cm^{-1} , the observed rates of formation of the $H_{red}H^+$ intermediate does not show the anticipated proton dependence. The pH 6.5 and pH 7.1 samples show nearly identical formation rates of 8 μs and 12 μs respectively, well within the error of the fitting. Because the pKa of the amino group is ~ 7.2 ¹² the similarity of these rates is not unexpected since we are close to this threshold at pH 6.5 and pH 7.1. It is not until the kinetics were measured at pH 9.1, is a slower rate of formation of this population observable, (105 μs). The decay of the $H_{red}H^+$ population, interestingly, clearly shows this to be a proton limited transition with rates that mirror the increasing basicity of each sample: 90 μs , 427 μs and 2000 μs respectively. This observation is evidence that, after the formation of $H_{red}H^+$, the next intermediate state to be populated involves a subsequent proton transfer step.

$H_{sred}H^+$ (1915 cm^{-1}) The $H_{sred}H^+$ intermediate state has been characterized as having a 2-electron reduced H-cluster, 1-electron housed on one of the auxiliary Fe_4S_4 cluster and 1-electron on the distal Fe of the di-Fe active site. This intermediate also contains a protonated pendant amine and has been proposed to be the sequential intermediate following the $H_{red}H^+$ intermediate formed by ET to $H_{red}H^+$. Monitoring at the 1915 cm^{-1} frequency reveals a trend in formation lifetimes similar to what is observed with the H_{red} intermediate. At pH 6.5, no population of $H_{sred}H^+$ is observed to form, however, similar to what was observed when monitoring the H_{red} intermediate a small population is observed to form in the pH 7.1 sample and a large population forms for the pH 9.1 sample. Not surprisingly, the rates of formation of the $H_{sred}H^+$ intermediate in the pH 7.1 and pH 9.1 samples (8 μs and 65 μs respectively) are almost identical to those observed when monitoring the H_{red} intermediate. A similar observation has been made in

previous kinetics studies of [FeFe] hydrogenase in which this observation was explained by the direct reduction of the H_{red} population⁴² that is present in the sample at the beginning of the experiment, (Fig. 5.11A). The decay of the $H_{sred}H^+$ intermediate shows some proton dependent behavior, but these results are not consistent with any previously proposed catalytic model indicating a different analysis of this intermediate is needed to understand how it fits within the catalytic cycle of FeFe hydrogenase.

	pH: 6.5		pH: 7.1		pH: 9.1	
	$\tau_{formation} (\mu s)$	$\tau_{decay} (\mu s)$	$\tau_{formation} (\mu s)$	$\tau_{decay} (\mu s)$	$\tau_{formation} (\mu s)$	$\tau_{decay} (\mu s)$
H_{red}	None obs	None obs	8	400	16, 150	1400
$H_{red}H^+$	8	90	12	427	105	2000
$H_{sred}H^+$	None obs	None obs	8	780	65	3000
H_{hyd}			26	2000	44	70000

Table 5.1 Summary of kinetics results as formation and decay constants.

H_{hyd} (1980 cm^{-1}): Finally, the H_{hyd} intermediate state has been characterized as having an oxidized active site and a 1-electron reduced Fe_4S_4 cluster but having a hydride group coordinated in the open site on the distal Fe of the bimetallic core. The generally agreed upon mechanism for the formation of this intermediate is through the combination of an electron in the active site and the proton from the protonated pendant amine.⁴⁶ The observed formation constants of the H_{hyd} intermediate for the pH 7.1 and pH 9.1 samples (26 and 44 μs respectively) are quite similar and so do not indicate a proton limited formation. The decay that is observed of this population, however, differ quite significantly depending on pH. The decay of the H_{hyd} population in the pH 7.1 sample has a decay constant of around 2000 μs , while the pH 9.1 H_{hyd} population decays with a lifetime constant of around 8000 μs , considerably slower than what is

observed for the pH 7.1 sample. These results are consistent with a proton limited transition from the H_{hyd} intermediate to form another protonated intermediate, such as $H_{\text{hyd}}H^+$. Again, generally accepted in the field that the final intermediate before formation of a H_2 molecule in the active site is the formation of a protonated H_{hyd} like state or $H_{\text{hyd}}H^+$.^{2, 11, 13-15} The results of this study would be the first experimental evidence supporting the formation of the $H_{\text{hyd}}H^+$ intermediate state.

5.5.2 Redox Anti-cooperativity with the PDT mutant

As mentioned earlier in this section, an interesting structural feature that sets the *DdHydAB* variant apart from the *CrHydA1* variant is the presence of two additional Fe_4S_4 clusters (or F-clusters) in proximity to the active site (Fig. 5.13A) presumably acting as an ET pathway to the H-cluster. One result of this additional structural feature is the apparent occupation of intermediate states different from other [FeFe] hydrogenases.²⁰ One report describes a set of intermediate states which seem to form depending on the location of one electron in the F-cluster, each intermediate yielding detectable IR signatures.²¹ No other examples of this phenomenon with [FeFe] hydrogenase have been reported that we could find, thus we became interested in seeing whether these F-cluster related intermediates could be also characterized by their kinetics of formation .

To lay the foundation for these kinetics experiments using the same photo triggering method as in the previous sections, we began by monitoring IR frequencies suggested in the report with WT enzyme to confirm that we can identify unique kinetics at IR frequencies differing by a single wavenumber. The individual kinetics traces from the TRIR WT experiment are pictured in Fig. 5.13C.

The initial kinetics appear complex, but careful fitting has revealed isolable lifetimes for each of the species in the H_{ox} region, 1940 to 1942 cm^{-1} . The 1940 cm^{-1} H_{ox} population features a double exponential decay, the fast phase has a lifetime of 10 μs and a slow phase of 540 μs . The $\text{H}_{\text{ox}}\text{F}_{\text{ox}}$ (1941 cm^{-1}) population has three exponential decay components with lifetimes of 24 μs , 280 μs , and 600 μs . And finally the $\text{H}_{\text{ox}}\text{F}_{\text{red}}$ (1942 cm^{-1}) population features a single exponential rise with a lifetime of 26 μs and a slower decay phase of 260 μs . Some of these lifetimes can be attributed to the overlapping populations, not unexpected considering they are

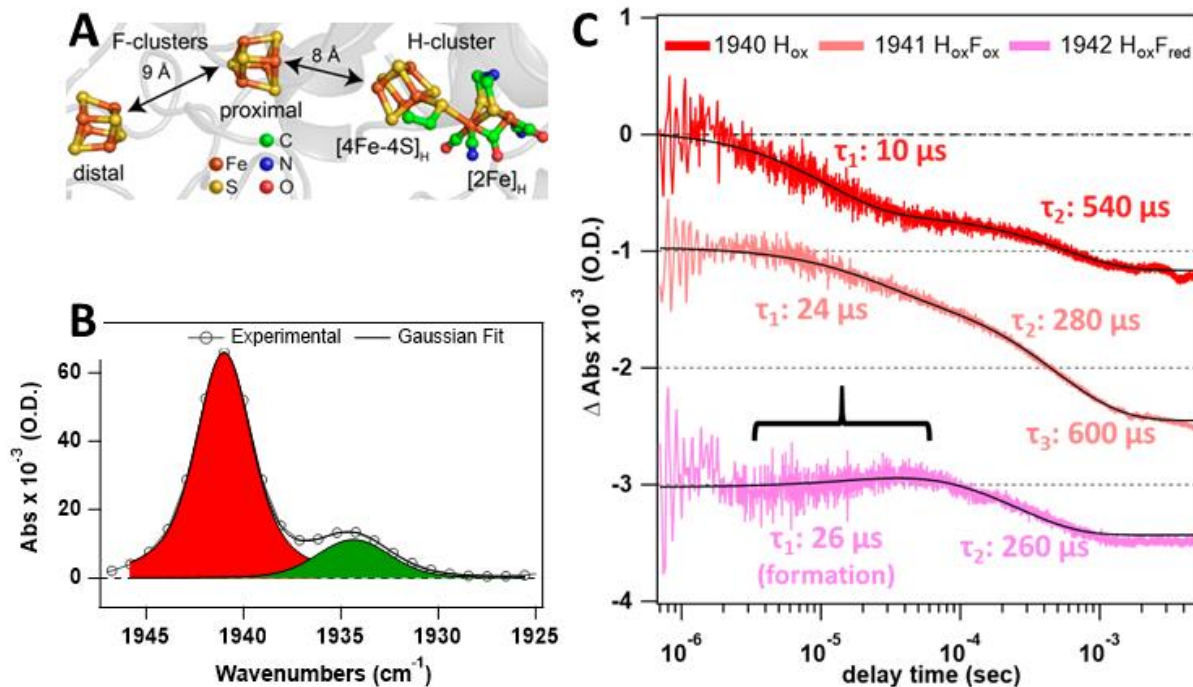


Figure 5.13 WT kinetics of F-cluster related intermediates. A) Schematic depicting relationship between auxiliary FeS clusters and H-cluster. *Figure adapted from ref 33.* B) Representative FTIR of WT sample used for kinetics measurements zoomed in on the region of interest. C) Kinetics of $H_{ox}F_{ox}$ region investigated in WT measurements.

only one wavenumber removed from each other. For instance, the slow phase in H_{ox} is quite similar to the slowest phase observed in the $H_{ox}F_{ox}$ population. Another example is clear when comparing $H_{ox}F_{ox}$ and $H_{ox}F_{red}$ in which the slowest component decay is quite similar to the 2nd fast phase decay of $H_{ox}F_{ox}$. Even more interesting, is the fact that the single exponential rise observed in $H_{ox}F_{red}$ compliments well the fast phase decay of $H_{ox}F_{ox}$.

In contrast, when the H_{red} F-cluster region (~ 1934 to 1938 cm^{-1}) was monitored, the only observable formation was of the one electron reduced intermediate, with none of the other complex F-cluster related dynamics at other frequencies. This we reasoned was likely to do with

the fact that, once formed, the H_{red} intermediate transitioned to form other intermediates along the catalytic cycle as the enzyme turned over before the F-cluster intermediates could form.

So, with the viability of this technique for monitoring such minute shifts in intermediate populations confirmed, we next sought to make the same sets of measurements, though with the PDT mutant instead. While we could not observe unique kinetics for the F-cluster related intermediate frequencies of the H_{red} intermediate state with the WT enzyme, we expected to successfully measure kinetics for these intermediate populations with the PDT mutated H-cluster. Because the PDT variant is not catalytically active and is “stuck” at the H_{red} intermediate it is an ideal candidate to study interesting inter-cluster redox effects as they occur with the H_{red} intermediate. Another key difference for this next round of kinetics experiments, was a change in excitation source. For the PDT F-cluster potential jump experiments, green light (532 nm) was used as the excitation source. The advantage of using 532 nm light is that the sample can be pumped with higher power resulting in larger potential jumps, yielding a larger signal in the IR measurements.

We began by scanning the region where we expected to measure H_{ox} F-cluster intermediates, from 1941 cm^{-1} to 1945 cm^{-1} (Fig. 5.14A). When the $H_{\text{ox}}F_{\text{ox}}$ kinetics of the PDT mutant are compared to those made with the WT protein, the results are stunningly similar. Broadly speaking, the same trend in decay and similar multi exponential kinetics are observed as we “scan” across the spectral region. The most significant difference rests in the fact that while the F-cluster kinetics for the WT H_{ox} species required 3-exponentials to accurately fit, the PDT transients required only 2 exponentials to fit. The rates observed however fit with the same general trend as with the WT enzyme albeit slightly faster. Derived from the bi exponential fits, a “fast” formation constant averaging around $15\text{ }\mu\text{s}$ and a “slow” formation constant averaging

around 100 μs were observed. This is slightly faster than the observed rate of decay of the WT $\text{H}_{\text{ox}}\text{F}_{\text{ox}}$ population and likely relates back to the fact that we are generating larger radical populations with the PDT sample, leading to faster ET.

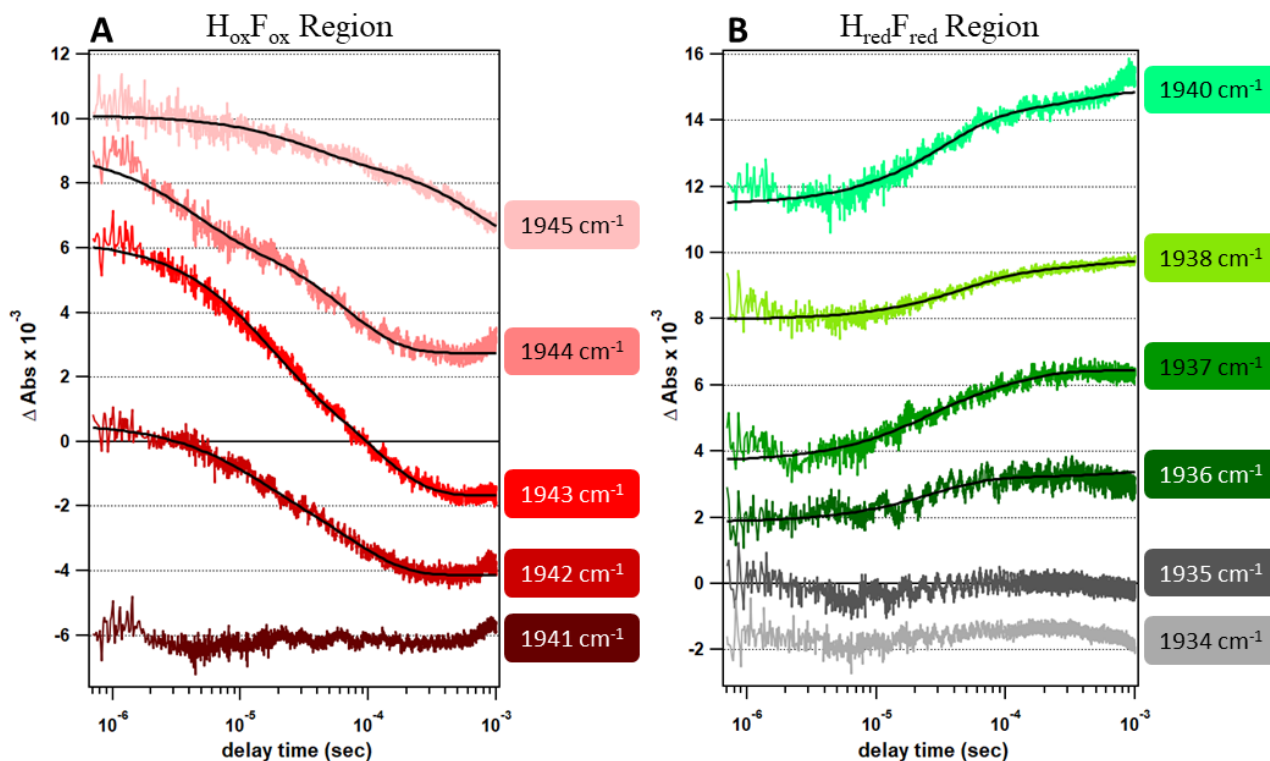


Figure 5.14 F-cluster kinetics “scanning” from 1934 cm^{-1} to 1945 cm^{-1} . A) Measuring kinetics in the $\text{H}_{\text{ox}}\text{F}_{\text{ox}}$ region from 1945 to 1941 cm^{-1} . B) Measuring kinetics in the $\text{H}_{\text{red}}\text{F}_{\text{ox}}$ region from 1934 to 1940 cm^{-1} .

Next, the region in which the H_{red} F-cluster intermediates are predicted to be observable (1934-1935 cm^{-1}) was “scanned” for evidence of multiple populations observable by our kinetics measurements. When individual transients at these frequencies are compared, we do in fact observe unique rate constants at different frequencies, which is consistent with a region which has multiple overlapping populations. Kinetics measured at 1934 and 1935 cm^{-1} yielded no observable changes in population, however beginning at 1936 cm^{-1} an increase in absorbance,

consistent with the formation of a one-electron reduced population, is observed. The rate of this formation occurs on the same timescale as the bleach of the H_{ox} population and so fits well with the current understanding of this first ET step.^{11, 22} Interestingly, each frequency measured also fits well with a bi-exponential fit function and the formation constants derived from these fits also feature a “fast” phase ranging from 20 to 45 μ s and a “slow” phase ranging from 100 μ s to 1700 μ s. These formation and decay constants are summarized in Table 5.2.

HoxFox and HredFred Kinetics of <i>DdHydAB</i>, PDT variant				
IR Frequency (cm⁻¹)	A₁	τ_1 (μs)	A₂	τ_2 (μs)
1934				
1935				
1936	-0.0013	27	-0.0004	1700
1937	-0.0015	20	-0.0012	97
1938	-0.0013	45	-0.0004	447
1940	-0.0026	32	-0.0008	360
1941				
1942	0.0017	10	0.003	74
1943	0.0037	13	0.0042	104
1944	0.0025	4	0.0037	66
1945	0.0013	31	0.0029	760

Table 5.2 Summary of formation and decay constants for PDT kinetics data with *DdHydAB*

When plots of Δ Abs vs. wavenumber are generated at specific points in time (Fig. 5.15) using the kinetics data, we can use these “time slices” to extract and visualize intermediate population distributions. From this analysis, a clearer picture of what is happening with the F-cluster intermediates develops.

Unfortunately, the data set does not include data for frequencies beyond 1945 cm^{-1} so a true appraisal of the H_{ox} region cannot be made, however some preliminary observations can be drawn regardless. When the H_{ox} region (1940 to 1945 cm^{-1}) is examined, two populations are clearly observable from the fits. The dominant population being centered at 1941 cm^{-1} and the smaller population centered at 1944 cm^{-1} . This fits with the current understanding of the interaction between the F-clusters and the H-cluster. The population at 1941 cm^{-1} is described as having a completely oxidized H-cluster and F-clusters, that is no electrons are present. A bleach of this population therefore, means there exists at least one electron somewhere on one of the Fe

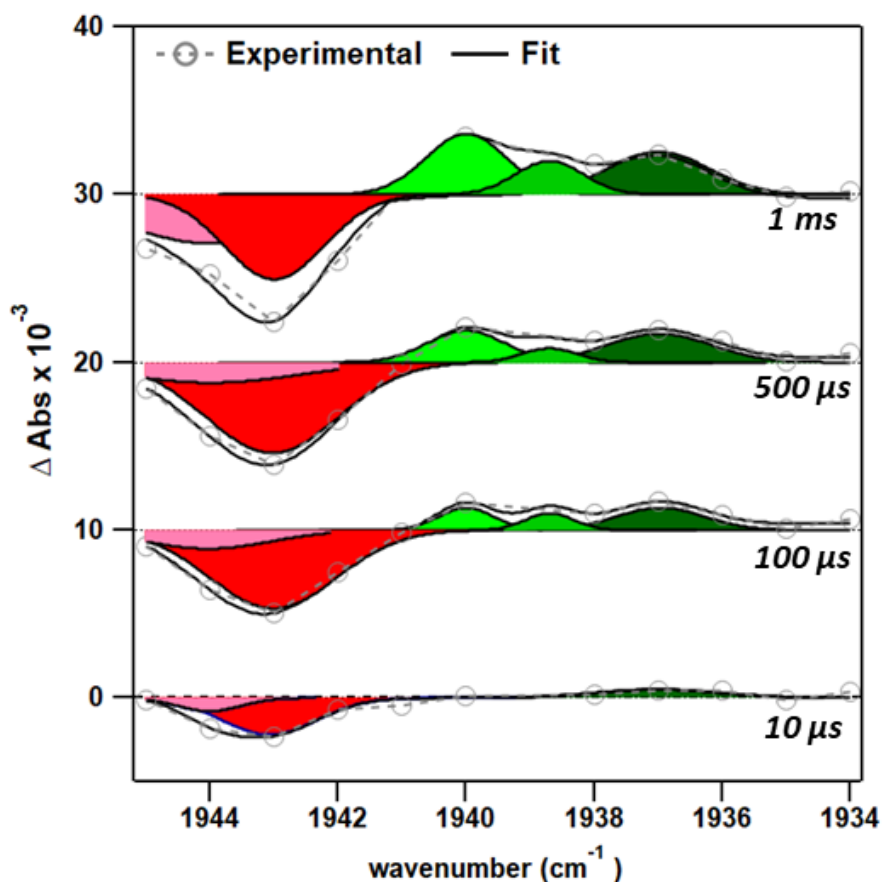


Figure 5.15 Time-resolved FTIR of region in which FeS cluster intermediates are observable.

Color scheme: Red = $\text{H}_{\text{ox}}\text{F}_{\text{ox}}$; Pink = $\text{H}_{\text{ox}}\text{F}_{\text{red}}$; Dark green = H_{red} ; light green = $\text{H}_{\text{red}}\text{F}_{\text{ox}}$; lime green = $\text{H}_{\text{red}}\text{F}_{\text{red}}$;

clusters. The small population observable at 1944 cm^{-1} corresponds with a small population of enzyme which still has an oxidized H-cluster, but now there is an electron present on one of the F-clusters. This electron is then free to move between the F-clusters

A full picture however for the H_{red} region (1934 – 1940 cm^{-1}) can be developed based on these results. Based on previous reports there are two possible intermediates which can form in this region: $\text{H}_{\text{red}}\text{F}_{\text{ox}}$ (oxidized F-clusters, one electron reduced H-cluster) and $\text{H}_{\text{red}}\text{F}_{\text{red}}$ (one electron reduced F-cluster and a one electron reduced H-cluster). However, $\text{H}_{\text{red}}\text{F}_{\text{red}}$ can technically yield two unique intermediate populations due to the location of the electron on one of the F-clusters. An electron could persist on the proximal Fe_4S_4 cluster or on the distal Fe_4S_4 cluster of the F-clusters leading to two populations observable by kinetics measurements. Thus, there are three potential intermediates which could be identified due to this F-cluster H-cluster relationship and if this is the case, three populations should be observable by our “time-slice” analysis.

When the results for the H_{red} region are examined, three populations are in fact identifiable based on the gaussian fits in the region centered at 1940, 1939 and 1937 cm^{-1} . Interestingly, there is no “dominant population” like what is observed in the H_{ox} region-the distribution between the three intermediates is roughly the same. Though, the intermediate centered at 1939 cm^{-1} does not appear to have the same amplitude as the populations at 1940 and 1937 cm^{-1} . One possible explanation is that this intermediate could be the result of the unlikely occupation of an electron on the Fe_4S_4 cluster proximal to the H-cluster. In the previously published results, there is no distinction between $\text{H}_{\text{red}}\text{F}_{\text{red}}$ intermediates which would differ by the location of the electron, i.e. whether it is located on the proximal or distal Fe_4S_4 . If this is the case, these results would be the first evidence of this occurring in this enzyme.

5.6 Conclusions on [FeFe] Hydrogenase Mechanistic Studies

By combining a technique for rapidly initiating catalysis with TRIR, a highly sensitive technique for monitoring active site chemistry, we were able to perform a series of studies designed to elucidate details about the catalytic mechanism of [FeFe] hydrogenase. After establishing the viability of this technique and identified IR frequencies which, when monitored, yield unique kinetics for individual populations, we sought to perform more detailed studies on both the *CrHydA1* enzyme and the *DdHydAB* variant.

By employing an [FeFe] hydrogenase with a mutated active site, referred to as the PDT mutant, we were able to measure active site kinetics at two different pHs and demonstrate the unambiguous lack of dependence in the rate of ET to form the H_{red} intermediate state. This result verifies that this first ET step cannot be proton coupled in which a protonated Fe_4S_4 cluster is an integral part of the ET process for the formation of H_{red} .

Using the *DdHydAB* protein, TRIR kinetics using samples prepared at different pHs were measured to determine which intermediate transitions are proton coupled. Based on the results of this study, it seems clear that the $H_{\text{red}}H^+ \rightarrow H_{\text{hyd}}$ transition is proton coupled. If this is the case, then this indicates that the $H_{\text{sred}}H^+$ intermediate state is likely an off pathway intermediate. Again, with the *DdHydAB* protein, we also monitored for the unusual H_{ox} and H_{red} F-cluster intermediates and successfully measured unique rates of formation for several of these F-cluster intermediates. More importantly, these kinetics represent the first to directly monitor ET events within Fe_4S_4 clusters of a protein.

5.6 References

1. Lubitz, W.; Ogata, H.; Rüdiger, O.; Reijerse, E., Hydrogenases. *Chemical Reviews* **2014**, *114* (8), 4081–4148.
2. Duan, J.; Senger, M.; Esselborn, J.; Engelbrecht, V.; Wittkamp, F.; Apfel, U.-P.; Hofmann, E.; Stripp, S. T.; Happe, T.; Winkler, M., Crystallographic and spectroscopic assignment of the proton transfer pathway in [FeFe]-hydrogenases. *Nature Communications* **2018**, *9* (1), 4726.
3. Ahmed, M. E.; Dey, S.; Darensbourg, M. Y.; Dey, A., Oxygen-Tolerant H₂ Production by [FeFe]-H₂ase Active Site Mimics Aided by Second Sphere Proton Shuttle. *Journal of the American Chemical Society* **2018**, *140* (39), 12457-12468.
4. Sommer, C.; Richers, C. P.; Lubitz, W.; Rauchfuss, T. B.; Reijerse, E. J., A [RuRu] Analogue of an [FeFe]-Hydrogenase Traps the Key Hydride Intermediate of the Catalytic Cycle. *Angewandte Chemie* **2018**, *130* (19), 5527-5530.
5. Liu, T.; Darensbourg, M. Y., A Mixed-Valent, Fe(II)Fe(I), Diiron Complex Reproduces the Unique Rotated State of the [FeFe]Hydrogenase Active Site. *Journal of the American Chemical Society* **2007**, *129* (22), 7008-7009.
6. Slater, J. W.; Marguet, S. C.; Monaco, H. A.; Shafaat, H. S., Going beyond Structure: Nickel-Substituted Rubredoxin as a Mechanistic Model for the [NiFe] Hydrogenases. *Journal of the American Chemical Society* **2018**, *140* (32), 10250-10262.
7. Onoda, A.; Hayashi, T., Artificial hydrogenase: biomimetic approaches controlling active molecular catalysts. *Current Opinion in Chemical Biology* **2015**, *25*, 133-140.

8. Roy, S.; Groy, T. L.; Jones, A. K., Biomimetic model for [FeFe]-hydrogenase: asymmetrically disubstituted diiron complex with a redox-active 2,2'-bipyridyl ligand. *Dalton Transactions* **2013**, 42 (11), 3843-3853.
9. Siebel, J. F.; Adamska-Venkatesh, A.; Weber, K.; Rumpel, S.; Reijerse, E.; Lubitz, W., Hybrid [FeFe]-Hydrogenases with Modified Active Sites Show Remarkable Residual Enzymatic Activity. *Biochemistry* **2015**, 54 (7), 1474-1483.
10. Huynh, M. H. V.; Meyer, T. J., Proton-coupled electron transfer. *Chemical Reviews* **2007**, 107 (11), 5004-5064.
11. Wittkamp, F.; Senger, M.; Stripp, S. T.; Apfel, U. P., [FeFe]-Hydrogenases: recent developments and future perspectives. *Chemical Communications* **2018**, 54 (47), 5934-5942.
12. Sommer, C.; Adamska-Venkatesh, A.; Pawlak, K.; Birrell, J. A.; Rudiger, O.; Reijerse, E. J.; Lubitz, W., Proton Coupled Electronic Rearrangement within the H-Cluster as an Essential Step in the Catalytic Cycle of [FeFe] Hydrogenases. *J. Am. Chem. Soc.* **2017**, 139 (4), 1440-1443.
13. Rodríguez-Maciá, P.; Kertess, L.; Burnik, J.; Birrell, J. A.; Hofmann, E.; Lubitz, W.; Happe, T.; Rüdiger, O., His-Ligation to the [4Fe-4S] Subcluster Tunes the Catalytic Bias of [FeFe] Hydrogenase. *Journal of the American Chemical Society* **2019**, 141 (1), 472-481.
14. Senger, M.; Mebs, S.; Duan, J.; Shulenina, O.; Laun, K.; Kertess, L.; Wittkamp, F.; Apfel, U.-P.; Happe, T.; Winkler, M.; Haumann, M.; Stripp, S. T., Protonation/reduction dynamics at the [4Fe-4S] cluster of the hydrogen-forming cofactor in [FeFe]-hydrogenases. *Physical Chemistry Chemical Physics* **2018**, 20 (5), 3128-3140.

15. Ratzloff, M. W.; Artz, J. H.; Mulder, D. W.; Collins, R. T.; Furtak, T. E.; King, P. W., CO-Bridged H-Cluster Intermediates in the Catalytic Mechanism of [FeFe]-Hydrogenase CaI. *Journal of the American Chemical Society* **2018**, *140* (24), 7623-7628.
16. Haumann, M.; Stripp, S. T., The Molecular Proceedings of Biological Hydrogen Turnover. *Accounts of Chemical Research* **2018**.
17. Adamska-Venkatesh, A.; Krawietz, D.; Siebel, J.; Weber, K.; Happe, T.; Reijerse, E.; Lubitz, W., New Redox States Observed in [FeFe] Hydrogenases Reveal Redox Coupling Within the H-Cluster. *Journal of the American Chemical Society* **2014**, *136* (32), 11339-11346.
18. Greene, B. L.; Schut, G. J.; Adams, M. W. W.; Dyer, R. B., Pre-Steady-State Kinetics of Catalytic Intermediates of an [FeFe]-Hydrogenase. *ACS Catalysis* **2017**, *7* (3), 2145-2150.
19. Greene, B. L.; Vansuch, G. E.; Chica, B. C.; Adams, M. W. W.; Dyer, R. B., Applications of Photogating and Time Resolved Spectroscopy to Mechanistic Studies of Hydrogenases. *Accounts of Chemical Research* **2017**, *50* (11), 2718-2726.
20. Adamska, A.; Silakov, A.; Lambertz, C.; Rudiger, O.; Happe, T.; Reijerse, E.; Lubitz, W., Identification and characterization of the "super-reduced" state of the H-cluster in [FeFe] hydrogenase: a new building block for the catalytic cycle? *Angewandte Chemie International Edition* **2012**, *51* (46), 11458-62.
21. Rodríguez-Maciá, P.; Pawlak, K.; Rüdiger, O.; Reijerse, E. J.; Lubitz, W.; Birrell, J. A., Intercluster Redox Coupling Influences Protonation at the H-cluster in [FeFe] Hydrogenases. *Journal of the American Chemical Society* **2017**, *139* (42), 15122-15134.
22. Land, H.; Senger, M.; Berggren, G.; Stripp, S. T., Current State of [FeFe]-Hydrogenase Research: Biodiversity and Spectroscopic Investigations. *ACS Catalysis* **2020**, 7069-7086.

23. Greene, B. L.; Joseph, C. A.; Maroney, M. J.; Dyer, R. B., Direct Evidence of Active-Site Reduction and Photodriven Catalysis in Sensitized Hydrogenase Assemblies. *Journal of the American Chemical Society* **2012**, *134* (27), 11108-11111.
24. Greene, B. L.; Wu, C.-H.; McTernan, P. M.; Adams, M. W. W.; Dyer, R. B., Proton-Coupled Electron Transfer Dynamics in the Catalytic Mechanism of a [NiFe]-Hydrogenase. *Journal of the American Chemical Society* **2015**, *137* (13), 4558-4566.
25. Sanchez, M. L. K.; Wu, C.-H.; Adams, M. W. W.; Dyer, R. B., Optimizing electron transfer from CdSe QDs to hydrogenase for photocatalytic H₂ production. *Chemical Communications* **2019**, *55* (39), 5579-5582.
26. Mulder, D. W.; Boyd, E. S.; Sarma, R.; Lange, R. K.; Endrizzi, J. A.; Broderick, J. B.; Peters, J. W., Stepwise [FeFe]-hydrogenase H-cluster assembly revealed in the structure of HydAΔEFG. *Nature* **2010**, *465*, 248.
27. Chica, B.; Wu, C.-H.; Liu, Y.; Adams, M. W. W.; Lian, T.; Dyer, R. B., Balancing electron transfer rate and driving force for efficient photocatalytic hydrogen production in CdSe/CdS nanorod-[NiFe] hydrogenase assemblies. *Energy & Environmental Science* **2017**, *10* (10), 2245-2255.
28. Zhao, F.; Li, Q.; Han, K.; Lian, T., Mechanism of Efficient Viologen Radical Generation by Ultrafast Electron Transfer from CdS Quantum Dots. *The Journal of Physical Chemistry C* **2018**, *122* (30), 17136-17142.
29. Sensi, M.; Baffert, C.; Fradale, L.; Gauquelin, C.; Soucaille, P.; Meynial-Salles, I.; Bottin, H.; de Gioia, L.; Bruschi, M.; Fourmond, V.; Léger, C.; Bertini, L., Photoinhibition of FeFe Hydrogenase. *ACS Catalysis* **2017**, *7* (10), 7378-7387.

30. Roseboom, W.; De Lacey, A. L.; Fernandez, V. M.; Hatchikian, E. C.; Albracht, S. P. J., The active site of the [FeFe]-hydrogenase from *Desulfovibrio desulfuricans*. II. Redox properties, light sensitivity and CO-ligand exchange as observed by infrared spectroscopy. *JBIC Journal of Biological Inorganic Chemistry* **2006**, *11* (1), 102-118.
31. Goldet, G.; Brandmayr, C.; Stripp, S. T.; Happe, T.; Cavazza, C.; Fontecilla-Camps, J. C.; Armstrong, F. A., Electrochemical Kinetic Investigations of the Reactions of [FeFe]-Hydrogenases with Carbon Monoxide and Oxygen: Comparing the Importance of Gas Tunnels and Active-Site Electronic/Redox Effects. *Journal of the American Chemical Society* **2009**, *131* (41), 14979-14989.
32. Baffert, C.; Bertini, L.; Lautier, T.; Greco, C.; Sybirna, K.; Ezanno, P.; Etienne, E.; Soucaille, P.; Bertrand, P.; Bottin, H.; Meynial-Salles, I.; De Gioia, L.; Léger, C., CO Disrupts the Reduced H-Cluster of FeFe Hydrogenase. A Combined DFT and Protein Film Voltammetry Study. *Journal of the American Chemical Society* **2011**, *133* (7), 2096-2099.
33. Lemon, B. J.; Peters, J. W., Binding of Exogenously Added Carbon Monoxide at the Active Site of the Iron-Only Hydrogenase (CpI) from *Clostridium pasteurianum*. *Biochemistry* **1999**, *38* (40), 12969-12973.
34. Talapin, D. V.; Koeppel, R.; Götzinger, S.; Kornowski, A.; Lupton, J. M.; Rogach, A. L.; Benson, O.; Feldmann, J.; Weller, H., Highly Emissive Colloidal CdSe/CdS Heterostructures of Mixed Dimensionality. *Nano Letters* **2003**, *3* (12), 1677-1681.
35. Mirmohades, M.; Adamska-Venkatesh, A.; Sommer, C.; Reijerse, E.; Lomoth, R.; Lubitz, W.; Hammarström, L., Following [FeFe] Hydrogenase Active Site Intermediates by Time-Resolved Mid-IR Spectroscopy. *The Journal of Physical Chemistry Letters* **2016**, *7* (16), 3290-3293.

36. Mulder, D. W.; Ratzloff, M. W.; Shepard, E. M.; Byer, A. S.; Noone, S. M.; Peters, J. W.; Broderick, J. B.; King, P. W., EPR and FTIR Analysis of the Mechanism of H₂ Activation by [FeFe]-Hydrogenase HydA1 from *Chlamydomonas reinhardtii*. *Journal of the American Chemical Society* **2013**, *135* (18), 6921-6929.
37. Cramer Stephen, P.; Pham Cindy, C.; Mulder David, W.; Pelmeshnikov, V.; King Paul, W.; Ratzloff Michael, W.; Wang, H.; Mishra, N.; Alp, E.; Zhao, J.; Hu Michael, Y.; Tamasaku, K.; Yoda, Y., Terminal Hydride Species in [FeFe]-Hydrogenases are Vibrationally Coupled to the Active Site Environment. *Angewandte Chemie International Edition* **2018**, *0* (ja).
38. Papini, C.; Sommer, C.; Pecqueur, L.; Pramanik, D.; Roy, S.; Reijerse, E. J.; Wittkamp, F.; Artero, V.; Lubitz, W.; Fontecave, M., Bioinspired Artificial [FeFe]-Hydrogenase with a Synthetic H-Cluster. *ACS Catalysis* **2019**, *9* (5), 4495-4501.
39. Senger, M.; Laun, K.; Wittkamp, F.; Duan, J.; Haumann, M.; Happe, T.; Winkler, M.; Apfel, U.-P.; Stripp, S. T., Proton-Coupled Reduction of the Catalytic [4Fe-4S] Cluster in [FeFe]-Hydrogenases. *Angewandte Chemie International Edition* **2017**, *56* (52), 16503-16506.
40. Mebs, S.; Duan, J.; Wittkamp, F.; Stripp, S. T.; Happe, T.; Apfel, U.-P.; Winkler, M.; Haumann, M., Differential Protonation at the Catalytic Six-Iron Cofactor of [FeFe]-Hydrogenases Revealed by ⁵⁷Fe Nuclear Resonance X-ray Scattering and Quantum Mechanics/Molecular Mechanics Analyses. *Inorganic Chemistry* **2019**, *58* (6), 4000-4013.
41. Senger, M.; Eichmann, V.; Laun, K.; Duan, J.; Wittkamp, F.; Knör, G.; Apfel, U.-P.; Happe, T.; Winkler, M.; Heberle, J.; Stripp, S. T., How [FeFe]-Hydrogenase Facilitates Bidirectional Proton Transfer. *Journal of the American Chemical Society* **2019**, *141* (43), 17394-17403.

42. Sanchez, M. L. K.; Sommer, C.; Reijerse, E.; Birrell, J. A.; Lubitz, W.; Dyer, R. B., Investigating the Kinetic Competency of CrHydA1 [FeFe] Hydrogenase Intermediate States via Time-Resolved Infrared Spectroscopy. *Journal of the American Chemical Society* **2019**, *141* (40), 16064-16070.
43. Silakov, A.; Kamp, C.; Reijerse, E.; Happe, T.; Lubitz, W., Spectroelectrochemical Characterization of the Active Site of the [FeFe] Hydrogenase HydA1 from *Chlamydomonas reinhardtii*. *Biochemistry* **2009**, *48* (33), 7780-7786.
44. Fontecilla-Camps, J. C.; Volbeda, A.; Cavazza, C.; Nicolet, Y., Structure/Function Relationships of [NiFe]- and [FeFe]-Hydrogenases. *Chemical Reviews* **2007**, *107* (10), 4273-4303.
45. Caserta, G.; Papini, C.; Adamska-Venkatesh, A.; Pecqueur, L.; Sommer, C.; Reijerse, E.; Lubitz, W.; Gauquelin, C.; Meynial-Salles, I.; Pramanik, D.; Artero, V.; Atta, M.; del Barrio, M.; Faivre, B.; Fourmond, V.; Léger, C.; Fontecave, M., Engineering an [FeFe]-Hydrogenase: Do Accessory Clusters Influence O₂ Resistance and Catalytic Bias? *Journal of the American Chemical Society* **2018**, *140* (16), 5516-5526.
46. Wiedner, E. S., Thermodynamic Hydricity of [FeFe]-Hydrogenases. *Journal of the American Chemical Society* **2019**, *141* (18), 7212-7222.

Chapter 6

Conclusions and Future Directions

6.1 Conclusions

The research and studies described in this thesis can be described as two aims. The first aim was to improve upon the previously established potential jump technique through the exploration of new mediators, new photosensitizers and optimizing potential jump sample conditions. The second was to leverage the knowledge gained from the studies characterizing and optimizing the potential jump technique for the purpose of studying hydrogenase enzymes.

Chapter 3 described, in depth, the discoveries made from expanding the repertoire of small molecule mediators used for the potential jump studies. From this study, the relationship between the driving force for ET between photosensitizer, mediator and catalyst was cemented. It was also demonstrated that to achieve optimal efficiency, consideration between driving force, forward ET and back ET must be considered.

Chapter 4 outlined a study in which the sample conditions, such as: pH, mediator salt concentration, photosensitizer concentration, catalyst concentration and photon flux can all be utilized to influence ET rates for photocatalytic studies. Establishing these parameters, was imperative to broadening the applicability of the potential jump approach for the study of biocatalytic systems other than hydrogenase. Taken cumulatively the results of chapters 3 and 4, drive home the complex interplay between the components of this system and the fine tuning which can be achieved through simple modifications.

In Chapter 5 of this thesis, the potential jump technique described in the previous chapters was applied for the mechanistic study of [FeFe] hydrogenase enzymes. Two different hydrogenases were examined, one from the organism *Chlamydomonas reinhardtii*, CrHydA1 and one from the organism *Desulfovibrio desulfuricans*, DdHydAB.

In the first section of chapter 5, the goal was to validate this photoinitiation technique as suitable for studying [FeFe] hydrogenase as well as to establish the kinetic competency of several intermediate states the enzyme was proposed to occupy during turnover. The second section of this chapter described preliminary studies examining the differences between the two hydrogenase variants, *CrHydA1* and *DdHydAB*, and how the differences in protein architecture might influence the occupation of different intermediate states in the [FeFe] hydrogenase catalytic cycle.

6.2 Future Directions and Potential Avenues of Investigation

The results presented in this thesis lay the foundation for several potential avenues for further investigation. One path would be to focus exclusively on the interplay between the photosensitizer, mediator and protein. A comprehensive model for the ET mechanism between photosensitizer and this class of mediators has also hardly been explored. It is not difficult to imagine several modifications and variations to the mediator structures which could be used to interrogate the ET mechanism at the mediator, photosensitizer, and protein junctions. Such an investigation would expand the utility of the potential jump system by providing a more complete fundamental basis for designing such photocatalytic systems. Additionally, the breadth of reduction potentials and modifiability of the mediators examined also opens the door to a number of studies of other oxidoreductase enzymes which might require more reducing conditions, such as CODH.

For the [FeFe] hydrogenase enzymes examined in this work, there are several studies which could yield interesting results and further our understanding of this dynamic enzyme. The

proton dependence for the formation of different intermediate states has not been examined in depth. Identification of which intermediates form by PCET can be determined by measuring the rate of formation under different pH conditions. This can be done for both the *DdHydAB* enzyme as well as the *CrHydA1* variant. This set of experiments is critical for building a comprehensive model of the catalytic mechanism for FeFe hydrogenase. Kinetic isotope effect studies can also provide compelling evidence for which intermediate transitions are proton coupled events and which are ET only.

Also, inherent to [FeFe] hydrogenase enzymes, is the facile modifiability of the active site. Because the H-cluster is synthesized independent of protein expression, it is easily modified synthetically. This modifiability opens the door to several non-native substitutions into the active site, such as introducing non-native metals or other atoms into the inner coordination sphere. These substitutions allow several aspects of the intermediate populations to be probed directly, such as trapping different intermediate states for instance for further characterization. All of these are rich avenues to be explored and can give great insight into the catalytic mechanism of this fascinating class of enzymes.